

**Dynamics and nature of photogenerated excitons and charges in transition metal dichalcogenide thin films**

Poonia, D.

**DOI**

[10.4233/uuid:05eef4ec-d5a2-4bc7-8dbe-57651f5ece60](https://doi.org/10.4233/uuid:05eef4ec-d5a2-4bc7-8dbe-57651f5ece60)

**Publication date**

2023

**Document Version**

Final published version

**Citation (APA)**

Poonia, D. (2023). *Dynamics and nature of photogenerated excitons and charges in transition metal dichalcogenide thin films*. [Dissertation (TU Delft), Delft University of Technology].  
<https://doi.org/10.4233/uuid:05eef4ec-d5a2-4bc7-8dbe-57651f5ece60>

**Important note**

To cite this publication, please use the final published version (if applicable).  
Please check the document version above.

**Copyright**

Other than for strictly personal use, it is not permitted to download, forward or distribute the text or part of it, without the consent of the author(s) and/or copyright holder(s), unless the work is under an open content license such as Creative Commons.

**Takedown policy**

Please contact us and provide details if you believe this document breaches copyrights.  
We will remove access to the work immediately and investigate your claim.

# **Dynamics and nature of photogenerated excitons and charges in transition metal dichalcogenide thin films**

**Deepika Poonia**

## Propositions

1. Despite the high binding energy of excitons, free charges are also present after photoexcitation of ReS<sub>2</sub> nanoflakes. (Chapter 2)
2. Metal atoms are homogeneously distributed in the Mo<sub>0.6</sub>W<sub>0.4</sub>S<sub>2</sub> alloy. (Chapter 3)
3. Free charges alter the absorption profile of excitons on ultrashort time scales. (Chapter 4)
4. Multiexciton generation is efficient in monolayer MoSe<sub>2</sub>. (Chapter 5)
5. Pump-probe delay time and photoexcitation density crucially affect the nature of photogenerated species in transition metal dichalcogenides.
6. The success of a PhD student is dependent on how well the experimental data and methods, and reports on failed experiments are stored and transferred.
7. Research articles should have an uncensored 'after-thoughts' section.
8. Regular visits/traineeships in relevant industry will help in keeping researchers motivated.
9. Office computers must give a warning every 30 minutes that prolonged sitting is injurious to health.
10. Sadly, the possibility of life on Mars is given more attention than preserving the existing biodiversity on Earth.

These propositions are regarded as opposable and defensible, and have been approved as such by the promoters prof. dr. L.D.A. Siebbeles and prof. dr. P. Schall.

**Dynamics and nature of photogenerated excitons and charges in transition metal dichalcogenide thin films**



**Dynamics and nature of photogenerated excitons and charges in transition metal  
dichalcogenide thin films**

**Proefschrift**

ter verkrijging van de graad van doctor  
aan de Technische Universiteit Delft,  
op gezag van de Rector Magnificus prof. dr. ir. T. H. J. J. van der Hagen,  
voorzitter van het College voor Promoties,  
in het openbaar te verdedigen op  
woensdag 11 oktober 2023 om 12:30 uur

door

**Deepika POONIA**

Master of Science in Physics

Indian Institute of Technology Indore, India

geboren te Jaipur, India

Dit proefschrift is goedgekeurd door de promotoren.

Samenstelling promotiecommissie:

Rector Magnificus	Voorzitter
Prof. dr. L. D. A. Siebbeles	Technische Universiteit Delft, promotor
Prof. dr. P. Schall	University of Amsterdam, promotor
Onafhankelijke leden:	
Prof. dr. J. Gomez Rivas	Technische Universiteit Eindhoven
Dr. C. de Mello-Donega	Universiteit Utrecht
Prof. dr. A. J. Houtepen	Technische Universiteit Delft
Prof. dr. F.C. Grozema	Technische Universiteit Delft
Prof. dr. P. Dorenbos	Technische Universiteit Delft



Het in dit proefschrift gerapporteerde werk is gefinancierd door de Nederlandse Organisatie voor Wetenschappelijk Onderzoek (NWO) in het kader van Materialen voor Duurzaamheid en het Ministerie van Economische Zaken in het kader van de PPS-toeslag. Een deel van het NWO-project is gefinancierd via Toyota Motor Europe. De TD-DFT berekeningen zijn uitgevoerd op de Nationale e-Infrastructuur met ondersteuning van de SURF-Coöperatie.

## Table of Contents

<b>Chapter 1</b>	<b>Introduction</b>	7
	1.1 Two-dimensional van der Waals materials	8
	1.2 Optical properties of TMDCs	9
	1.3 Tuning the optical properties of TMDCs by alloying	11
	1.4 Carrier multiplication	11
	1.5 Experimental techniques to probe photoexcitations	12
	1.6 Overview of the thesis	15
<b>Chapter 2</b>	<b>Unraveling the photophysics of liquid-phase exfoliated two-dimensional ReS<sub>2</sub> nanoflakes</b>	21
	2.1 Introduction	22
	2.2 Materials and methods	23
	2.3 Results and discussion	23
	2.4 Conclusions	34
<b>Appendix A2</b>		34
<b>Chapter 3</b>	<b>Effects of the structure and temperature on the nature of excitons in the Mo<sub>0.6</sub>W<sub>0.4</sub>S<sub>2</sub> alloy</b>	55
	3.1 Introduction	56
	3.2 Materials and methods	57
	3.3 Results and discussion	59
	3.4 Conclusions	68
<b>Appendix A3</b>		68

<b>Chapter 4</b>	<b>Photogeneration, relaxation and many-body effects of excitons and charge carriers in MoS<sub>2</sub>, WS<sub>2</sub>, and the Mo<sub>0.6</sub>W<sub>0.4</sub>S<sub>2</sub> alloy, probed by transient optical absorption spectroscopy.</b>	79
	4.1 Introduction	80
	4.2 Materials and methods	80
	4.3 Results and discussion	81
	4.4 Conclusions	88
<b>Appendix A4</b>		89
<b>Chapter 5</b>	<b>Multiexciton generation in monolayer MoSe<sub>2</sub></b>	99
	5.1 Introduction	100
	5.2 Results and discussion	101
	5.3 Conclusions	105
<b>Summary</b>		109
<b>Samenvatting</b>		111
<b>List of publications</b>		113

# Chapter 1

## Introduction

This thesis reports the effects of the absorption of light in two-dimensional transition metal dichalcogenides. We studied the nature and relaxation dynamics of photogenerated free electrons and holes, as well as Coulombically bound electron hole pairs, which are known as neutral excitons. In the present chapter, the atomic and electronic structure and the optical properties of transition metal dichalcogenides are introduced.

## 1.1 Two-dimensional van der Waals materials

In the scientific community, graphene has been an alluring two-dimensional (2D) van der Waals material owing to its unique band structure and exceptional carrier mobility values.<sup>1,2</sup> But, graphene does not stand alone in the fascinating land of 2D materials and since then, many 2D materials such as transition metal-dichalcogenides (TMDCs), black phosphorous or phosphorene and hexagonal boron-nitride (h-BN) have received widespread attention from researchers. The research in TMDCs alone has grown exponentially after 2010 and has been expanded to the realm of multilayer heterostructures to form type II semiconductor heterojunctions that facilitate efficient charge separation.<sup>3,4</sup>

Transition metal dichalcogenides are represented by the chemical formula  $\text{MX}_2$ , where M is a transition metal element of groups IV-VII B (Mo, W, V, Nb, Ta, Ti, Zr, Hf, Tc, and Re) and X is a chalcogen element (S, Se, and Te). TMDCs form a layered structure of the form X-M-X, with chalcogen atoms situated in two hexagonal planes which are separated by a plane of metal atoms. The metal atoms are covalently bonded to two nearby chalcogen atoms with octahedral or trigonal prismatic coordination numbers as shown in Figure 1.1a. Van der Waals interactions hold individual  $\text{MX}_2$  layers together to form a bulk crystal of different polytypes, which vary by stacking order and atom coordination.<sup>5</sup> The bulk crystal can be easily thinned down to monolayers of  $\sim 0.7$  nm thickness using mechanical exfoliation, which allows flexible integration of different materials and opens a new area of material engineering on a nanoscale.

The electronic band structure of TMDCs ranges from metals to semiconductors.<sup>6</sup> In this thesis, we studied semiconducting TMDCs with an intrinsic bandgap in the visible or near-infrared part of the electromagnetic spectrum. As shown in Figure 1.1b, the band alignment in TMDCs lies in between conducting graphene and insulating h-BN and varies from 1L to multilayer  $\text{MX}_2$ . TMDCs exhibit unique optical and electronic properties which are heavily dependent on the film thickness and are interesting to study, both from application and fundamental science points of view.

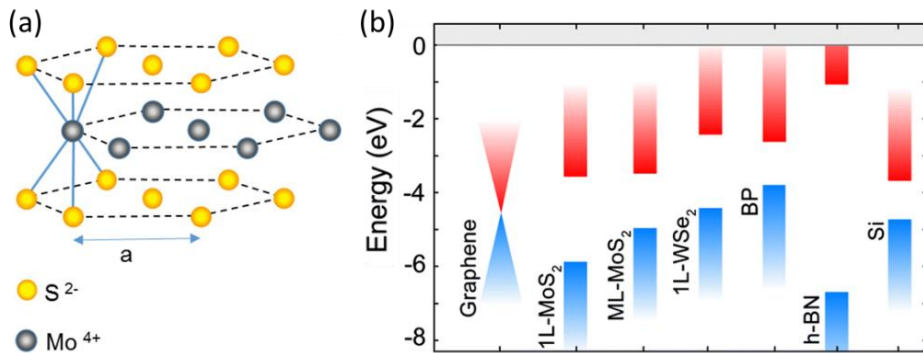


**Figure 1.1.** (a) Mo and S layers are forming a hexagonal structure.<sup>5</sup> (b) Schematic band alignment in 1L and multilayer (ML) TMDCs compared with other 2D materials.<sup>7</sup>

## 1.2 Optical properties of TMDCs

In the nanoscale limit, the optical response of TMDCs is governed by excitons. Excitons are the bound states of electrons and holes which are held together by Coulomb interactions. In the  $k$ -space, an exciton is visualized as two parabolic bands as shown in Figure 1.2a. The strength of the Coulomb interactions determines the binding energy of excitons. In monolayer TMDCs, the binding energy of excitons is of the order of hundreds of meV while in the bulk binding energy of excitons is of the order of tens of meV.<sup>8</sup> The large difference in binding energy stems from the change in the dielectric environment on going from bulk to monolayer which consequently affects the carrier-carrier interaction. These changes are shown schematically in Figure 1.2b for both bulk (3D) and monolayer (2D) samples. In bulk, most of the electric field lines traverse inside the sample, while in monolayer, the field lines traverse outside the sample too and hence, experience a different dielectric environment. This leads to an overall reduction of dielectric screening ( $\epsilon_{2D}$ ) and more pronounced Coulomb interactions in 2D.

The striking feature in layered TMDCs is the transition from indirect to direct bandgap when the material is thinned to monolayers. The transition from bulk to monolayer also alters other physical properties such as bandgap,<sup>11</sup> photoluminescence efficiency<sup>12</sup>, and photoconductivity.<sup>13</sup>

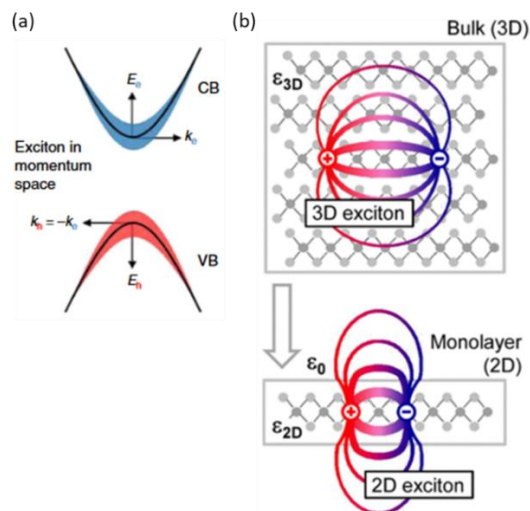


**Figure 1.2.** (a) Schematic representation of an exciton in  $k$ -space.<sup>9</sup> (b) Exciton in real space for bulk and monolayer TMDCs. Coulomb effects are much stronger in 2D than 3D due to reduced dielectric screening in a monolayer. Reproduced with permission from ref. 10.

The first optical experiments were performed on MoS<sub>2</sub> and two dominant emission peaks started appearing in the visible range on reducing film thickness (Figure 1.3a).<sup>12</sup> The peaks are labeled as A and B excitons and correspond to the direct bandgap transition at the K and K' points of the Brillouin zone (Figure 1.3b).<sup>12–14</sup> The spin-orbit coupling in the valence band determines the energy difference between A and B excitons in monolayers.

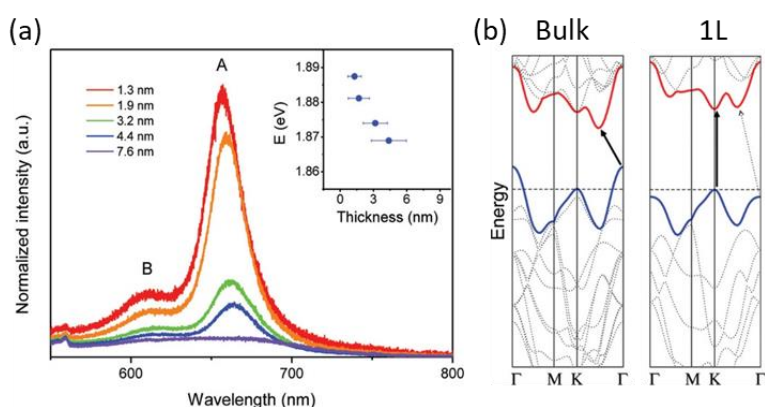


**Figure 1.3.** (a) The emergence of A and B exciton emission peaks on reducing the film thickness in MoS<sub>2</sub>. Reproduced with permission from ref. 15 (b) Indirect to direct bandgap transition on reducing the film thickness. Reproduced with permission from ref. 12

### 1.3 Tuning the optical properties of TMDCs by alloying

The band structure and optoelectronic properties of TMDCs can be further modified by the process of alloying. Various techniques such as chemical vapor deposition, molecular beam epitaxy, and atomic layer deposition (ALD) have been used in literature to synthesize TMDC alloys. Alloying has emerged as a powerful technique to finely tune the physical properties of TMDCs. Layers of  $M_yM'_{1-y}X_2$  and  $MX_{2y}X'_{2(1-y)}$  have been synthesized by varying the composition ( $y$ ) of the metal ( $M/M'$ ) or chalcogens ( $X/X'$ ) atoms.<sup>16–18</sup> By controlling the composition, the fundamental physical properties such as effective mass and bandgap are modified effectively between the stoichiometric end point.<sup>16,19</sup>

### 1.4 Carrier multiplication

Carrier multiplication (CM) is a process in which a single high-energy photon results in the generation of more than one electron-hole pair provided that the energy of the incident photon is at least twice the bandgap. CM is highly desired in photovoltaics as Beard *et.al.* predicted that CM could overcome the Shockley-Queisser limit and can raise the solar cell efficiency to ~46%.<sup>20–22</sup> The process of CM is the inverse of Auger recombination and enables the use of high-energy photons to increase the photocurrent. In bulk semiconductors, the process is known as impact ionization. To characterize the CM process, the quantum yield of photogenerated charges and threshold photon energy need to be considered. The quantum yield is defined as the number of electron-hole pairs produced per absorbed photon. The threshold photon energy corresponds to the incident energy at which the process of CM starts.

In the literature, the CM process has been extensively studied on Pb-chalcogenides,<sup>23–25</sup> Cd-chalcogenides,<sup>26,27</sup> perovskites,<sup>28,29</sup> and silicon nanostructures.<sup>30–32</sup> Recently, TMDCs have emerged as a promising material for CM due to their optimal optical bandgaps (0.7 eV - 1eV),<sup>33</sup> and efficient sunlight absorption.<sup>4</sup> Two separate pump-probe studies have shown CM efficiencies within 94%-99% on a multilayer  $MoTe_2$ .<sup>34,35</sup> Compared to other materials, TMDCs are found to be highly CM efficient which is explained by weak electron-phonon coupling,<sup>36–38</sup> and high density of states.<sup>39</sup>

## 1.5 Experimental techniques to probe photoexcitations

Before implementing TMDCs for any application, it is important to study the response of the material upon photoexcitation. It is crucial to know in which energy regimes the material is absorbing and which types of photoexcited states are generated. Are photogenerated charges free or are they bound pairs of electrons-holes (excitons)? What is the yield of charges and how do the charges relax on time scales of femtoseconds to microseconds? To answer the above-mentioned questions, time-resolved spectroscopy is used which utilizes ultrashort laser pulses to produce and probe the dynamics of charge carriers and excitons. In the present thesis, ultrashort laser pulses are used in two techniques: Optical-pump optical-probe spectroscopy (transient absorption/reflection/transmission) and Optical-Pump Terahertz-Probe spectroscopy (OPTP).

### 1.5.1 Optical-pump optical-probe spectroscopy

Ultrafast pump optical-probe spectroscopy is an experimental technique that utilizes ultrashort light pulses of sub-picosecond time to study the generation and relaxation dynamics of photogenerated charges or excitons in solids, molecules, and nanostructures.<sup>43</sup> In this technique, a primary ultrashort laser pulse is split into two pulses: the ‘pump’ pulse of light is used to photoexcite the sample and the ‘probe’ pulse is used to measure the pump-induced changes in the sample. The detected (probe) signal is further plotted as transient absorption, transient reflection, or transient transmission which provides information about changes in the optical constants with probe delay times. In pump-probe measurements, a detector is placed behind the sample which detects the transmitted probe light through the sample. After photoexcitation, the change in the extinction ( $\Delta E$ ) is given by

$$\Delta E = E_{\text{on}} - E_{\text{off}} = -\log_{10} \left( \frac{I_{\text{on}}}{I_0} \right) + \log_{10} \left( \frac{I_{\text{off}}}{I_0} \right) = \log_{10} \left( \frac{I_{\text{off}}}{I_{\text{on}}} \right) \quad 1.1$$

$I_0$  is the intensity of the probe light in front of the sample.  $I_{\text{on}}$  and  $I_{\text{off}}$  are the transmitted probe light through the sample with and without photoexcitation by the pump pulse. Hence, an indirect approach of measurements to detect ultrafast electronic dynamics is used without knowing  $I_0$  in front of the sample. In literature,  $\Delta E$  is often considered to be equal to the change in absorption ( $\Delta A$ ) assuming that the changes in reflection ( $\Delta R$ ) and scattering ( $\Delta S$ ) are negligible, as

$$T = 1 - A - R - S = 1 - E, \quad \text{and} \quad E = A + R + S \quad 1.2$$

The tabletop pump-probe setup consists of a Yb: KGW oscillator (Light Conversion, Pharos SP) for generating 180 fs pulses, centered at 1028 nm wavelength with 5 kHz frequency. The pump pulse is created by sending the fundamental beam to an Optical Parametric Amplifier (OPA). The OPA is equipped with a second harmonic module where non-linear frequency mixing is performed to produce an output pump pulse between 310 nm - 1330 nm. A small fraction of the fundamental beam is directed separately to a sapphire/CaF<sub>2</sub> crystal to generate a broadband probe spectrum from the ultraviolet to the infrared region (375 nm - 1600 nm). A mechanical chopper operating at 2.5 kHz, is placed in the path of the pump beam to allow transmission of one every two pump pulses. The pump and probe beam overlap at the sample with a relative time delay controlled by an automated delay stage. The pump pulse is dumped (after transmission through the sample), while the probe beam is collected at the detector. The pump photon fluence is estimated by using a thermopile sensor and a 1 mm radius pinhole.

### 1.5.2 Optical-pump terahertz-probe spectroscopy

Optical-pump Terahertz-probe (THz) spectroscopy is a non-contact way of determining the photoconductivity of free charges and excitons. One THz corresponds to a frequency of  $10^{12}$  Hz (1 THz  $\sim$  4 meV) and in the electromagnetic spectrum, THz frequencies lie in between the microwave and the infrared regions. In this thesis, we performed THz spectroscopy and measured transient changes of the electric field waveforms with an envelope of time duration of a few picoseconds induced after excitation of the sample by an optical pump pulse.

The THz conductivity setup is based on a laser system with a Mira Oscillator and a Legend HE-USP regenerative amplifier (by Coherent Inc). The measurements were performed by photoexciting thin films with pump pulses of 60 fs duration and probing photogenerated charge carriers and/or excitons using single-cycle THz pulses which are generated in a nonlinear zinc telluride (ZnTe) crystal via optical rectification. The latter yields a THz waveform with a duration slightly longer than 1 ps, which determines the time resolution of the OPTP measurements.<sup>44</sup> The detection of the THz waveform takes place in a ZnTe crystal by spatially overlapping the THz pulse with a chirped optical laser pulse centered

at 800 nm, such that the entire THz waveform is detected by a single laser shot.<sup>45,46</sup> This method allows us to record the transmitted THz waveform before and after photoexcitation, i.e.,  $E_0(t_p)$  and  $E_{\text{excited}}(t_p, t)$  in a time window of about 3.5 ps, which is determined by the duration of the chirped optical pulse detecting the THz waveform. The time,  $t_p$  is the detection time of the THz probe waveform, and  $t$  is the time delay between the THz probe and the laser pump pulse that photoexcites the sample. The pump pulses are generated in the visible and infrared region using optical parametric amplifier. The recorded THz waveform is Fourier transformed with respect to  $t_p$  to yield information of the complex frequency dependent change of the THz field as a function of the pump-probe time  $t$ ; i.e.  $\Delta E(\nu, t) = E_0(\nu) - E_{\text{excited}}(\nu, t)$ . The quantum yield weighted real and imaginary mobility of free charges and excitons are related to the differential THz signal  $\Delta E(\nu, t)$ ,

$$S(\nu, t) = \frac{(1+n_s)c\varepsilon_0}{eN_a} \frac{\Delta E(\nu, t)}{E_0(\nu, t)} \quad 1.3$$

while  $n_s$ ,  $c$ ,  $\varepsilon_0$  and  $e$  is the refractive index of the substrate, speed of light in a vacuum, vacuum permittivity, and elementary charge, respectively.  $N_a$  is the absorbed pump laser photon density per unit area. The samples studied are deposited on a quartz substrate ( $n_s = 2$ ).

The real part of the quantum yield weighted mobility is due to the in-phase drift velocity of charge carriers in the probing THz field. The free charges lead to the reduction of the amplitude of the transmitted THz field.<sup>47</sup> The imaginary part of quantum yield weighted mobility is due to the out-of-phase drift velocity of charges and the polarizability of excitons.<sup>47,48</sup> In bulk semiconductors and nanomaterials, the transport of charge carriers can be understood by modeling the complex mobility in the frequency domain. The Drude model has been widely used to describe the mobilities of free charges and takes into account the carrier-phonon scattering.<sup>47</sup> For nanomaterials, the Drude-Smith model is often adopted, which is an extension of the Drude model.<sup>49,50</sup> In the Drude-Smith model, physical boundaries on the nanoscale system are considered and a constant,  $c$ , referred to as a back-scattering parameter is introduced. We used the Drude-Smith model to analyze the mobility of charges in ReS<sub>2</sub> and the details are discussed in chapter 2.

## 1.6 Overview of the thesis

In the present thesis, we performed ultrafast pump-probe spectroscopy, THz photoconductivity measurements, and low-temperature optical transmission measurements. The samples under consideration were thin films of rhenium disulfide ( $\text{ReS}_2$ ), molybdenum disulfide ( $\text{MoS}_2$ ), tungsten disulfide ( $\text{WS}_2$ ), a molybdenum and tungsten disulfide alloy ( $\text{Mo}_{0.6}\text{W}_{0.4}\text{S}_2$ ) and a monolayer of molybdenum diselenide ( $\text{MoSe}_2$ ) to achieve the following set of goals:

Chapter 2. We combined ultrafast pump-probe spectroscopy with THz photoconductivity measurements to discern free charges and excitons in  $\text{ReS}_2$ . Pump-probe measurements were used to study the generation and recombination dynamics of charge carriers, while THz photoconductivity measurements were used to quantify the yield of free charges and excitons, together with the magnitude of the mobility of free charges.

Chapter 3. Low-temperature optical transmission studies were performed on  $\text{MoS}_2$ ,  $\text{WS}_2$ , and the  $\text{Mo}_{0.6}\text{W}_{0.4}\text{S}_2$  alloy to distinguish the optical properties of the alloy from the pure compounds. Low-temperature measurements along with TD-DFT calculations showed that the  $\text{Mo}_{0.6}\text{W}_{0.4}\text{S}_2$  alloy is a uniform mixture of pure  $\text{MoS}_2$  and  $\text{WS}_2$ .

Chapter 4. The photogeneration and relaxation dynamics of charge carriers are studied in multilayer samples of  $\text{MoS}_2$ ,  $\text{WS}_2$  and the  $\text{Mo}_{0.6}\text{W}_{0.4}\text{S}_2$  alloy. Free charges are found to be present in the alloy as well as in the pure compounds on a time scale from picoseconds to nanoseconds.

Chapter 5. The process of multiexciton generation is studied in a monolayer of  $\text{MoSe}_2$ . The sample is photoexcited at various pump photon energies and the quantum yield of the excitons increased for pump energies more than twice the bandgap.

## References

- (1) Novoselov, K. S.; Geim, A. K.; Morozov, S. V.; Jiang, D.; Zhang, Y.; Dubonos, S. V.; Grigorieva, I. V.; Firsov, A. A. Electric Field Effect in Atomically Thin Carbon Films. *Science* **2004**, *306*, 666–669.
- (2) Geim, A. K.; Novoselov, K. S. The Rise of Graphene. *Nat. Mater.* **2007**, *6*, 183–191.
- (3) Hong, X.; Kim, J.; Shi, S.-F.; Zhang, Y.; Jin, C.; Sun, Y.; Tongay, S.; Wu, J.; Zhang, Y.; Wang, F. Ultrafast Charge Transfer in Atomically Thin MoS<sub>2</sub>/WS<sub>2</sub> Heterostructures. *Nat. Nanotechnol.* **2014**, *9*, 682–686.
- (4) Bernardi, M.; Palumbo, M.; Grossman, J. C. Extraordinary Sunlight Absorption and One Nanometer Thick Photovoltaics Using Two-Dimensional Monolayer Materials. *Nano Lett.* **2013**, *13*, 3664–3670.
- (5) Ye, M.; Winslow, D.; Zhang, D.; Pandey, R.; Yap, Y. K. Recent Advancement on the Optical Properties of Two-Dimensional Molybdenum Disulfide (MoS<sub>2</sub>) Thin Films. *Photonics* **2015**, *2*, 288–307.
- (6) Ding, Y.; Wang, Y.; Ni, J.; Shi, L.; Shi, S.; Tang, W. First Principles Study of Structural, Vibrational and Electronic Properties of Graphene-like MX<sub>2</sub> (M=Mo, Nb, W, Ta; X=S, Se, Te) Monolayers. *Phys. B Condens. Matter* **2011**, *406*, 2254–2260.
- (7) Frisenda, R.; Molina-Mendoza, A. J.; Mueller, T.; Castellanos-Gomez, A.; Zant, H. S. J. van der. Atomically Thin p–n Junctions Based on Two-Dimensional Materials. *Chem. Soc. Rev.* **2018**, *47*, 3339–3358.
- (8) Cheiwchanchamnangij, T.; Lambrecht, W. R. L. Quasiparticle Band Structure Calculation of Monolayer, Bilayer, and Bulk MoS<sub>2</sub>. *Phys. Rev. B* **2012**, *85*, 205302.
- (9) Peng, Z.; Chen, X.; Fan, Y.; Srolovitz, D. J.; Lei, D. Strain Engineering of 2D Semiconductors and Graphene: From Strain Fields to Band-Structure Tuning and Photonic Applications. *Light Sci. Appl.* **2020**, *9*, 190.
- (10) Chernikov, A.; Berkelbach, T. C.; Hill, H. M.; Rigosi, A.; Li, Y.; Aslan, O. B.; Reichman, D. R.; Hybertsen, M. S.; Heinz, T. F. Exciton Binding Energy and Nonhydrogenic Rydberg Series in Monolayer WS<sub>2</sub>. *Phys. Rev. Lett.* **2014**, *113*, 076802.

- (11) Kuc, A.; Zibouche, N.; Heine, T. Influence of Quantum Confinement on the Electronic Structure of the Transition Metal Sulfide  $TS_2$ . *Phys. Rev. B* **2011**, *83*, 245213.
- (12) Splendiani, A.; Sun, L.; Zhang, Y.; Li, T.; Kim, J.; Chim, C.-Y.; Galli, G.; Wang, F. Emerging Photoluminescence in Monolayer  $MoS_2$ . *Nano Lett.* **2010**, *10*, 1271–1275.
- (13) Mak, K. F.; Lee, C.; Hone, J.; Shan, J.; Heinz, T. F. Atomically Thin  $MoS_2$ : A New Direct-Gap Semiconductor. *Phys. Rev. Lett.* **2010**, *105*, 136805.
- (14) Coehoorn, R.; Haas, C.; de Groot, R. A. Electronic Structure of  $MoSe_2$ ,  $MoS_2$ , and  $WSe_2$ . II. The Nature of the Optical Band Gaps. *Phys. Rev. B* **1987**, *35*, 6203–6206.
- (15) Eda, G.; Yamaguchi, H.; Voiry, D.; Fujita, T.; Chen, M.; Chhowalla, M. Photoluminescence from Chemically Exfoliated  $MoS_2$ . *Nano Lett.* **2011**, *11*, 5111–5116.
- (16) Kutana, A.; Penev, E. S.; Yakobson, B. I. Engineering Electronic Properties of Layered Transition-Metal Dichalcogenide Compounds through Alloying. *Nanoscale* **2014**, *6*, 5820–5825.
- (17) Li, H.; Duan, X.; Wu, X.; Zhuang, X.; Zhou, H.; Zhang, Q.; Zhu, X.; Hu, W.; Ren, P.; Guo, P.; Ma, L.; Fan, X.; Wang, X.; Xu, J.; Pan, A.; Duan, X. Growth of Alloy  $MoS_{2x}Se_{2(1-x)}$  Nanosheets with Fully Tunable Chemical Compositions and Optical Properties. *J. Am. Chem. Soc.* **2014**, *136*, 3756–3759.
- (18) Zhang, W.; Li, X.; Jiang, T.; Song, J.; Lin, Y.; Zhu, L.; Xu, X. CVD Synthesis of  $Mo_{(1-x)}W_xS_2$  and  $MoS_{2(1-x)}Se_{2x}$  Alloy Monolayers Aimed at Tuning the Bandgap of Molybdenum Disulfide. *Nanoscale* **2015**, *7*, 13554–13560.
- (19) Xi, J.; Zhao, T.; Wang, D.; Shuai, Z. Tunable Electronic Properties of Two-Dimensional Transition Metal Dichalcogenide Alloys: A First-Principles Prediction. *J. Phys. Chem. Lett.* **2014**, *5*, 285–291.
- (20) Beard, M. C.; Luther, J. M.; Semonin, O. E.; Nozik, A. J. Third Generation Photovoltaics Based on Multiple Exciton Generation in Quantum Confined Semiconductors. *Acc. Chem. Res.* **2013**, *46*, 1252–1260.

- (21) Hanna, M. C.; Beard, M. C.; Nozik, A. J. Effect of Solar Concentration on the Thermodynamic Power Conversion Efficiency of Quantum-Dot Solar Cells Exhibiting Multiple Exciton Generation. *J. Phys. Chem. Lett.* **2012**, *3*, 2857–2862.
- (22) Shockley, W.; Queisser, H. J. Detailed Balance Limit of Efficiency of p-n Junction Solar Cells. *J. Appl. Phys.* **1961**, *32*, 510–519.
- (23) Kulkarni, A.; Evers, W. H.; Tomić, S.; Beard, M. C.; Vanmaekelbergh, D.; Siebbeles, L. D. A. Efficient Steplike Carrier Multiplication in Percolative Networks of Epitaxially Connected PbSe Nanocrystals. *ACS Nano* **2018**, *12*, 378–384.
- (24) Aerts, M.; Bielewicz, T.; Klinke, C.; Grozema, F. C.; Houtepen, A. J.; Schins, J. M.; Siebbeles, L. D. A. Highly Efficient Carrier Multiplication in PbS Nanosheets. *Nat. Commun.* **2014**, *5*, 3789.
- (25) Ellingson, R. J.; Beard, M. C.; Johnson, J. C.; Yu, P.; Micic, O. I.; Nozik, A. J.; Shabaev, A.; Efros, A. L. Highly Efficient Multiple Exciton Generation in Colloidal PbSe and PbS Quantum Dots. *Nano Lett.* **2005**, *5*, 865–871.
- (26) Nair, G.; Bawendi, M. G. Carrier Multiplication Yields of CdSe and CdTe Nanocrystals by Transient Photoluminescence Spectroscopy. *Phys. Rev. B* **2007**, *76*, 081304.
- (27) Schaller, R. D.; Petruska, M. A.; Klimov, V. I. Effect of Electronic Structure on Carrier Multiplication Efficiency: Comparative Study of PbSe and CdSe Nanocrystals. *Appl. Phys. Lett.* **2005**, *87*, 253102.
- (28) de Weerd, C.; Gomez, L.; Capretti, A.; Lebrun, D. M.; Matsubara, E.; Lin, J.; Ashida, M.; Spoor, F. C. M.; Siebbeles, L. D. A.; Houtepen, A. J.; Suenaga, K.; Fujiwara, Y.; Gregorkiewicz, T. Efficient Carrier Multiplication in CsPbI<sub>3</sub> Perovskite Nanocrystals. *Nat. Commun.* **2018**, *9*, 4199.
- (29) Maiti, S.; Ferro, S.; Poonia, D.; Ehrler, B.; Kinge, S.; Siebbeles, L. D. A. Efficient Carrier Multiplication in Low Band Gap Mixed Sn/Pb Halide Perovskites. *J. Phys. Chem. Lett.* **2020**, *11*, 6146–6149.
- (30) Trinh, M. T.; Limpens, R.; de Boer, W. D. A. M.; Schins, J. M.; Siebbeles, L. D. A.; Gregorkiewicz, T. Direct Generation of Multiple Excitons in Adjacent Silicon Nanocrystals Revealed by Induced Absorption. *Nat. Photonics* **2012**, *6*, 316–321.

- (31) Beard, M. C.; Knutsen, K. P.; Yu, P.; Luther, J. M.; Song, Q.; Metzger, W. K.; Ellingson, R. J.; Nozik, A. J. Multiple Exciton Generation in Colloidal Silicon Nanocrystals. *Nano Lett.* **2007**, *7*, 2506–2512.
- (32) Stolle, C. J.; Lu, X.; Yu, Y.; Schaller, R. D.; Korgel, B. A. Efficient Carrier Multiplication in Colloidal Silicon Nanorods. *Nano Lett.* **2017**, *17*, 5580–5586.
- (33) Chaves, A.; Azadani, J. G.; Alsalman, H.; da Costa, D. R.; Frisenda, R.; Chaves, A. J.; Song, S. H.; Kim, Y. D.; He, D.; Zhou, J.; Castellanos-Gomez, A.; Peeters, F. M.; Liu, Z.; Hinkle, C. L.; Oh, S.-H.; Ye, P. D.; Koester, S. J.; Lee, Y. H.; Avouris, P.; Wang, X.; Low, T. Bandgap Engineering of Two-Dimensional Semiconductor Materials. *Npj 2D Mater. Appl.* **2020**, *4*, 1–21.
- (34) Zheng, W.; Bonn, M.; Wang, H. I. Photoconductivity Multiplication in Semiconducting Few-Layer MoTe<sub>2</sub>. *Nano Lett.* **2020**, *20*, 5807–5813.
- (35) Kim, J.-H.; Bergren, M. R.; Park, J. C.; Adhikari, S.; Lorke, M.; Frauenheim, T.; Choe, D.-H.; Kim, B.; Choi, H.; Gregorkiewicz, T.; Lee, Y. H. Carrier Multiplication in van Der Waals Layered Transition Metal Dichalcogenides. *Nat. Commun.* **2019**, *10*.
- (36) Li, T.; Zhang, Z.; Zheng, W.; Lv, Y.; Huang, F. A Possible High-Mobility Signal in Bulk MoTe<sub>2</sub>: Temperature Independent Weak Phonon Decay. *AIP Adv.* **2016**, *6*, 115207.
- (37) Helmrich, S.; Schneider, R.; Achtstein, A. W.; Arora, A.; Herzog, B.; Vasconcellos, S. M. de; Kolarczik, M.; Schöps, O.; Bratschitsch, R.; Woggon, U.; Owschimikow, N. Exciton–Phonon Coupling in Mono- and Bilayer MoTe<sub>2</sub>. *2D Mater.* **2018**, *5*, 045007.
- (38) Makino, K.; Saito, Y.; Horii, S.; Fons, P.; Kolobov, A.; Ando, A.; Ueno, K.; Mondal, R.; Hase, M. Ultrafast Dynamics of Electron-Phonon Coupling in Transition-Metal Dichalcogenides. *ArXiv Prepr. ArXiv180710879* **2018**.
- (39) Weerdenburg, S. A Theoretical Study on Charge Carrier Multiplication in 2H-MoTe<sub>2</sub>. Master of Science, Delft University of Technology, The Netherlands, **2022**.
- (40) Schaller, R. D.; Pietryga, J. M.; Klimov, V. I. Carrier Multiplication in InAs Nanocrystal Quantum Dots with an Onset Defined by the Energy Conservation Limit. *Nano Lett.* **2007**, *7*, 3469–3476.

(41) Cirloganu, C. M.; Padilha, L. A.; Lin, Q.; Makarov, N. S.; Velizhanin, K. A.; Luo, H.; Robel, I.; Pietryga, J. M.; Klimov, V. I. Enhanced Carrier Multiplication in Engineered Quasi-Type-II Quantum Dots. *Nat. Commun.* **2014**, *5*, 4148.

(42) Gachet, D.; Avidan, A.; Pinkas, I.; Oron, D. An Upper Bound to Carrier Multiplication Efficiency in Type II Colloidal Quantum Dots. *Nano Lett.* **2010**, *10*, 164–170.

(43) Berera, R.; van Grondelle, R.; Kennis, J. T. M. Ultrafast Transient Absorption Spectroscopy: Principles and Application to Photosynthetic Systems. *Photosynth. Res.* **2009**, *101*, 105–118.

(44) Kunneman, L. T.; Zanella, M.; Manna, L.; Siebbeles, L. D. A.; Schins, J. M. Mobility and Spatial Distribution of Photoexcited Electrons in CdSe/CdS Nanorods. *J. Phys. Chem. C* **2013**, *117*, 3146–3151.

(45) Evers, W. H.; Schins, J. M.; Aerts, M.; Kulkarni, A.; Capiod, P.; Berthe, M.; Grandidier, B.; Delerue, C.; van der Zant, H. S. J.; van Overbeek, C.; Peters, J. L.; Vanmaekelbergh, D.; Siebbeles, L. D. A. High Charge Mobility in Two-Dimensional Percolative Networks of PbSe Quantum Dots Connected by Atomic Bonds. *Nat. Commun.* **2015**, *6*, 8195.

(46) Lauth, J.; Failla, M.; Klein, E.; Klinker, C.; Kinge, S.; Siebbeles, L. D. A. Photoexcitation of PbS Nanosheets Leads to Highly Mobile Charge Carriers and Stable Excitons. *Nanoscale* **2019**, *11*, 21569–21576.

(47) Ulbricht, R.; Hendry, E.; Shan, J.; Heinz, T. F.; Bonn, M. Carrier Dynamics in Semiconductors Studied with Time-Resolved Terahertz Spectroscopy. *Rev. Mod. Phys.* **2011**, *83*, 543–586.

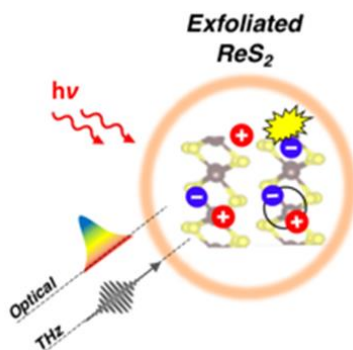
(48) Joyce, H. J.; Boland, J. L.; Davies, C. L.; Baig, S. A.; Johnston, M. B. A Review of the Electrical Properties of Semiconductor Nanowires: Insights Gained from Terahertz Conductivity Spectroscopy. *Semicond. Sci. Technol.* **2016**, *31*, 103003.

(49) Smith, N. Classical Generalization of the Drude Formula for the Optical Conductivity. *Phys. Rev. B* **2001**, *64*, 155106.

(50) Cocker, T. L.; Baillie, D.; Buruma, M.; Titova, L. V.; Sydora, R. D.; Marsiglio, F.; Hegmann, F. A. Microscopic Origin of the Drude-Smith Model. *Phys. Rev. B* **2017**, *96*, 205439.

## Chapter 2

### Unraveling the Photophysics of Liquid-Phase Exfoliated Two-Dimensional ReS<sub>2</sub> Nanoflakes



Based on:

#### Unraveling the Photophysics of Liquid-Phase Exfoliated Two-Dimensional ReS<sub>2</sub> Nanoflakes

Pieter Schiettecatte, Deepika Poonia, Ivo Tanghe, Sourav Maiti, Michele Failla, Sachin Kinge, Zeger Hens, Laurens D.A. Siebbeles, and Pieter Geiregat

J. Phys. Chem. C 2021, 125, 38, 20993–21002

## 2.1 Introduction

Over the past few years, layered rhenium chalcogenide compounds have gained significant interest in the scientific community due to their anisotropic electronic and optoelectronic properties.<sup>1</sup> Rhenium disulfide ( $\text{ReS}_2$ ) exhibits layer-independent optical properties due to electronically and vibrationally decoupled monolayers.<sup>2,3</sup> Among several implications, the possible preservation of a direct electronic bandgap for thicker stacks sets  $\text{ReS}_2$  apart from more conventional transition metal dichalcogenides (TMDs), which suffer from indirect bandgaps for multi-layered stacks.<sup>2,4-6</sup>  $\text{ReS}_2$  has shown great potential for transistors,<sup>7-9</sup> photodetectors,<sup>10-12</sup> light-emitting diodes<sup>13</sup> and sensors.<sup>14</sup> Unlike conventional two-dimensional (2D) semiconductors,  $\text{ReS}_2$  has a stable distorted  $1T'$  crystal structure and shows in-plane<sup>15,16</sup> and out-of-plane anisotropy.<sup>17,18</sup> This results in the formation of anisotropic excitons, and as a consequence, their fundamental properties, such as transport and <sup>19</sup> lifetimes, can be selectively modulated by varying the polarization of incident light.

Similar to other layered semiconductors,  $\text{ReS}_2$  can be produced either through vacuum epitaxial growth, exfoliation from high-quality crystals, or direct colloidal synthesis.<sup>20-23</sup> Exfoliation, particularly through liquid-phase methods, is a cost-effective means to produce flakes of  $\text{ReS}_2$  as it combines the advantages of solution processing (low cost and upscaling) while preserving high crystallinity, a persistent issue in direct colloidal synthesis methods.<sup>24-26</sup> An in-depth study of the synthesis of crystalline few-layered  $\text{ReS}_2$  flakes through liquid-phase exfoliation has been reported recently, and first reports indicate their promising potential for PV applications.<sup>27,28</sup> Although high-quality  $\text{ReS}_2$  nanoflakes obtained through such exfoliation procedures are clearly promising materials, the nature and dynamics of elementary optical excitations in these novel materials are not yet known, limiting their potential use in applications such as light emission or photovoltaics.

In this chapter, we report the temporal evolution of photogenerated excitons and free charge carriers in highly crystalline liquid-phase exfoliated 2D  $\text{ReS}_2$  nanoflakes with few-monolayer thicknesses. We photoexcited the sample with ultrashort optical laser pulses and detected excitons and free charge carriers by both time-resolved optical probe and terahertz (THz) probe (conductivity) measurements.

## 2.2 Materials and methods

**Liquid-phase exfoliation of ReS<sub>2</sub> and film preparation.** Dispersions of ReS<sub>2</sub> were produced by liquid-phase exfoliation in N-methyl-2-pyrrolidone, as reported previously.<sup>27</sup> The ReS<sub>2</sub> film is prepared by drop-casting ReS<sub>2</sub> dispersion on a quartz substrate. The thickness of the ReS<sub>2</sub> film is 57 nm, details appendix A2.1.

**Transient absorption (TA) spectroscopy.** TA measurements were performed on the ReS<sub>2</sub> film over a span of several months. The pump-induced change in absorbance is calculated using  $\Delta A = \log_{10}\left(\frac{I_{\text{off}}}{I_{\text{on}}}\right)$ . Here,  $I$  is the incident light on the detector with either pump on or pump off. The details of the setup is in chapter 1. In the present measurements, differential reflectance is not considered, and hence, differential transmittance is considered equal to differential absorbance.

**Optical pump-THz probe (OPTP) spectroscopy.** The details of the THz setup and working principles are discussed in chapter 1.

## 2.3 Results and discussion

**Linear and Transient Absorption Spectroscopy.** Figure 2.1a (red trace) shows the linear optical absorbance spectrum of a ReS<sub>2</sub> film on quartz. The dashed black line indicates a fit with a polynomial background and an exciton absorption profile centered at 1.51 eV (820 nm).

The color map of Figure 2.1b provides a general overview of the TA spectroscopy data of ReS<sub>2</sub> film after photoexcitation with a 2.34 eV (530 nm) 180 fs pump pulse and interrogation by a broadband probe spanning the energy range from 1.4 eV (880 nm) up to 2.4 eV (515 nm). The bandgap region shows a complex interplay of spectral effects, as shown in Figure 2.2a. We observe an interplay of different phenomena, such as exciton profile broadening or shifts, that can superimpose on a negative TA signal ( $\Delta A < 0$ ) due to stimulated emission (SE) or bleach due to state-filling. A description of the effects of line shape shifts and broadening on  $\Delta A$  spectra is provided, appendix A2.2, yet Figure 2.2b summarizes the main effects on a Gaussian transition lineshape. To analyze the 2D TA map based on these qualitative concepts, we present spectral slices of  $\Delta A$  at distinct pump-probe time delays in Figure 2.2c.

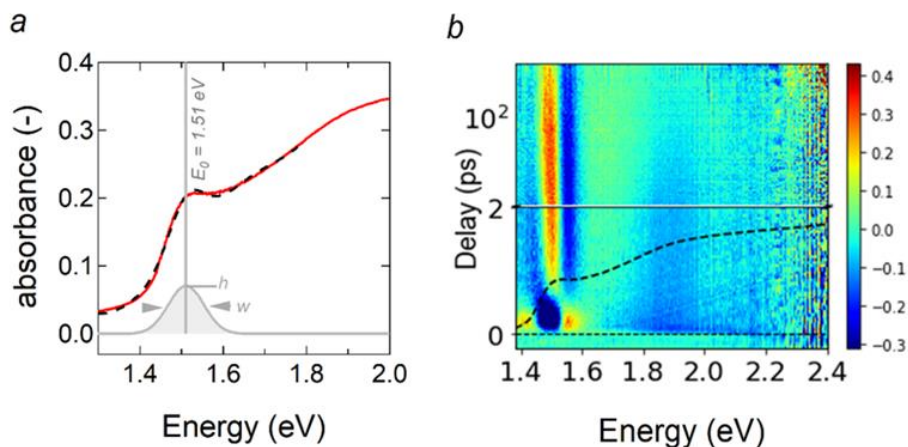


**Figure 2.1** (a) Linear absorbance spectrum (red) of a thin film of ReS<sub>2</sub> nanoflakes obtained after dropcasting on quartz. The dashed black line reveals a fit of the absorbance spectrum, using a background with an exciton absorption profile centered at 1.51 eV (820 nm, grey shaded area) superimposed. The exciton profile is characterized by a width ' $w$ ', an amplitude ' $h$ ' and a central position  $E_{x,0}$ . (b) Overview of the transient absorbance  $\Delta A$  recorded after a film of ReS<sub>2</sub> on quartz was photoexcited with a 180 fs pump pulse with photon energy 2.34 eV and absorbed photon fluence  $1.2 \times 10^{13}$  photons  $\text{cm}^{-2}$  per pump pulse. The black dashed curve represents the linear absorbance spectrum.

Immediately after photo-excitation (spectrum i,  $t = 200$  fs), the spectrum exhibits a bleach ( $\Delta A < 0$ ) around the exciton profile sided by two positive photo-induced absorptions (PA,  $\Delta A > 0$ ). We recognize such a second-derivative-like line shape as a combination of SE and/or state-filling induced bleach with a broadening of a Gaussian absorption profile; see Figure 2.2b ( $\Delta w > 0$ , bottom right) and appendix A2.2. The bleach minimum is slightly offset towards lower energy, and the PA band appears more intense at the higher energy side. These asymmetries are likely the result of a blue-shifted exciton absorption line after the pump pulse, i.e., a shift towards higher energy; see Figure 2.2b ( $\Delta E > 0$ , top right). At higher probe photon energy ( $> 1.65$  eV), the  $\Delta A$  spectrum shows a net negative signal, where the ground state absorbance  $A_0$  has a relatively uniform slope up to 2.4 eV; see dashed curve in Figure 2.1b and Figure A2.1. Considering the extent of the negative band, it is unlikely to result from state-filling but presumably reflects a blue-shift of the higher-lying energy states.

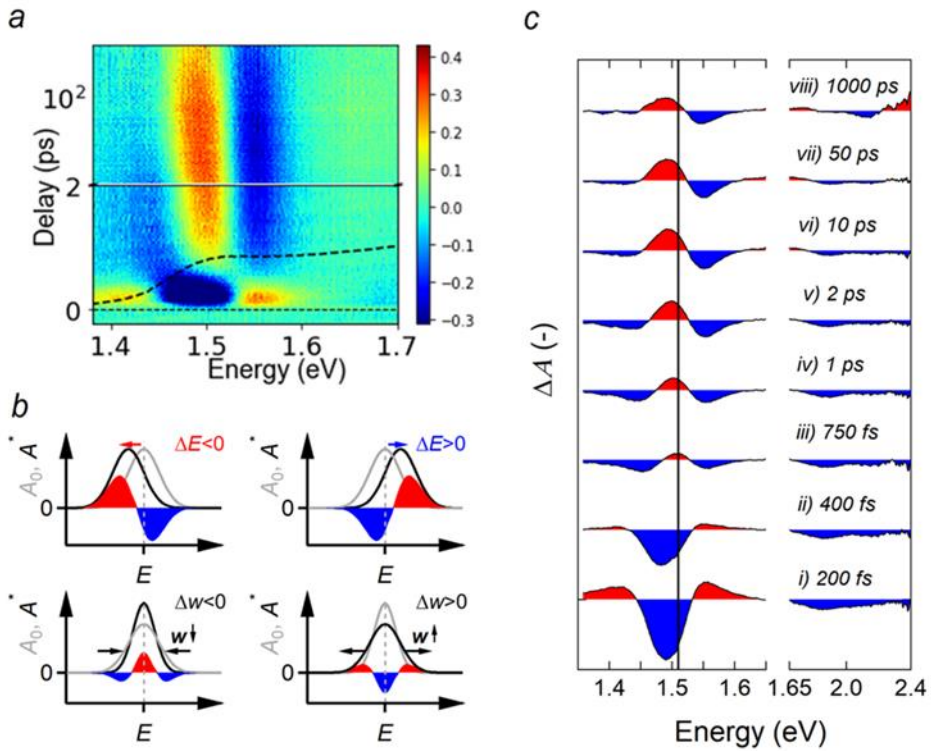


**Figure 2.2.** Overview of the transient absorbance  $\Delta A$  spectroscopy in the bandgap region around 1.51 eV (820 nm) (a) Zoom view of the 2D energy-delay map of  $\Delta A$  under similar excitation conditions as Figure 2.1, showing a complex interplay between several spectral effects shown in (b). The black dashed curve again represents the linear absorbance spectrum. (b) Schematics of pump-induced effects on a Gaussian-shaped optical transition (from left to right and top to bottom): spectral red-shift ( $\Delta E < 0$ ), spectral blue-shift ( $\Delta E > 0$ ), linewidth narrowing ( $\Delta w < 0$ ), and linewidth broadening ( $\Delta w > 0$ ). (c) Transient absorbance spectra at time delays as indicated, plotted at an offset. For clarity, negative values of  $\Delta A$  are filled in blue and positive values of  $\Delta A$  are filled in red.

Most remarkably, while decaying, the signal at the band edge switches sign over the next few hundreds of femtoseconds (spectra ii-iv) and yields a clear photo-induced absorption sided by two bleach bands at a delay of 1 ps (spectrum iv). Such a feature reflects a narrowed exciton profile after photoexcitation of the sample, i.e., the probe photon produces an exciton with a narrower linewidth than the exciton in the ground state absorption spectrum; see Figure 2.2b ( $\Delta w < 0$ , bottom left). At a delay of 750 fs (spectrum iii), the line shape is asymmetric, with a more intense negative tailing at lower energy, i.e., a shift to higher energy is superimposed on a narrowed exciton profile. At a delay of 1 ps (spectrum iv), the  $\Delta A$  feature is

symmetric, while at pump-probe delays longer than 1 ps (spectra v-vi), the symmetry is reversed, and the initial blue-shift has decayed into a red-shift; a process evidenced by a less intense tailing at lower energies and a shift of the PA maximum to the red side.

At higher energy  $> 1.65$  eV, the blue-shifted continuum absorption has mostly decayed and even yields a slight red-shift at decays longer than  $\sim 10$  ps (spectrum vi), a signature we recognize through the rise of a positive absorption band between 1.6 - 1.7 eV. In contrast, the signature at the band edge decays over a much longer time scale. While decaying (spectra vi-viii), the peak maximum in the  $\Delta A$  progressively shifts to the lower energy and obtains a sinusoidal-like shape, which is characteristic of a spectral red-shift of an absorption peak; see Figure 2.2b ( $\Delta E < 0$ , top left). In summary, we recognize two dominant regimes in the  $\Delta A$  map:

Regime I,  $< 3$  ps: After photoexcitation, the exciton band broadens and blue-shifts. At the same time, we observe a blue-shift of the higher-lying energy states.

Regime II,  $> 3$  ps - 1 ns: The initially broadened and blue-shifted exciton transition decays into its mirror image, i.e., it narrows down and shifts to the red. At the same time, the blue-shifted higher-lying states gradually decay.

**Optical pump Terahertz probe spectroscopy.** Having established two distinct regimes of TA dynamics in ReS<sub>2</sub>, we now proceed to providing insights into the nature of photogenerated charges, be it unbound carriers and/or excitons, that are present in each regime and how their presence could induce the observed spectral broadening and shifts in both regimes. The usually very large binding energy of excitons in 2D materials, e.g. reported as 117 meV<sup>38</sup> for ReS<sub>2</sub>, suggest the dominance of tightly bound excitons after energetic relaxation of initially unbound charge carriers produced by the pump laser pulse. However, trapping due to defects and binding energy reduction due to dielectric screening resulting from the presence of free or trapped charge carriers both result in a shift of the balance from excitons towards charge carriers. To evaluate the presence and nature of photogenerated free charges versus excitons after photoexcitation, we first measured the differential transmission terahertz signal after photoexcitation at a pump photon energy of 3.1 eV (400 nm). Analogous to previous work, we consider the complex THz conductivity signal,  $S(t)$ , averaged over frequencies ( $\nu$ ) in the range of 0.6 - 1.1 THz, which is given by<sup>37</sup>

$$S(t) = \phi_{e,h}(t)\mu_{e,h} + \phi_{EX}(t)\mu_{EX} \quad 2.1$$

In the first term of Equation 2.1,  $\phi_{e,h}(t)$  is the time-dependent quantum yields of free mobile charges, and  $\mu_{e,h}$  is the sum of the complex-valued mobility of electrons and holes. The real and imaginary components of  $\mu_{e,h}$  are due to the motion of charges with velocity in-phase and out-of-phase with respect to the THz field, respectively.<sup>39,40</sup> The second term in Equation 2.1 takes into account the contribution of excitons with quantum yield  $\phi_{EX}(t)$  and polarizability,  $\alpha$ , which at a single radian frequency of the THz field ( $\omega$ ) is given by  $\alpha = -eIm(\mu_{EX})/\omega$ .<sup>37</sup>

The red curve in Figure 2.3a, due to the real THz conductivity signal from free charges, exhibits an initial fast decay over a time scale of *ca.* 3 ps at an absorbed photon density of  $1.1 \times 10^{13}$  photons  $\text{cm}^{-2}$ , which is comparable to the initial variation of the TA spectrum, see Figure 2.2a-c. Taking the initial measured value of  $S_R(t) = 10 \text{ cm}^2/\text{Vs}$  (Figure 2.3a) and assuming the reported electron mobility values for bulk ReS<sub>2</sub> in the range  $19\text{-}34 \text{ cm}^2/\text{Vs}$ <sup>41-43</sup> to be comparable to the hole mobility,<sup>41</sup> we estimate the quantum yield of free pairs of electrons and holes to be in the range  $\phi_{e,h}(t=0) = 0.20 \pm 0.05$ , see Equation 2.1. After 3 ps, the remaining signal decays on a much longer time scale of several hundreds of picoseconds, possibly due to trapping of remaining charges.

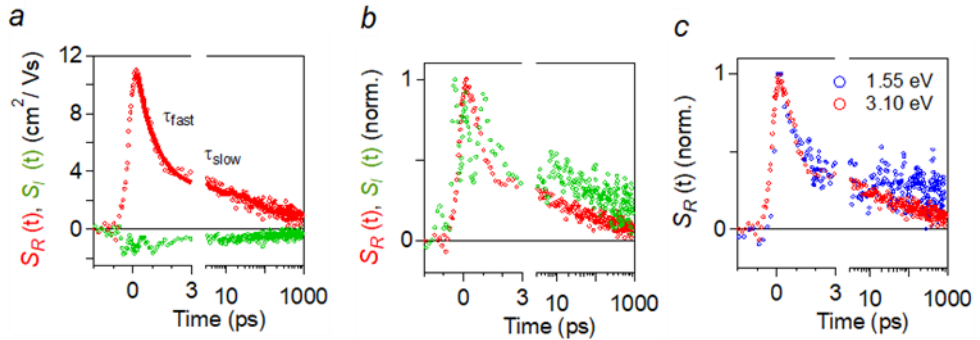


**Figure 2.3.** (a) Real and imaginary THz conductivity signal as a function of time obtained after photoexcitation with 3.1 eV energy and at an absorbed photon density  $N_a = 1.1 \times 10^{13} \text{ cm}^{-2}$ . The solid red curve is a bi-exponential fit revealing a fast and slow decay time constant; see also Figure 2.5. (b) Normalized kinetics of Figure 2.3a to show the common decay channel for both real and imaginary parts of the conductivity. (c) Normalized kinetics of the real conductivity after photoexcitation with 1.55 eV (800 nm, red) pulses, resonant with the bandgap, together with the off-resonant case (3.1 eV, blue) for a comparable absorbed photon flux.

The green curve in Figure 2.3a represents the imaginary component due to the motion of free charges with a velocity component that is out-of-phase with the applied THz field and/or the polarizability of free excitons.<sup>37,39,40</sup> However, we can show that the exciton polarizability is too small to contribute to the THz conductivity signal due to the experimental detection limit (see appendix A2.3). Therefore, we attribute the observed small imaginary component to backscattering of free charges from randomly oriented stacks of ReS<sub>2</sub> flakes and possibly also from localized trap charges, as further discussed in appendix A2.4. When normalized and plotted on top of each other in Figure 2.3b, the real and imaginary THz conductivity signals follow the same decay kinetics, which strongly corroborates that the real and imaginary components originate from the same species; i.e., unbound or ‘free’ charges. When pumping at 800 nm (1.55 eV), no excess energy is provided to the charges, and excitons should be formed straight away. The THz transient overlays however perfectly with the 400 nm pump as is shown in Figure 2.3c. We hence, conclude that a significant population of unbound charge carriers are present, in addition to weakly polarizable excitons, which will dominate the response of the nanoflakes.

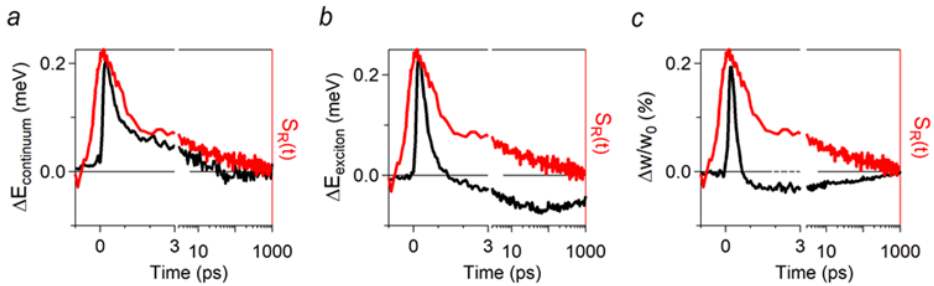


**Figure 2.4.** Evolution of the fit parameters (solid black lines) obtained from a fit of a Gaussian  $G(h, E_{\text{exciton}}, w)$  with the constrained area and a background absorbance  $C(E)$  to the  $\Delta A$  in Figure 2.1b, including (a) the shift of the background absorbance  $\Delta E_{\text{bck}}$  and, (b) the energy shift of the exciton  $\Delta E_{\text{exciton}} = E_X(t) - E_{X,0}$ , and (c) the normalized change in the width  $\Delta w/w_0$ .

By combining a qualitative assessment of the  $\Delta A$  maps (Figure 2.2) and THz spectroscopy (Figure 2.3), we have identified two distinct time regimes of free or trapped charge carrier dynamics. To complete this analysis and compare THz to TA dynamics directly, we note that extracting reliable information from the complex and broadband 2D TA map based on slices at fixed probe energies is prone to error. To better quantify the complex interplay of spectral effects that govern the free carrier dominated TA response in the two-time regimes, we proceed to fit  $\Delta A(E, t)$  to a Gaussian fit function  $G(h, E_{\text{exciton}}, w)$ , that accounts for the exciton absorption,

and a background absorbance  $C(E)$  attributed to higher energy states (see appendix A2.5). Using this procedure, we extract, for each pump-probe time delay the amplitude  $h(t)$ , the spectral position  $E_{\text{exciton}}(t)$ , and the width  $w(t)$  of the Gaussian that describes the exciton band, similar as in Figure 2.1a, and a shift of the background absorbance spectrum  $\Delta E_{\text{bck}}$ . Next, we translate these into differential quantities:  $\Delta E_{\text{exciton}}$ ,  $\Delta w$ , and  $\Delta E_{\text{bck}}$ . The results of this quantitative analysis of the  $\Delta A$  maps, as shown in Figures 2.4a-c, reproduce the qualitative assessment put forward earlier, i.e., the complex spectral response is a result of an interplay between line width changes and spectral shifts and is split into two time regimes. Remarkably, the temporal evolution of the spectral parameters  $\Delta E_{\text{exciton}}$ ,  $\Delta w$ , and  $\Delta E_{\text{bck}}$  coincides quite well with the decay of the real component of the THz conductivity shown in Figure 2.3a and overlaid in Figures 2.4a-c (red curve). A single exponential fit reveals time constants of 0.47 ps and 0.42 ps for  $\Delta E_{\text{exciton}}$ , and  $\Delta E_{\text{bck}}$  respectively, and a 0.27 ps time constant for  $\Delta w$ . The slower rise and *ca.* 1 ps decay of the THz conductivity signal is due to the lower time resolution of OPTP measurements as compared to TA spectroscopy.

**Carrier dynamics.** Remarkably, the decay of the carrier population is independent of carrier density, as is evidenced by the decay traces of the real THz conductivity in Figure 2.5a over an order of magnitude in pump fluence. A double-exponential fit to the full decay reveals two lifetimes:  $\tau_{\text{fast}} = 0.94$  ps and  $\tau_{\text{slow}} = 88$  ps, see Figure 2.5b. We use the fast component, which is limited by the OPTP time resolution, as a tentative ruler to set the regimes apart, i.e., after 3 decay constants (*ca.* 3 ps), we assume the effects of regime *I* are finished. Such fluence independent behavior was also observed in flakes of other TMD materials and typically points towards fast trapping of one charge carrier, followed by non-radiative recombination through a Shockley-Read-Hall as is shown in Figure 2.5c, bottom.<sup>24,25,44</sup>

**Regimes of charge recombination.** Based on the acquired TA and THz data analysis, we outline two time regimes, both of which are dominated by free mobile charge carriers, which are discussed in detail below, see also Figure 2.5c:

**Regime I (< 3 ps). Linewidth broadening and blue-shifts.** The optical pump generates predominantly free charge carriers that initially broaden the exciton resonance due to collisional broadening and blue-shift the exciton energy due to a free carrier screening mechanism (Figure 2.4a).

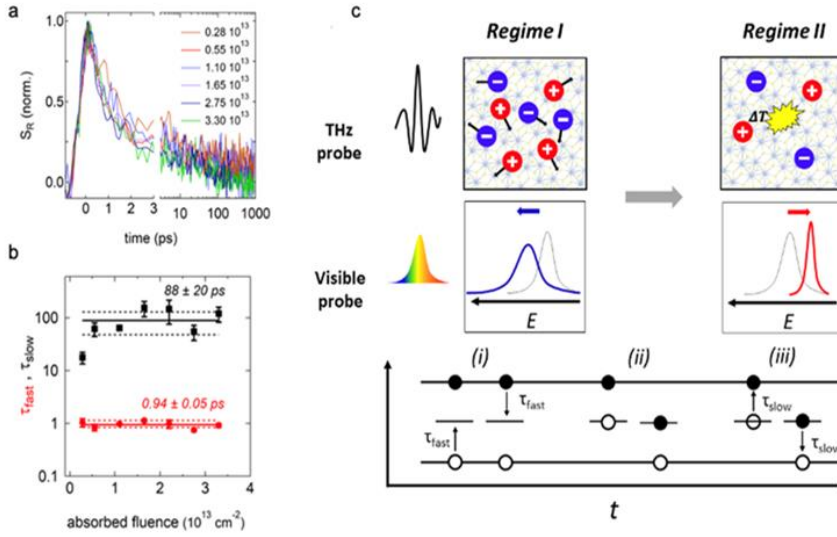


**Figure 2.5.** (a) Normalized decay traces of the real part of the THz conductivity, a metric for the charge population, for increasing absorbed photon density ( $0.28 \times 10^{13}$  -  $3.3 \times 10^{13} \text{ cm}^{-2}$ ). (b) The time constants extracted from a bi-exponential fit to (a) showing density-independent recombination dynamics for both fast (red,  $\tau_{\text{fast}} = 0.94 \text{ ps}$ ) and slow (black,  $\tau_{\text{slow}} = 88 \text{ ps}$ ) timescales. (c) Schematic summary representation of the proposed charge carrier generation and decay in liquid-phase exfoliated  $\text{ReS}_2$ , proceeding through two distinct regimes. An optical pump generates predominantly free mobile charge carriers, as evidenced by THz spectroscopy, that initially cause broadening and a blue-shift of the exciton profile due to collisional broadening and free carrier screening, respectively. Next, the broadened and blue-shifted transition decays into a peculiar narrowed, and red-shifted line profile on a similar timescale as the THz conductivity decays. The latter indicates a non-radiative recombination event giving rise to the observed spectral signatures, i.e., a red-shift due to heating or carrier-capture induced energetic red-shifts and a narrowing due to a homogenization of the energy landscape.

Collisional broadening is responsible for broadening spectral lines in atoms and molecules and absorption and emission lines in semiconductors.<sup>45–48</sup> In addition to the broadening, we also observe a blue-shift of the spectrum due to the screening of Coulomb forces, resulting in the reduction of the binding energy of excitons.<sup>49</sup> The central position of an exciton resonance  $E_X$  depends on the exciton binding energy,  $E_b$ , and the free-particle bandgap,  $E_g$ , such that  $E_X = E_g - E_b$ .<sup>50</sup> It is well-known that the presence of carriers alters the Coulomb potential experienced by electrons and holes. Screening of attractive electron-hole interactions decreases the exciton binding energy (binding energy reduction, BER), causing blue-shifts, while electron-

electron (exchange) interactions renormalize the bandgap (bandgap renormalization, BGR), causing red-shifts.<sup>51,52</sup> Both mechanisms work in spectrally opposite directions yet do not fully compensate in general. As such, screening either results in a blue or a red-shift of the exciton profile.<sup>53</sup> For instance, blue-shifted exciton transitions as a result of screening have been observed in quasi-2D QWs,<sup>46,47,53,54</sup> atomically thin TMDs,<sup>48,49,55</sup> and 2D layered perovskites.<sup>56</sup> In MoS<sub>2</sub>,<sup>48</sup> and WS<sub>2</sub>,<sup>49,55</sup> blue-shifts at early delays were always accompanied by a broadening, similar to our observations.

It is worth mentioning that studies typically focus on the lowest-lying exciton state and rarely address the higher-lying energy levels within this context. This makes it more challenging to rationalize a blue-shift of the absorption of the higher-lying energy states. Theoretical work addressing the broadband optical response of MoS<sub>2</sub> in the presence of excited carriers showed a clear difference between the excitonic response and the higher energy C band absorption. While the excitons engaged in a distinctive competitive behavior between the BGR and BER, the C peak was relatively stable against increasing carrier densities and even showed signs of a small blue-shift.<sup>57</sup> In this regard, Steinhoff *et al.*<sup>57</sup> suggest that an interpretation of higher-lying energy states is far from trivial.

**Regime II (> 3 ps – 1 ns). Red-shifts and linewidth narrowing.** The initial line broadening and blue-shift exhibit a cross-over into a peculiar narrowing and red-shift on the same timescale as the THz conductivity decreases. Figure 2.6a shows the TA spectra at a long time delay, indicating a dominant red-shift ( $\Delta E_{\text{exciton}} < 0$ ), see Figure 2.6b, that persists up to 1 ns (Figures 2.6a-b) and scales linearly with the photon flux, see Figure 2.6c. In addition, such an analysis reveals a dominant linear scaling of the exciton linewidth  $\Delta w$  and the shift of background absorbance  $\Delta E_{\text{bck}}$  with the pump fluence (see appendix A2.6), an observation that again points to a common mechanistic origin. Such a transition from a blue to a red-shift has been observed in WS<sub>2</sub>.<sup>49,55</sup> In these studies, the cross-over was attributed to an initial blue-shift due to BER, followed by a red-shift due to lattice heating, arising from non-radiative recombination of electrons and holes on longer timescales. On the other hand, as outlined above, a decay of charge carriers due to recombination would also alter the intricate interplay between BER and BGR. Irrespective of whether the red-shift is induced by a temperature effect or by a variation in charge carrier density, tipping the balance between BER and BGR, both are due to the recombination of free mobile charge carriers, an interpretation in agreement with the decay of the

real THz conductivity signal. In addition, the linear dependence of the exciton shift with the pump fluence points to a trapping mechanism rather than to an Auger-like higher-order recombination mechanism.

As carrier-carrier scattering induces a broadening of the line, carrier loss inevitably reduces the width. While such a process accounts for the decay in broadening, it does not explain the small, albeit measurable, narrowing we observe afterward. A line narrowing might occur due to different mechanisms; nonetheless, they again all reflect non-radiative capture events:

**Homogenization of the local environment.** A line narrowing can be interpreted as a reduction of the inhomogeneous linewidth of the excitonic optical absorption profile, typically due to a homogenization of the environment. Such homogenization could arise from screening of parasitic in-plane electric fields arising from local potentials, *e.g.*, as a result of charged or ionized defects,<sup>58,59</sup> or due to pre-existing built-in fields. We note that such screening of internal electric fields by photogenerated free charges has been studied before by numerous authors on epitaxially grown semiconductor quantum wells.<sup>60–63</sup> The internal electric field in these 2D systems originated from the intrinsic piezoelectric property of the material. Unlike 2H TMDs, such as MoSe<sub>2</sub> and WSe<sub>2</sub>, ReS<sub>2</sub> crystallizes in a distorted 1T'-CdCl<sub>2</sub> lattice-type, similar to WTe<sub>2</sub>. Although a ReS<sub>2</sub> monolayer (unit cell) is centrosymmetric, exfoliated multi-layered stacks of ReS<sub>2</sub> are known to favor an anisotropic *AB* stacking order where one layer is shifted with respect to the other.<sup>17,18</sup> We, indeed, observed such a stacking order by Raman spectroscopy in our previous work.<sup>27</sup> In a similar case, Cobden and co-workers reported the presence of ferroelectricity in bilayer 1T'-WTe<sub>2</sub>, while it was absent in a monolayer.<sup>65</sup> This distinctive behavior stemmed from surface dipoles that arise due to the uniquely distorted 1T'-phase. This suggests that an internal field in ReS<sub>2</sub> is not unlikely.

Alternatively, Heinz and co-workers outlined that dielectric disorder is the dominant source of inhomogeneities in 2D materials<sup>66</sup> due to the strong effect on the exciton binding energy. Dielectric disorder originates from local fluctuations of the permittivity, for example, due to localized defects. But either by neutralizing internal or parasitic electric fields or by means of improving dielectric order, charge carrier capture into charged defects will always homogenize the energy landscape, thereby reducing inhomogeneous broadening and eventually narrowing the linewidth of the excitonic optical absorption profile.

**Interlayer coupling** - An alternative interpretation relates to the interlayer coupling in ReS<sub>2</sub>. It is well-known that interlayer interactions can broaden an exciton profile.<sup>17,64</sup> These effects are subtle, manifesting on changes of the interlayer distance less than 0.1 Angström. An excellent example is the existence of two dominant polytypes in ReS<sub>2</sub>, labeled as *AB* (anisotropic) and *AA* (isotropic).<sup>17,18</sup> Recently, it has been reported that spectral lines in the *AB* polytype are broader and blue-shifted with respect to *AA*.<sup>64</sup> These differences relate to the stronger interlayer coupling between stacked ReS<sub>2</sub> layers in the *AB* polytype – the dominant polytype present in the liquid-phase exfoliated ReS<sub>2</sub>.<sup>17,27</sup> In this respect, a sudden carrier capture event would locally polarize/charge the sheet and repel adjacent layers, reduces the interlayer coupling – thereby partially undoing differences between *AB* and *AA*. As a result, the excitonic absorption profile could narrow.

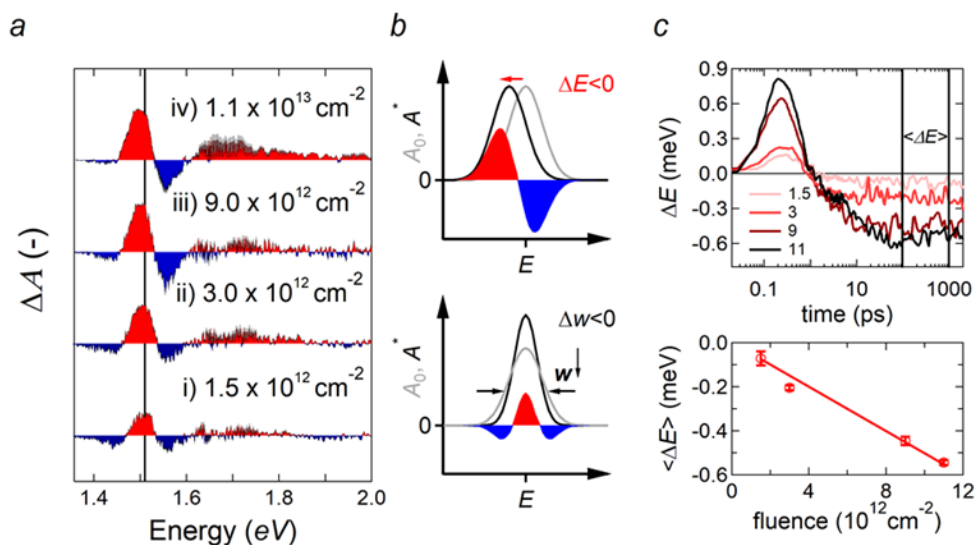


**Figure 2.6.** (a) The red-shift of the exciton peak for increasing absorbed pump fluence at a probe delay time of 1 ns. (b) Schematics depicting how a red-shift and line narrowing manifest in TA spectra. (c) (top) Evolution of the energy shift of the exciton obtained from Gaussian fit with a constrained area and background absorbance to fluence dependent  $\Delta A$  maps for increasing densities of  $1.5 \times 10^{12}$  to  $11 \times 10^{12} \text{ cm}^{-2}$ . (bottom) Averaged exciton energy shift  $\langle \Delta E \rangle$ , here averaged between 100 and 1000 picoseconds (see also (c), top graph), as a function of fluence. Markers represent experimental data points, and the solid curve is a linear fit through the origin.

## 2.4 Conclusions

In summary, we have analyzed the dynamics of photogenerated charge carriers in high-quality exfoliated ReS<sub>2</sub> nanoflakes using time-resolved pump-probe laser spectroscopy with optical and THz conductivity detection. We identified two distinct time regimes of charge carrier dynamics, both of which are dominated by responses due to unbound charge carriers. In the first time regime, free charge carriers induce collisional broadening of the exciton energy and a blue-shift due to screening of the electron-hole attraction. In the second time regime, peculiar line narrowing effects are identified, which could be due to charge carriers reducing effects of built-in fields or charged defects. Besides providing a toolbox to gain insights into a series of complex and interplaying optical nonlinearities in commonly used transient absorption spectroscopy of TMD materials, the generation of unbound and mobile charge carriers in such ultrathin materials is equally interesting from a practical point of view, as mobile charges are highly desired in photovoltaic devices or photodetectors.

## A2 Appendix to chapter 2

**A2.1 Optical absorption of the ReS<sub>2</sub> film.** We describe the absorbance spectrum of the film around the band edge by a Gaussian, accounting for the lowest-lying exciton transition, and a polynomial function, describing the background

$$f(E) = A \exp\left(-\frac{(E-E_0)^2}{w^2}\right) + \sum_{i=0}^8 C_i E^i \quad \text{A2.1}$$

A fit of the optical absorbance (solid red curve, Figure A2.1) to equation A2.1 (black dashed curve, Figure A2.1) yields an exciton resonance centered around  $E_0 = 1.511 \pm 0.001$  eV (grey curve, Figure A2.1). We estimate the thickness of the film  $t$  based on the optical absorbance  $A$  and the absorption coefficient ( $\alpha$ ) of rhenium disulphide

$$t = \frac{\ln 10 A}{\alpha} \quad \text{A2.2}$$

Using  $\alpha$  of  $8 \times 10^6 \text{ m}^{-1}$  at 1.5 eV, equation A2.2 yields a film thickness of 57 nm.

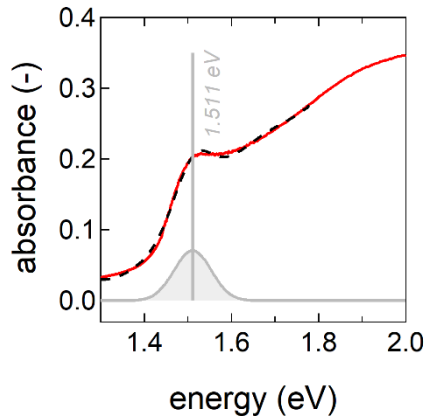


**Figure A2.1.** Characterization of the drop-casted ReS<sub>2</sub> film on a quartz substrate showing the optical absorption spectrum of the film (red). The black dashed line is a fit to equation A2.1, yielding a Gaussian-shaped exciton centered around  $E_0 = 1.511 \pm 0.001$  eV (grey).

## A2.2 Understanding broadening and spectral shifts via derivative analysis.

**Taylor approximations.** For a transient spectrum  $\Delta A$  determined by a spectral shift  $\delta E$ <sup>67</sup> or a change in the linewidth  $\Delta\sigma$ , we expect a proportionality between the first and second derivative of the linear absorbance  $A_0$  to the energy  $E$ .

$$\Delta A \approx \frac{dA_0}{dE} \delta E \quad \text{A2.3}$$

$$\Delta A \approx \frac{d^2 A}{dE^2} \sigma_0 \Delta\sigma \quad \text{A2.4}$$

We point out that equation A2.3 and equation A2.4 are derived by expanding  $\Delta A(x + \delta x)$ , where  $x = E, \sigma$  as a Taylor series up to the first order, and thereby only hold for infinitesimal increments  $\delta x$  (see mathematical detail below).

### Mathematical detail – Derivation of Taylor Series

**Proportionality between  $\Delta A$  and  $dA_0/dE$  in case of a Spectral Shift  $\delta\sigma$ .** In the case of a pure spectral shift  $\delta E$ , the nonlinear absorbance after photoexcitation  $A^*$  is a function of  $\delta E$ , and can be expanded through a Taylor series around the linear absorbance  $A_0$ :

$$A^* = A_0 + \frac{dA_0}{dE} \delta E + \frac{1}{2} \frac{d^2 A_0}{dE^2} \delta E^2 + \dots \quad \text{A2.5}$$

For sufficiently small values of  $\delta E$ , a Taylor expansion up to the first order yields a direct proportionality between the transient ( $\Delta A = A^* - A_0$ ) and the derivative of the linear absorbance  $dA_0/dE$ :

$$\Delta A \approx \frac{dA_0}{dE} \delta E \quad \text{A2.6}$$

Accordingly, a value for the spectral shift  $\delta E$  can be obtained from the ratio between the transient absorbance and the derivative of the linear absorbance spectrum. Figure A2.2 illustrates this proportionality between  $dA_0/dE$  and  $\Delta A$  in the case of a pure spectral shift.

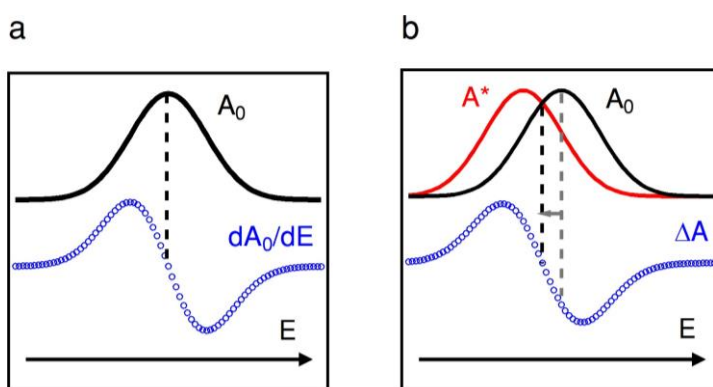


**Figure A2.2.** Pictorial representation showing the relationship between a derivative (a) and a spectral shift (b). A spectral shift closely resembles a derivative-like spectrum except that the inflection point is being slightly offset. The linear absorbance  $A_0$  is indicated in black, and the excited state absorbance  $A^*$  in red.

**Proportionality between  $\Delta A$  and  $d^2A_0/dE^2$  in Case of a Change in Linewidth  $\Delta\sigma$ .** In the case of a pure spectral broadening or narrowing  $\Delta\sigma$ , the nonlinear absorbance after photoexcitation  $A^*(\sigma)$  can be expanded as a Taylor series around the linear absorbance  $A_0(\sigma_0)$ :

$$A^*(\sigma_0 + \Delta\sigma) = A_0(\sigma_0) + \frac{dA_0}{d\sigma} \delta\sigma + \frac{1}{2} \frac{d^2A_0}{d\sigma^2} \delta\sigma^2 + \dots \quad \text{A2.7}$$

Here again, for small values of  $\Delta\sigma$ , the transient ( $\Delta A = A^* - A_0$ ) is directly proportional to the derivative of the linear absorbance to the linewidth  $dA_0/d\sigma$

$$A^*(\sigma_0 + \Delta\sigma) \approx A_0(\sigma_0) + \frac{dA_0}{d\sigma} \delta\sigma \quad \text{A2.8}$$

Approximating the absorbance spectrum  $A_0$  by a Gaussian function characterized by a spectral position  $E_0$  and a linewidth  $\sigma_0$ , the respective derivatives of  $A_0$  to  $\sigma_0$  and  $E$  are given by

$$\frac{dA_0}{d\sigma} = A_0 \frac{E_0^2 - \sigma_0^2}{\sigma_0^3} \quad \text{A2.9}$$

$$\frac{d^2A_0}{dE^2} = A_0 \frac{E_0^2 - \sigma_0^2}{\sigma_0^4} \quad \text{A2.10}$$

Combining equations A2.9 and A2.10, the equivalence between  $\frac{dA_0}{d\sigma}$  and  $\frac{d^2A_0}{dE^2}$  reads

$$\frac{dA_0}{d\sigma} = \frac{d^2A_0}{dE^2} \sigma_0 \quad \text{A2.11}$$

Through equations A2.8 and A2.11, the transient  $\Delta A$ , expressed as the difference between the nonlinear absorbance  $A^*(\sigma_0 + \Delta\sigma)$  and the linear absorbance  $A_0(\sigma_0)$ , now becomes

$$A^*(\sigma_0 + \Delta\sigma) - A_0(\sigma_0) \approx \frac{d^2A_0}{dE^2} \sigma_0 \Delta\sigma \quad \text{A2.12}$$

According to equation A2.12, a transient absorbance resulting from changes in linewidth has a one-to-one correlation with the second derivative of the linear absorbance spectrum to the energy, and the ratio between both functions yields a value for  $\sigma_0\Delta\sigma$ . Figure A2.3 illustrates this proportionality in the case of the broadening and the narrowing of a Gaussian.

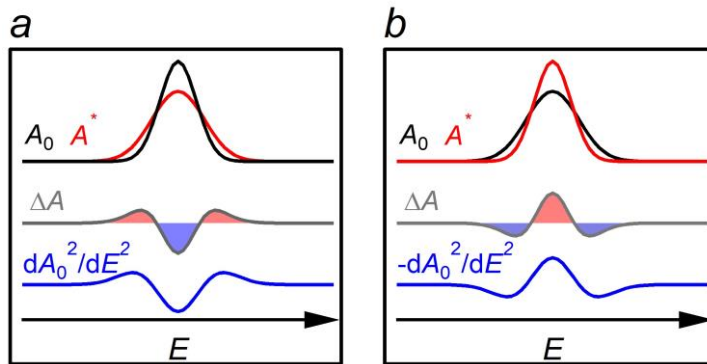


**Figure A2.3.** Pictorial representation depicting the relationship between (a) the broadening and (b) the narrowing of a Gaussian resonance, the difference spectrum  $\Delta A$  and the second derivative of  $A_0$  to  $E$ . The linear absorbance  $A_0$  is indicated in black, the excited state absorbance  $A^*$  in red, and the transient absorbance  $\Delta A$  in grey.

## Qualitative Analysis of the Transient $\Delta A$ Spectra Based on Derivative Analysis

### Regime I – Linewidth broadening and blue-shifts.

Figures A2.4a and A2.4b plot  $\Delta A$  after a pump-probe delay of 200 fs (solid red curve) and the averaged  $\Delta A$  between  $t_0$  and 500 fs (dashed red curve) together with the first derivative  $\frac{dA_0}{dE}$  (black, panel a) and the second derivative  $\frac{d^2A_0}{dE^2}$  (black, panel b). As evident in Figure A2.4a, the transient has a one-to-one correspondence with  $\frac{dA_0}{dE}$  between 1.6-1.9 eV. Notably, the ensuing fixed ratio of  $\Delta A$  to the first derivative  $\frac{dA_0}{dE}$  is negative and thereby reflects a blue-shift of the higher-lying energy states. Using equation A2.3, the blue-shift  $\delta E$ , for instance, evaluated at probe energy of 1.75 eV, equals  $\approx 0.2$  meV. As shown later on, this value agrees well with the spectral deconvolution of the transients.

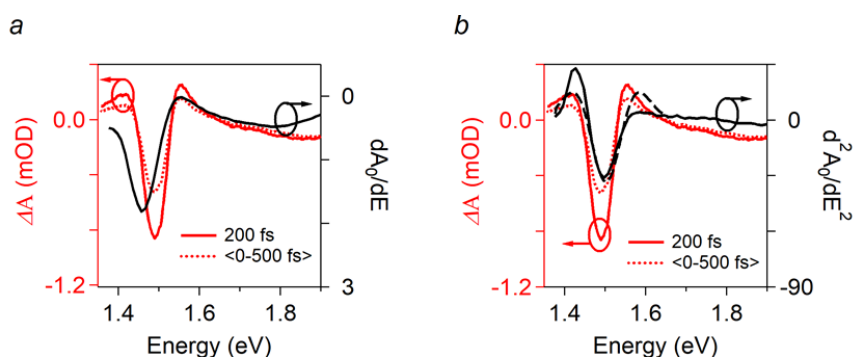


**Figure A2.4.** Overview of the derivative analysis in regime I. Comparison of (red) the transient absorbance at a delay of (red, solid curve) 200 fs and of (red, dashed curve) the averaged signal between  $t_0$  and 500 fs to (black, panel a) the first derivative  $\frac{dA_0}{dE}$  and to (black, panel b) the second derivative  $\frac{d^2A_0}{dE^2}$ . Take note that the right axis in panel a runs from positive to negative values.

Around the band edge, the transient coincides relatively well with minima and maxima in the second derivative  $\frac{d^2A_0}{dE^2}$  to the photon energy  $E$ , and the sign of this correspondence marks a broadening of the exciton. For clarity, we plot both the second derivative of  $A_0$  (solid black curve) and the second derivative of a fitted Gaussian absorption profile to  $A_0$  (black dashed curve). For an isolated Gaussian, the second derivative is symmetric; i.e., a linewidth change has an identical effect at lower and higher energy (black dashed curve). In the case of an  $A_0$  spectrum

consisting of an exciton superimposed on a step-like continuum, a broadening of the exciton line is more pronounced at lower energy (see the solid black curve). Irrespective of these considerations, the line symmetry of  $\Delta A$  is opposite from both predictions and is consistent with the presence of an additional blue-shift. As signified by its correspondence to  $-\frac{dA_0}{dE}$ , such a blue shift would decrease/increase the intensity at lower/higher energy. Although shifts also contribute to the transient, we can, nonetheless, make a rough estimate on the order of magnitude of the relative broadening  $\delta\sigma/\sigma_0$  using equation A2.4. In this respect, evaluating  $\Delta A$  at different energies, we retrieve values for  $\delta\sigma/\sigma_0$  of 0.3 – 0.7%.

### Regime II – Linewidth narrowing and red-shifts.

Figures A2.5a and A2.5b plot  $\Delta A$  after a pump-probe delay of 2 ps (solid red curve) and the averaged  $\Delta A$  between 1 ps and 1.5 ns (dashed red curve) together with the second derivative  $\frac{d^2 A_0}{dE^2}$  (black, panel a) and the first derivative  $\frac{dA_0}{dE}$  (black line, panel b). At longer time delays, the band edge feature has switched sign and is similar in shape to the mirror image of a second derivative, see Figure A2.5a. Importantly, such a correlation implies a counter-intuitive narrowing of the exciton band. Similarly, as pointed out above, the shape deviates from a purely narrowed line shape. Given that at those time delays,  $\Delta A$  is asymmetric with the lower energy feature being less intense, it also marks a superimposed red-shift. As marked by correspondence to  $\frac{dA_0}{dE}$ , such a red-shift would indeed increase  $\frac{dA_0}{dE}$  at shorter wavelengths, see Figure A2.5b.

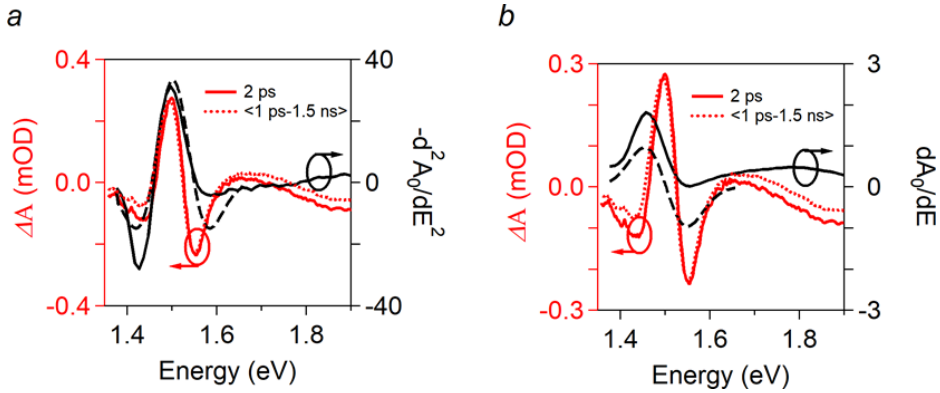


**Figure A2.5.** Overview of the derivative analysis in regime II. Comparison of (red) the transient absorbance at a delay of (red, solid curve) 2 ps and of (red, dashed curve) the averaged signal between 1 ps and 1.5 ns to (black, panel a) the second derivative  $-\frac{d^2 A_0}{dE^2}$  and to (black, panel b) the first derivative  $\frac{dA_0}{dE}$  to the energy.

### A2.3 Exciton polarizability

The exciton polarizability,  $\alpha$ , is defined as the ratio of the induced dipole moment to the applied electric field and can be theoretically calculated according to  $\alpha_{\text{theory}} = \frac{2e^2 a_B^2}{E_1 - E_0}$ .<sup>68</sup> In this expression, the summation over all higher exciton states is reduced to the first exciton state, and the transition dipole moment is taken equal to the two-dimensional exciton Bohr radius,  $a_B = 1$  nm.<sup>38</sup> Finally,  $E_1 - E_0$  is taken equal to exciton binding energy of ReS<sub>2</sub>, i.e., 117 meV.<sup>38</sup> This yields a value for  $\alpha_{\text{theory}}$  of  $0.27 \times 10^{-35}$  Cm<sup>2</sup>V<sup>-1</sup>. This number is lower than the experimental upper detection limit. The experimental upper detection limit is calculated through the relation,  $\alpha_{\text{exp}} = -e \text{Im}(\mu_{\text{EX}})/\omega$ . Here,  $\text{Im}(\mu_{\text{EX}})$  is the experimentally obtained imaginary quantum yield weighted mobility values and  $\omega$  is THz probe frequency. This results in  $\alpha_{\text{exp}} = 2.7 \times 10^{-35}$  Cm<sup>2</sup>V<sup>-1</sup>.

### A2.4 Charge Carrier Scattering and Analysis of the Frequency Dependence of the THz Conductivity by the Drude-Smith Model

The free charge carriers scattering length can be calculated using,  $L = \sqrt{\frac{4\mu_{\text{dc}} k_B T t_{\text{osc}}}{e}}$ . Here,  $\mu_{\text{dc}}$  is the dc mobility of free charges,  $t_{\text{osc}}$  is the time period of a single THz pulse (1 ps),  $k_B$  is the Boltzmann constant,  $T$  is the room temperature, and  $e$  is the electronic charge. From literature, the obtained value of  $\mu_{\text{dc}}$  for a 4.5

nm thick layer of ReS<sub>2</sub> is 30 cm<sup>2</sup>/Vs.<sup>43</sup> Thus, the scattering length of charges during a period of ( $t_{osc}$ ) the THz field is 17 nm, which is higher than the flakes thickness.

The backscattering of the charge carriers can be observed from the frequency dependent THz signal. To understand the charge transport mechanism we analyze the frequency-dependent THz conductivity signal obtained by averaging  $S(t)$  over a pump-probe delay time of 5-10 ps, shown in Figure A2.6. The charge mobility is fitted by the Drude-Smith equation (written below) to observe the signatures of localization and backscattering on the motion of free charge carriers.<sup>69</sup>

$$\mu(\omega) = \frac{e\tau}{m^*(1-i\omega\tau)} \left(1 + \frac{c}{1-i\omega\tau}\right) \quad \text{A2.13}$$

Here,  $e$  is the elementary charge,  $\tau$  is the scattering time,  $m^*$  is the effective mass, and  $c = \langle \cos(\theta) \rangle$  is a parameter that takes into account the elastic scattering with  $\theta$  the scattering angle. A fit of the Drude-Smith equation yields  $c = -0.87 \pm 0.02$ ,  $\tau = 7.5 \pm 1.0$  fs and  $m^* = 0.96 \pm 0.11 m_0$ , with  $m_0$  the free electron mass, resulting in comparable values to that of ReS<sub>2</sub> and other TMDCs reported in literature.<sup>70,71</sup> The obtained values from the fit are in line with The negative value of the scattering parameter  $c$  implies significant backscattering of the charges.

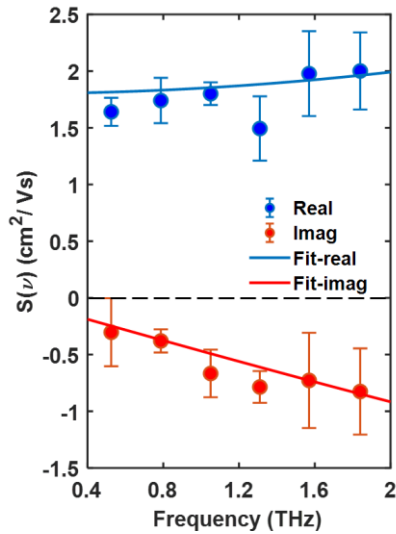


**Figure A2.6.** Frequency dependence of the THz conductivity signal (markers) and fits of the Drude-Smith model (solid lines).

## A2.5 Spectral Deconvolution of the Transient Absorbance

### Overview of the procedure

A first visual interpretation of the spectra and a comparison of the transients to derivatives of  $A_0$  to  $E$  marked a complex interplay between shifts and linewidth changes. To better quantify the parameters that govern the transient signal, we describe the ultrafast transient by a Gaussian band edge exciton  $G$  and a background absorbance  $C$  that accounts for the higher energy transitions. The Gaussian has (1) a variable central position accounting for spectral shifts, (2) a variable width accounting for line broadening and narrowing effects, and (3) a variable amplitude describing width and areal changes. In addition, the background absorbance spectrum can (4) shift toward lower or higher energy.

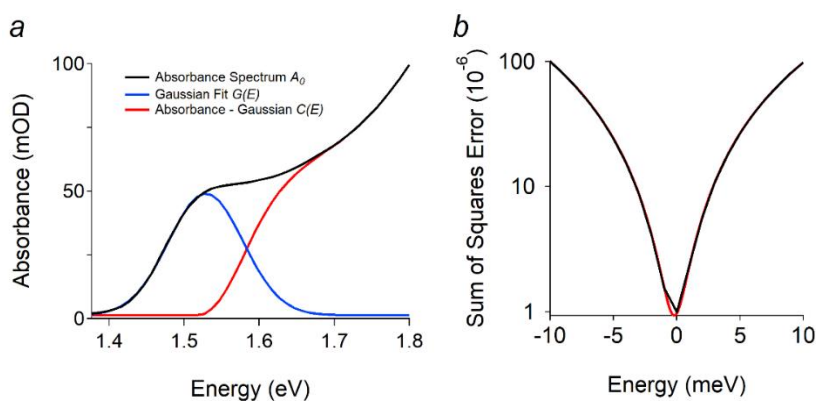


**Figure A2.7.** (a) Gaussian fit of the linear absorbance spectrum (black trace), partitioning the Gaussian fit function  $G(E)$  (blue trace) and the background absorbance  $C(E)$  (red trace). (b) An example of the error analysis.

In a first step, we describe the linear absorption by a fit to a Gaussian function with the amplitude  $h$ , the central position  $E_0$ , and the width  $w$ , as fit parameters:

$$G(E) = h \cdot \exp\left(-\frac{(E-E_0)^2}{w^2}\right) \quad \text{A2.14}$$

Such an approach yields a fitted spectrum as depicted in Figure A2.7. In this way, the difference between the fitted Gaussian (blue trace) and the linear absorbance spectrum (black trace) yields the background absorbance (red trace).

To fit the transients, we work in two stages. Since a background shift is not a straightforward fitting parameter in numerical software, we move the background in increments  $\delta E$ . Such an approach does not fit  $dA(E,t)$  directly, but rather the difference  $dA(E,t) - L_m(E, t, \delta E)$ , with  $L_m$  signifying the shifted background function at a background shift  $\delta E$ . Sweeping the background shift in increments  $\delta E$ , we scan for the best fit (the fit that provides a minimal error, see Figure A2.7b) and extract the other fitting parameters from that particular fit. The to-be fitted function now is

$$dA(E, t) = h_n(t) \cdot \exp\left(-\frac{(E-E_n(t))^2}{w_n(t)^2}\right) - h \cdot \exp\left(-\frac{(E-E_0)^2}{w^2}\right) \quad \text{A2.15}$$

where  $A$ ,  $E_0$ , and  $w$  are fixed to the linear value, and we fit the parameters  $A_n(t)$ ,  $E_n(t)$ , and  $w_n(t)$ . This set of fit parameters, together with the background shift  $\delta E$ , will fit our full model. This procedure is followed for each and every time slice, i.e., at each pump-probe delay.

### Understanding Spectral Shifts and Linewidth Changes by Spectral Deconvolution of the Transient $\Delta A$ Spectra

Using the procedure mentioned above, we extract, at each pump-probe time delay, the amplitude  $h$ , the spectral position  $E_{\text{exciton}}$ , and the width  $w$  of the Gaussian that describes the exciton band and a shift of the background absorbance  $\Delta E_{\text{bck}}$ . Next, we translate these into differential quantities:  $\Delta E_{\text{exciton}}$ ,  $\Delta h$ ,  $\Delta w$ , and  $\Delta E_{\text{bck}}$  defined relatively to the respective values before  $t_0$ , i.e., before photoexcitation.

The primary results of such a spectral deconvolution are summarized in Figure A2.8 and show the evolution of the parameters mentioned above as a function of the pump-probe delay. In conjunction with a visual interpretation and a derivative analysis, we observe a blue-shift of the higher-lying energy states (Figure A2.8a,  $\Delta E_{\text{bck}} > 0$ ), and the values agree with estimates based on equation A2.1. Around the band edge, the exciton line is blue-shifted (Figure A2.8b,  $\Delta E_{\text{exciton}} > 0$ ) and broadened (Figure A2.8c-d,  $\Delta w/w_0 > 0$  and  $\Delta h/h_0 < 0$ ). Both results align with a second-derivative-like line shape that is slightly asymmetric with a more intense PA band at the higher energy side (see Figure 2.2c, spectrum i).

Around a time delay of  $\approx 1 - 2$  ps, the exciton has decayed into its narrowed (Figure A2.8c-d,  $\Delta w/w_0 < 0$  and  $\Delta h/h_0 > 0$ ) and red-shifted (Figure A2.8b,  $\Delta E_{\text{exciton}} < 0$ ) mirror image. Concomitantly, a large fraction of the blue-shifted background (Figure A2.8a) has decayed. Over time, the exciton red-shift reaches a maximum of

around  $\approx 50$  ps, where the background shift starts to fluctuate around zero or becomes even slightly negative (i.e., a red-shift). On the other hand, the narrowed exciton line shows little to no decay.

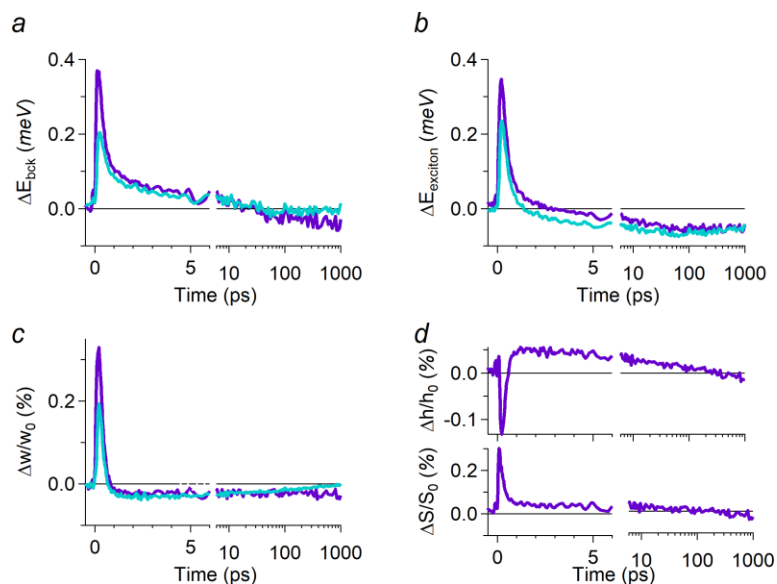


**Figure A2.8.** Evolution of the fit parameters that were obtained from a fit to a Gaussian  $G(h, E_{exciton}, w)$  and a background absorbance  $C(E)$  to the  $\Delta A$  in Figure 2.1b (cyan and blue curves represent fit with and without constrained area), including (a) the shift of the background absorbance  $\Delta E_{bck}$  and, (b) the energy shift of the exciton  $\Delta E_{exciton}$ , (c) and (d) the normalized change in the amplitude  $\Delta h/h_0$  of the Gaussian that describes the exciton band.

**Limitations** - While the agreement between the quantitative fit and the qualitative analyses presented above is remarkable, we also want to point out a shortcoming of our approach. We implemented the Gaussian amplitude and width as two different fit parameters to account for possible area changes. In this respect, the area is proportional to the product of the width and the amplitude. As shown in Figure A2.8d (bottom panel), the Gaussian area  $S$  seemingly increases after photoexcitation. Likely, this is due to the compensation of over-estimated blue-shifts. In this respect, we refitted the data-set while constraining the area of the Gaussian, and we plotted those fit parameters in Figure A2.8a-c in light blue. Most importantly, the trends we observe are similar. Yet, the initial blue-shifts and line broadening effects are slightly reduced in intensity. In contrast, the exciton red-shift gained intensity at long delays, and the narrowed line shows an expected decay over time.

## A2.6 Additional Information on the Deconvolution of Fluence Dependent TA Spectra

Using our spectral deconvolution procedure presented in section A2.5 and Figure 2.4 of the main text, we extracted, as a function of pump fluence of pump-probe delay, the shift  $\Delta E_{\text{exciton}}$  and linewidth change  $\Delta w$  of the exciton resonance together with a shift of the background absorbance  $\Delta E_{\text{bck}}$ . The results of such a spectral deconvolution are summarized in Figure A2.9 and evaluate the time-dependent evolution of the differential parameters mentioned above at different pump fluences, ranging from  $1.5 \times 10^{12} \text{ cm}^{-2}$  to  $11 \times 10^{12} \text{ cm}^{-2}$ . In line with the logic presented in the main text, we quantified each differential parameter in regime I (i.e., at early pump-probe delays,  $t \approx 0.25 \text{ ps}$ ) and in regime II (i.e., at long pump-probe delays; to account for signal noise, we averaged out between 100 ps and 1000 ps). Besides the linewidth change  $\Delta w$  II in regime II that saturates at high fluences, all differential parameters scale linearly with fluence, and point to a carrier-induced mechanism. In particular, and as pointed out in the main text, the linear dependence of the exciton red-shift on the fluence is characteristic for trap-assisted recombination rather than higher-order Auger recombination (see Figure 2.6).

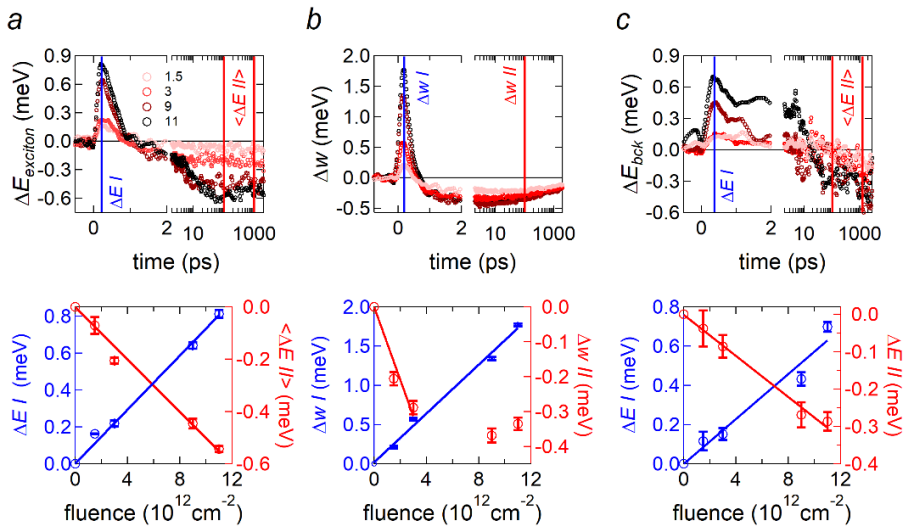


**Figure A2.9.** Evolution of the fit parameters (markers) obtained from a fit of a Gaussian  $G(E_{\text{exciton}}, w)$  with a constrained area and a background absorbance  $C(E_{\text{bck}})$  to TA maps measured at increasing absorbed fluences of  $1.5, 3, 9$  and  $11 \times 10^{12} \text{ cm}^{-2}$ , including (a) the energy shift of the exciton  $\Delta E_{\text{exciton}} = E_{\text{x}}(t) - E_{\text{x},0}$  and, (b) change in the exciton linewidth  $\Delta w = w - w_0$  and (c) shift of the background absorbance  $\Delta E_{\text{bck}} = E_{\text{bck}} - E_{\text{bck},0}$ .

## References

- (1) Wang, Q. H.; Kalantar-Zadeh, K.; Kis, A.; Coleman, J. N.; Strano, M. S. Electronics and Optoelectronics of Two-Dimensional Transition Metal Dichalcogenides. *Nat. Nanotechnol.* **2012**, *7*, 699–712.
- (2) Tongay, S.; Sahin, H.; Ko, C.; Luce, A.; Fan, W.; Liu, K.; Zhou, J.; Huang, Y.-S.; Ho, C.-H.; Yan, J.; Ogletree, D. F.; Aloni, S.; Ji, J.; Li, S.; Li, J.; Peeters, F. M.; Wu, J. Monolayer Behaviour in Bulk ReS<sub>2</sub> Due to Electronic and Vibrational Decoupling. *Nat. Commun.* **2014**, *5*, 3252.
- (3) Rahman, M.; Davey, K.; Qiao, S.-Z. Advent of 2D Rhenium Disulfide (ReS<sub>2</sub>): Fundamentals to Applications. *Adv. Funct. Mater.* **2017**, *27*, 1606129.
- (4) Dileep, K.; Sahu, R.; Sarkar, S.; Peter, S. C.; Datta, R. Layer Specific Optical Band Gap Measurement at Nanoscale in MoS<sub>2</sub> and ReS<sub>2</sub> van Der Waals Compounds by High Resolution Electron Energy Loss Spectroscopy. *J. Appl. Phys.* **2016**, *119*, 114309.
- (5) Liu, E.; Fu, Y.; Wang, Y.; Feng, Y.; Liu, H.; Wan, X.; Zhou, W.; Wang, B.; Shao, L.; Ho, C.-H.; Huang, Y.-S.; et al. Integrated Digital Inverters Based on Two-Dimensional Anisotropic ReS<sub>2</sub> Field-Effect Transistors. *Nat. Commun.* **2015**, *6*, 6991.
- (6) Echeverry, J. P.; Gerber, I. C. Theoretical Investigations of the Anisotropic Optical Properties of Distorted 1 T ReS<sub>2</sub> and ReSe<sub>2</sub> Monolayers, Bilayers, and in the Bulk Limit. *Phys. Rev. B* **2018**, *97*, 075123.
- (7) Xu, K.; Deng, H.-X.; Wang, Z.; Huang, Y.; Wang, F.; Li, S.-S.; Luo, J.-W.; He, J. Sulfur Vacancy Activated Field Effect Transistors Based on ReS<sub>2</sub> Nanosheets. *Nanoscale* **2015**, *7*, 15757–15762.
- (8) Liu, F.; Zheng, S.; He, X.; Chaturvedi, A.; He, J.; Chow, W. L.; Mion, T. R.; Wang, X.; Zhou, J.; Fu, Q.; Fan, H. J.; et al. Highly Sensitive Detection of Polarized Light Using Anisotropic 2D ReS<sub>2</sub>. *Adv. Funct. Mater.* **2016**, *26*, 1169–1177.
- (9) Liao, W.; Wei, W.; Tong, Y.; Chim, W. K.; Zhu, C. Low-Frequency Noise in Layered ReS<sub>2</sub> Field Effect Transistors on HfO<sub>2</sub> and Its Application for PH Sensing. *ACS Appl. Mater. Interfaces* **2018**, *10*, 7248–7255.
- (10) Shim, J.; Oh, A.; Kang, D.-H.; Oh, S.; Jang, S. K.; Jeon, J.; Jeon, M. H.; Kim, M.; Choi, C.; Lee, J.; Lee, S.; et al. High-Performance 2D Rhenium Disulfide (ReS<sub>2</sub>)

Transistors and Photodetectors by Oxygen Plasma Treatment. *Adv. Mater.* **2016**, *28*, 6985–6992.

(11) Hafeez, M.; Gan, L.; Li, H.; Ma, Y.; Zhai, T. Large-Area Bilayer ReS<sub>2</sub> Film/Multilayer ReS<sub>2</sub> Flakes Synthesized by Chemical Vapor Deposition for High Performance Photodetectors. *Adv. Funct. Mater.* **2016**, *26*, 4551–4560.

(12) Hafeez, M.; Gan, L.; Li, H.; Ma, Y.; Zhai, T. Chemical Vapor Deposition Synthesis of Ultrathin Hexagonal ReSe<sub>2</sub> Flakes for Anisotropic Raman Property and Optoelectronic Application. *Adv. Mater.* **2016**, *28*, 8296–8301.

(13) Wang, J.; Zhou, Y. J.; Xiang, D.; Ng, S. J.; Watanabe, K.; Taniguchi, T.; Eda, G. Polarized Light-Emitting Diodes Based on Anisotropic Excitons in Few-Layer ReS<sub>2</sub>. *Adv. Mater.* **2020**, *32*, 2001890.

(14) Yang, A.; Gao, J.; Li, B.; Tan, J.; Xiang, Y.; Gupta, T.; Li, L.; Suresh, S.; Idrobo, J. C.; Lu, T.-M.; Rong, M.; Koratkar, N. Humidity Sensing Using Vertically Oriented Arrays of ReS<sub>2</sub> Nanosheets Deposited on an Interdigitated Gold Electrode. *2D Mater.* **2016**, *3*, 045012.

(15) Chenet, D. A.; Aslan, O. B.; Huang, P. Y.; Fan, C.; van der Zande, A. M.; Heinz, T. F.; Hone, J. C. In-Plane Anisotropy in Mono- and Few-Layer ReS<sub>2</sub> Probed by Raman Spectroscopy and Scanning Transmission Electron Microscopy. *Nano Lett.* **2015**, *15*, 5667–5672.

(16) Wang, R.; Xu, X.; Yu, Y.; Ran, M.; Zhang, Q.; Li, A.; Zhuge, F.; Li, H.; Gan, L.; Zhai, T. The Mechanism of the Modulation of Electronic Anisotropy in Two-Dimensional ReS<sub>2</sub>. *Nanoscale* **2020**, *12*, 8915–8921.

(17) Qiao, X.-F.; Wu, J.-B.; Zhou, L.; Qiao, J.; Shi, W.; Chen, T.; Zhang, X.; Zhang, J.; Ji, W.; Tan, P.-H. Polytypism and Unexpected Strong Interlayer Coupling in Two-Dimensional Layered ReS<sub>2</sub>. *Nanoscale* **2016**, *8*, 8324–8332.

(18) Hart, L.; Dale, S.; Hoye, S.; Webb, J. L.; Wolverson, D. Rhenium Dichalcogenides: Layered Semiconductors with Two Vertical Orientations. *Nano Lett.* **2016**, *16*, 1381–1386.

(19) Cui, Q.; He, J.; Bellus, M. Z.; Mirzokarimov, M.; Hofmann, T.; Chiu, H.-Y.; Antonik, M.; He, D.; Wang, Y.; Zhao, H. Transient Absorption Measurements on Anisotropic Monolayer ReS<sub>2</sub>. *Small* **2015**, *11*, 5565–5571.

- (20) Fujita, T.; Ito, Y.; Tan, Y.; Yamaguchi, H.; Hojo, D.; Hirata, A.; Voiry, D.; Chhowalla, M.; Chen, M. Chemically Exfoliated ReS<sub>2</sub> Nanosheets. *Nanoscale* **2014**, *6*, 12458–12462.
- (21) Al-Dulaimi, N.; Lewis, E. A.; Lewis, D. J.; Howell, S. K.; Haigh, S. J.; O'Brien, P. Sequential Bottom-up and Top-down Processing for the Synthesis of Transition Metal Dichalcogenide Nanosheets: The Case of Rhenium Disulfide (ReS<sub>2</sub>). *Chem. Commun.* **2016**, *52*, 7878–7881.
- (22) Keyshar, K.; Gong, Y.; Ye, G.; Brunetto, G.; Zhou, W.; Cole, D. P.; Hackenberg, K.; He, Y.; Machado, L.; Kabbani, M.; Hart, A. H. C.; et al. Chemical Vapor Deposition of Monolayer Rhenium Disulfide (ReS<sub>2</sub>). *Adv. Mater.* **2015**, *27*, 4640–4648.
- (23) Martín-García, B.; Spirito, D.; Bellani, S.; Prato, M.; Romano, V.; Polovitsyn, A.; Brescia, R.; Oropesa-Nuñez, R.; Najafi, L.; Ansaldo, A.; D'Angelo, G.; et al. Extending the Colloidal Transition Metal Dichalcogenide Library to ReS<sub>2</sub> Nanosheets for Application in Gas Sensing and Electrocatalysis. *Small* **2019**, *15*, 1904670.
- (24) Schiettecatte, P.; Geiregat, P.; Hens, Z. Ultrafast Carrier Dynamics in Few-Layer Colloidal Molybdenum Disulfide Probed by Broadband Transient Absorption Spectroscopy. *J. Phys. Chem. C* **2019**, *123*, 10571–10577.
- (25) Zhou, P.; Tanghe, I.; Schiettecatte, P.; van Thourhout, D.; Hens, Z.; Geiregat, P. Ultrafast Carrier Dynamics in Colloidal WS<sub>2</sub> Nanosheets Obtained through a Hot Injection Synthesis. *J. Chem. Phys.* **2019**, *151*, 164701.
- (26) Coleman, J. N. Liquid Exfoliation of Defect-Free Graphene. *Acc. Chem. Res.* **2013**, *46*, 14–22.
- (27) Schiettecatte, P.; Rousaki, A.; Vandenabeele, P.; Geiregat, P.; Hens, Z. Liquid-Phase Exfoliation of Rhenium Disulfide by Solubility Parameter Matching. *Langmuir* **2020**, *36*, 15493–15500.
- (28) Maiti, S.; Poonia, D.; Schiettecatte, P.; Hens, Z.; Geiregat, P.; Kinge, S.; Siebbeles, L. D. A. Generating Triplets in Organic Semiconductor Tetracene upon Photoexcitation of Transition Metal Dichalcogenide ReS<sub>2</sub>. *J. Phys. Chem. Lett.* **2021**, *12*, 5256–5260.

- (29) Jawaid, A.; Nepal, D.; Park, K.; Jespersen, M.; Qualley, A.; Mirau, P.; Drummy, L. F.; Vaia, R. A. Mechanism for Liquid Phase Exfoliation of MoS<sub>2</sub>. *Chem. Mater.* **2016**, *28*, 337–348.
- (30) Backes, C.; Higgins, T. M.; Kelly, A.; Boland, C.; Harvey, A.; Hanlon, D.; Coleman, J. N. Guidelines for Exfoliation, Characterization and Processing of Layered Materials Produced by Liquid Exfoliation. *Chem. Mater.* **2017**, *29*, 243–255.
- (31) Spoor, F. C. M.; Kunneman, L. T.; Evers, W. H.; Renaud, N.; Grozema, F. C.; Houtepen, A. J.; Siebbeles, L. D. A. Hole Cooling Is Much Faster than Electron Cooling in PbSe Quantum Dots. *ACS Nano* **2016**, *10*, 695–703.
- (32) Spoor, F. C. M.; Tomić, S.; Houtepen, A. J.; Siebbeles, L. D. A. Broadband Cooling Spectra of Hot Electrons and Holes in PbSe Quantum Dots. *ACS Nano* **2017**, *11*, 6286–6294.
- (33) Lauth, J.; Kulkarni, A.; Spoor, F. C. M.; Renaud, N.; Grozema, F. C.; Houtepen, A. J.; Schins, J. M.; Kinge, S.; Siebbeles, L. D. A. Photogeneration and Mobility of Charge Carriers in Atomically Thin Colloidal InSe Nanosheets Probed by Ultrafast Terahertz Spectroscopy. *J. Phys. Chem. Lett.* **2016**, *7*, 4191–4196.
- (34) Grimaldi, G.; Geuchies, J. J.; van der Stam, W.; du Fossé, I.; Brynjarsson, B.; Kirkwood, N.; Kinge, S.; Siebbeles, L. D. A.; Houtepen, A. J. Spectroscopic Evidence for the Contribution of Holes to the Bleach of Cd-Chalcogenide Quantum Dots. *Nano Lett.* **2019**, *19*, 3002–3010.
- (35) Kunneman, L. T.; Zanella, M.; Manna, L.; Siebbeles, L. D. A.; Schins, J. M. Mobility and Spatial Distribution of Photoexcited Electrons in CdSe/CdS Nanorods. *J. Phys. Chem. C* **2013**, *117*, 3146–3151.
- (36) Evers, W. H.; Schins, J. M.; Aerts, M.; Kulkarni, A.; Capiod, P.; Berthe, M.; Grandidier, B.; Delerue, C.; van der Zant, H. S. J.; van Overbeek, C.; Peters, J. L.; et al. High Charge Mobility in Two-Dimensional Percolative Networks of PbSe Quantum Dots Connected by Atomic Bonds. *Nat. Commun.* **2015**, *6*, 8195.
- (37) Lauth, J.; Failla, M.; Klein, E.; Klinke, C.; Kinge, S.; Siebbeles, L. D. A. Photoexcitation of PbS Nanosheets Leads to Highly Mobile Charge Carriers and Stable Excitons. *Nanoscale* **2019**, *11*, 21569–21576.

- (38) Jadczyk, J.; Kutrowska-Girzycka, J.; Smoleński, T.; Kossacki, P.; Huang, Y. S.; Bryja, L. Exciton Binding Energy and Hydrogenic Rydberg Series in Layered ReS<sub>2</sub>. *Sci. Rep.* **2019**, *9*, 1578.
- (39) Ulbricht, R.; Hendry, E.; Shan, J.; Heinz, T. F.; Bonn, M. Carrier Dynamics in Semiconductors Studied with Time-Resolved Terahertz Spectroscopy. *Rev. Mod. Phys.* **2011**, *83*, 543–586.
- (40) Lloyd-Hughes, J.; Jeon, T.-I. A Review of the Terahertz Conductivity of Bulk and Nano-Materials. *J. Infrared Millim. Terahertz Waves* **2012**, *33*, 871–925.
- (41) Yu, Z. G.; Cai, Y.; Zhang, Y.-W. Robust Direct Bandgap Characteristics of One- and Two-Dimensional ReS<sub>2</sub>. *Sci. Rep.* **2015**, *5*, 13783.
- (42) Tiong, K. K.; Ho, C. H.; Huang, Y. S. The Electrical Transport Properties of ReS<sub>2</sub> and ReSe<sub>2</sub> Layered Crystals. *Solid State Commun.* **1999**, *111*, 635–640.
- (43) Liu, E.; Long, M.; Zeng, J.; Luo, W.; Wang, Y.; Pan, Y.; Zhou, W.; Wang, B.; Hu, W.; Ni, Z.; You, Y.; et al. High Responsivity Phototransistors Based on Few-Layer ReS<sub>2</sub> for Weak Signal Detection. *Adv. Funct. Mater.* **2016**, *26*, 1938–1944.
- (44) Cunningham, P. D.; McCreary, K. M.; Hanbicki, A. T.; Currie, M.; Jonker, B. T.; Hayden, L. M. Charge Trapping and Exciton Dynamics in Large-Area CVD Grown MoS<sub>2</sub>. *J. Phys. Chem. C* **2016**, *120*, 5819–5826.
- (45) Hindmarsh, W. R.; Petford, A. D.; Smith, G.; Kuhn, H. G. Interpretation of Collision Broadening and Shift in Atomic Spectra. *Proc. R. Soc. Lond. Ser. Math. Phys. Sci.* **1967**, *297*, 296–304.
- (46) Leite, R. C. C.; Shah, J.; Gordon, J. P. Effect of Electron-Exciton Collisions on the Free-Exciton Linewidth in Epitaxial GaAs. *Phys. Rev. Lett.* **1969**, *23*, 1332–1335.
- (47) Schultheis, L.; Kuhl, J.; Honold, A.; Tu, C. W. Ultrafast Phase Relaxation of Excitons via Exciton-Exciton and Exciton-Electron Collisions. *Phys. Rev. Lett.* **1986**, *57*, 1635–1638.
- (48) Sim, S.; Park, J.; Song, J.-G.; In, C.; Lee, Y.-S.; Kim, H.; Choi, H. Exciton Dynamics in Atomically Thin MoS<sub>2</sub>: Interexcitonic Interaction and Broadening Kinetics. *Phys. Rev. B* **2013**, *88*, 075434.

- (49) Cunningham, P. D.; Hanbicki, A. T.; McCreary, K. M.; Jonker, B. T. Photoinduced Bandgap Renormalization and Exciton Binding Energy Reduction in WS<sub>2</sub>. *ACS Nano* **2017**, *11*, 12601–12608.
- (50) Wang, G.; Chernikov, A.; Glazov, M. M.; Heinz, T. F.; Marie, X.; Amand, T.; Urbaszek, B. Colloquium: Excitons in Atomically Thin Transition Metal Dichalcogenides. *Rev. Mod. Phys.* **2018**, *90*, 021001.
- (51) Schmitt-Rink, S.; Ell, C.; Haug, H. Many-Body Effects in the Absorption, Gain, and Luminescence Spectra of Semiconductor Quantum-Well Structures. *Phys. Rev. B* **1986**, *33*, 1183–1189.
- (52) Schmitt-Rink, S.; Chemla, D. S.; Miller, D. A. B. Linear and Nonlinear Optical Properties of Semiconductor Quantum Wells. *Adv. Phys.* **1989**, *38*, 89–188.
- (53) Wake, D. R.; Yoon, H. W.; Wolfe, J. P.; Morkoç, H. Response of Excitonic Absorption Spectra to Photoexcited Carriers in GaAs Quantum Wells. *Phys. Rev. B* **1992**, *46*, 13452–13460.
- (54) Hulin, D.; Mysyrowicz, A.; Antonetti, A.; Migus, A.; Masselink, W. T.; Morkoç, H.; Gibbs, H. M.; Peyghambarian, N. Well-Size Dependence of Exciton Blue Shift in GaAs Multiple-Quantum-Well Structures. *Phys. Rev. B* **1986**, *33*, 4389–4391.
- (55) Ruppert, C.; Chernikov, A.; Hill, H. M.; Rigosi, A. F.; Heinz, T. F. The Role of Electronic and Phononic Excitation in the Optical Response of Monolayer WS<sub>2</sub> after Ultrafast Excitation. *Nano Lett.* **2017**, *17*, 644–651.
- (56) Wu, X.; Trinh, M. T.; Zhu, X.-Y. Excitonic Many-Body Interactions in Two-Dimensional Lead Iodide Perovskite Quantum Wells. *J. Phys. Chem. C* **2015**, *119*, 14714–14721.
- (57) Steinhoff, A.; Rösner, M.; Jahnke, F.; Wehling, T. O.; Gies, C. Influence of Excited Carriers on the Optical and Electronic Properties of MoS<sub>2</sub>. *Nano Lett.* **2014**, *14*, 3743–3748.
- (58) Moody, G.; Kavir Dass, C.; Hao, K.; Chen, C.-H.; Li, L.-J.; Singh, A.; Tran, K.; Clark, G.; Xu, X.; Berghäuser, G.; Malic, E.; et al. Intrinsic Homogeneous Linewidth and Broadening Mechanisms of Excitons in Monolayer Transition Metal Dichalcogenides. *Nat. Commun.* **2015**, *6*, 8315.

- (59) Stoneham, A. M. Shapes of Inhomogeneously Broadened Resonance Lines in Solids. *Rev. Mod. Phys.* **1969**, *41*, 82–108.
- (60) Wood, T. H.; Burrus, C. A.; Miller, D. a. B.; Chemla, D. S.; Damen, T. C.; Gossard, A. C.; Wiegmann, W. High-speed Optical Modulation with GaAs/GaAlAs Quantum Wells in a P-i-n Diode Structure. *Appl. Phys. Lett.* **1984**, *44*, 16–18.
- (61) Miller, D. A. B.; Chemla, D. S.; Damen, T. C.; Gossard, A. C.; Wiegmann, W.; Wood, T. H.; Burrus, C. A. Electric Field Dependence of Optical Absorption near the Band Gap of Quantum-Well Structures. *Phys. Rev. B* **1985**, *32*, 1043–1060.
- (62) Weiner, J. S.; Miller, D. a. B.; Chemla, D. S.; Damen, T. C.; Burrus, C. A.; Wood, T. H.; Gossard, A. C.; Wiegmann, W. Strong Polarization-sensitive Electroabsorption in GaAs/AlGaAs Quantum Well Waveguides. *Appl. Phys. Lett.* **1985**, *47*, 1148–1150.
- (63) Kuo, Y.-H.; Lee, Y. K.; Ge, Y.; Ren, S.; Roth, J. E.; Kamins, T. I.; Miller, D. A. B.; Harris, J. S. Strong Quantum-Confined Stark Effect in Germanium Quantum-Well Structures on Silicon. *Nature* **2005**, *437*, 1334–1336.
- (64) Zhou, Y.; Maity, N.; Rai, A.; Juneja, R.; Meng, X.; Roy, A.; Zhang, Y.; Xu, X.; Lin, J.-F.; Banerjee, S. K.; Singh, A. K.; et al. Stacking-Order-Driven Optical Properties and Carrier Dynamics in ReS<sub>2</sub>. *Adv. Mater.* **2020**, *32*, 1908311.
- (65) Fei, Z.; Zhao, W.; Palomaki, T. A.; Sun, B.; Miller, M. K.; Zhao, Z.; Yan, J.; Xu, X.; Cobden, D. H. Ferroelectric Switching of a Two-Dimensional Metal. *Nature* **2018**, *560*, 336–339.
- (66) Raja, A.; Waldecker, L.; Zipfel, J.; Cho, Y.; Brem, S.; Ziegler, J. D.; Kulig, M.; Taniguchi, T.; Watanabe, K.; Malic, E.; Heinz, T. F.; Berkelbach, T. C.; Chernikov, A. Dielectric Disorder in Two-Dimensional Materials. *Nat. Nanotechnol.* **2019**, *14*, 832–837.
- (67) Geiregat, P.; Houtepen, A.; Justo, Y.; Grozema, F. C.; Van Thourhout, D.; Hens, Z. Coulomb Shifts upon Exciton Addition to Photoexcited PbS Colloidal Quantum Dots. *J. Phys. Chem. C* **2014**, *118*, 22284–22290.
- (68) Atkins, P. W.; Friedman, R. S. *Molecular Quantum Mechanics*; OUP Oxford, 2011.

(69) Smith, N. Classical Generalization of the Drude Formula for the Optical Conductivity. *Phys. Rev. B* 2001, 64, 155106.

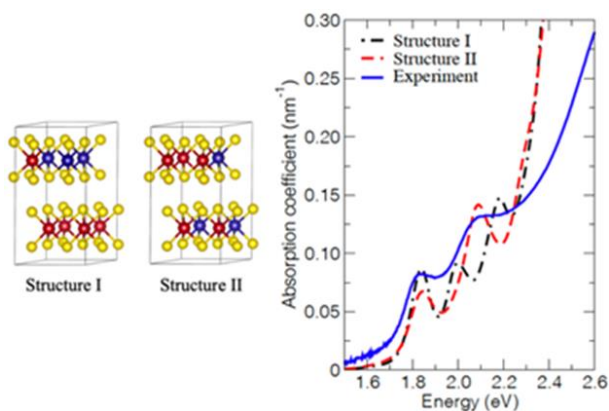
(70) Ovchinnikov, D.; Gargiulo, F.; Allain, A.; Pasquier, D. J.; Dumcenco, D.; Ho, C.-H.; Yazyev, O. V.; Kis, A. Disorder Engineering and Conductivity Dome in ReS<sub>2</sub> with Electrolyte Gating. *Nat. Commun.* 2016, 7, 12391.

(71) Nie, Z.; Long, R.; Sun, L.; Huang, C.-C.; Zhang, J.; Xiong, Q.; Hewak, D. W.; Shen, Z.; Prezhd, O. V.; Loh, Z.-H. Ultrafast Carrier Thermalization and Cooling Dynamics in Few- Layer MoS<sub>2</sub>. *ACS Nano* 2014, 8, 10931–10940.



## Chapter 3

### Effects of Structure and Temperature on the Nature of Excitons in the $\text{Mo}_{0.6}\text{W}_{0.4}\text{S}_2$ Alloy



Based on:

#### Effects of Structure and Temperature on the Nature of Excitons in the $\text{Mo}_{0.6}\text{W}_{0.4}\text{S}_2$ Alloy.

Deepika Poonia, Nisha Singh, Jeff J.P.M. Schulpen, Marco van der Laan, Sourav Maiti, Michele Failla, Sachin Kinge, Ageeth A. Bol, Peter Schall, and Laurens D.A. Siebbeles

J. Phys. Chem. C 2022, 126, 1931–1938.

### 3.1 Introduction

Layered van der Waals materials, in particular transition metal dichalcogenides (TMDCs), have gained considerable interest due to prospects for applications in e.g., photodetectors,<sup>1,2</sup> sensors,<sup>3,4</sup> and solar cells.<sup>5-7</sup> These materials consist of layers in which transition metal atoms are covalently bound to chalcogen (S, Se, Te) atoms. The layers are stacked on top of each other and held together by van der Waals forces.<sup>8,9</sup> TMDCs with chemical composition  $\text{MX}_2$  (M= Mo, W, etc. and X = S, Se) have been studied extensively owing to their direct bandgap in monolayers,<sup>10</sup> valley selective optical coupling,<sup>11</sup> and large exciton binding energies.<sup>12</sup> Alloying has been used to vary the relative content ( $y$ ) of the transition metal or chalcogen atoms and obtain layers of  $\text{M}_y\text{M}'_{1-y}\text{X}_2$  or  $\text{MX}_{2y}\text{X}'_{2(1-y)}$ .<sup>13,14</sup> For monolayers of  $\text{Mo}_y\text{W}_{1-y}\text{S}_2$  alloys it was found that the Mo and W atoms are spatially distributed in a random way.<sup>15</sup> Increasing the W content in samples of one or a few  $\text{Mo}_y\text{W}_{1-y}\text{S}_2$  layers caused a blue shift of the exciton peak in optical absorption and reflection spectra,<sup>16,17</sup> in agreement with time-dependent density functional theory (TDDFT) calculations.<sup>18</sup> According to DFT calculations the valence band of monolayer  $\text{Mo}_{0.5}\text{W}_{0.5}\text{S}_2$  consists of atomic d-orbitals on both Mo and W atoms, while the conduction band consists predominantly of d-orbitals on Mo atoms.<sup>19</sup>

For optoelectronic applications, understanding of electron-phonon and exciton-phonon interactions is important. The strength of these interactions governs charge transport,<sup>20</sup> bandgap renormalization,<sup>21</sup> optical heating of the lattice<sup>22</sup>, and intervalley scattering of excitons.<sup>23-25</sup> In this regard, effects of temperature on optical absorption and photoluminescence spectra can provide information about the coupling strength between excitons and phonons in TMDCs.<sup>23-26</sup>

More than two decades ago, Ho *et al.*<sup>27</sup> studied the effects of temperature on excitons in single crystals of  $\text{Mo}_y\text{W}_{1-y}\text{S}_2$  alloys by piezoreflectance measurements, which preferentially probe excitons near the sample surface. We extend these studies on atomic layer deposited (ALD)<sup>28</sup> bulk part of the  $\text{Mo}_{0.6}\text{W}_{0.4}\text{S}_2$  alloy to investigate the effects of temperature on peak energies and linewidths of excitons. The almost equal content of Mo and W atoms in the alloy is of interest since it offers the possibility to realize intimate mixing of the transition metal atoms, rather than having separate domains consisting of one atom type only. To elucidate the effects of the relative arrangement of Mo and W atoms in the alloy, we compared the measured spectra with results from *ab-initio* TDDFT calculations. For this purpose,

we constructed supercells having different positions of the metal atoms in the crystal structure of the alloy. The TDDFT calculations reproduced the experimental spectrum of the alloy for structures in which all layers contain both Mo and W atoms. In contrast, calculations on a structure containing W atoms in individual layers that are separated by layers containing only Mo atoms do not reproduce the experimental spectrum. From the latter, we infer that the ALD growth yields structures with a predominantly homogeneous spatial distribution of Mo and W atoms.

## 3.2 Materials and methods

**3.2.1 Temperature-dependent optical transmission measurements.** We used our previously reported ALD procedure to grow thin films of  $\text{MoS}_2$ ,  $\text{WS}_2$  and the  $\text{Mo}_{0.6}\text{W}_{0.4}\text{S}_2$  alloy, with thickness of 6.3 nm, 4.1 nm and 5.2 nm, respectively, on quartz substrates.<sup>28</sup> The uncertainty in the fraction of Mo and W is  $\pm 0.01$ .<sup>28</sup> The alloy was grown using an ALD supercycle length of 2 cycles (consisting of 1  $\text{MoS}_2$  cycle and 1  $\text{WS}_2$  cycle), to realize fine mixing of the Mo and W atoms. The composition was determined by XPS.<sup>28</sup> The separation between adjacent layers in these materials is  $\sim 0.6$  nm, so the film thicknesses correspond to 10-11, 6-7 and 8-9 layers, respectively.

The optical transmission of the samples was measured using a home-built setup containing a DH-2000 halogen light source and an Ocean-optics Maya 2000 spectrometer. To vary the temperature, the samples were placed under vacuum in a He-closed cycle cryostat. These measurements yield the fraction of light transmitted,  $T$ , through the sample as a function of photon energy and temperature.

For comparison of the optical properties of the samples with the optical absorption coefficient from TDDFT calculations (see Section 3.3), we determined the optical density,  $OD$ , using a Perkin Elmer Lambda 1050 spectrometer with an integrating sphere. This could be done only at room temperature, since the spectrometer is not equipped with a cryostat. Placing the sample in front of the light entrance of the integrating sphere yields  $T$ , and placing it in the center provides  $T+R$ , where  $R$  is the fraction of light reflected. Results of  $1-T$ ,  $R$ , and the fraction of light absorbed  $A = 1 - R - T$  are shown in Figure A3.1 for the pure compounds and the alloy. The optical density is obtained using the relation  $OD = -\log\left(\frac{T}{1-R}\right)$ . The

optical absorption coefficient,  $\alpha$ , of a film with thickness  $L$  is related to the  $OD$  according to  $e^{-\alpha L} = 10^{-OD}$ , giving  $\alpha = OD \ln(10)/L$ .

**3.2.2 TDDFT calculations of optical absorption coefficients.** Electronic structure calculations were performed using the all-electron full-potential linearized augmented plane wave (LAPW) code Elk<sup>29</sup> with PBE (GGA) functionals.<sup>30</sup> For all materials a hexagonal crystal structure (2H) was used, with the experimental lattice constants of 3.169 Å and 12.324 Å for MoS<sub>2</sub><sup>31</sup> and 3.153 Å and 12.323 Å for WS<sub>2</sub>.<sup>32</sup> A 2×2×1 supercell is constructed to study the Mo<sub>0.625</sub>W<sub>0.375</sub>S<sub>2</sub> alloy with the lattice parameters 6.338 Å and 12.324 Å obtained by doubling the MoS<sub>2</sub> unit cell. This is the smallest supercell describing the experimentally studied alloy with a composition very close to the experimental uncertainty, see Section 3.2.1. For calculations on a Mo<sub>0.6</sub>W<sub>0.4</sub>S<sub>2</sub> alloy we would need a 5×5×5 supercell with 75 Mo, 50 W and 250 S atoms. The large computational time and memory needed for the latter is impractical. Therefore we consider the Mo<sub>0.625</sub>W<sub>0.375</sub>S<sub>2</sub> alloy in the calculations. Calculation of the dielectric response functions from TDDFT requires a dense k-point grid to sample the Brillouin zone (BZ); hence a k-point grid of 16×16×8 for the primitive unit cell and a 8×8×8 k-point grid for the supercell are used. The set of LAPW basis functions is defined by specifying a cut off parameter  $|\mathbf{k} + \mathbf{G}|_{max}$  whose value is set to 7.0 Bohr<sup>-1</sup>. Additionally, the response is calculated using G vectors of length 1.5 Bohr<sup>-1</sup>. The number of conduction bands included in the calculations is 24 for both MoS<sub>2</sub>, WS<sub>2</sub>, and 96 for the alloy.

In TDDFT, a Dyson-like equation is solved to obtain the dielectric response function<sup>33</sup> whose real and imaginary parts can be used to obtain the optical absorption coefficient  $\alpha$ .<sup>34</sup> The method to obtain optical response functions is a two-step procedure. Firstly, a ground-state calculation is done to obtain the converged density and potentials. Next, the dielectric functions of MoS<sub>2</sub>, WS<sub>2</sub>, and the Mo<sub>0.625</sub>W<sub>0.375</sub>S<sub>2</sub> alloy are calculated as a function of photon energy using the bootstrap kernel,<sup>35</sup> as it is capable of capturing excitons in the TDDFT calculations. The dielectric functions thus obtained were broadened by 80 meV for MoS<sub>2</sub>, WS<sub>2</sub> and 54 meV for the alloy to obtain the best matches with the experimental optical absorption coefficient spectra ( $\alpha$ ). Note that the broadening thus introduced in the calculated spectra does not explain the exciton linewidths in the experimental spectra.

### 3.3 Results and discussion

**3.3.1 Optical transmission spectra.** Figure 3.1a shows optical transmission spectra of  $\text{MoS}_2$ ,  $\text{WS}_2$ , and the  $\text{Mo}_{0.6}\text{W}_{0.4}\text{S}_2$  alloy at room temperature (293 K). These spectra show the magnitude of  $1-T$ , which is the fraction of incident light that is not transmitted through the sample. The spectra of  $\text{MoS}_2$  and  $\text{WS}_2$  agree with previous results.<sup>8,36</sup> Two distinct peaks (marked by A and B) can be seen in all three materials. The peaks are due to photoexcitation from the ground state to A and B exciton states. The energies of these peaks are determined by spin-orbit coupling and interlayer interactions at the K and K' point of the Brillouin zone (BZ).<sup>37–39</sup> Towards the higher energy side, a broad absorption feature is observed (often addressed as C exciton), which originates from multiple transitions from the highest valence band to the lowest conduction bands near the  $\Gamma$  point of the BZ.<sup>40</sup> On lowering the temperature to 25 K (Figure 3.1b), the exciton peaks of all three materials become narrower and shift to higher energy.

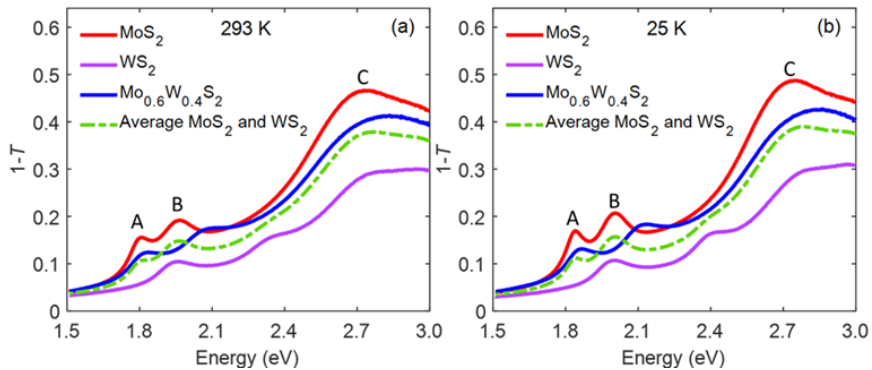


**Figure 3.1.** (a) Room-temperature (293 K) and (b) low temperature (25 K) optical transmission spectra of  $\text{MoS}_2$  (red),  $\text{WS}_2$  (magenta) and the  $\text{Mo}_{0.6}\text{W}_{0.4}\text{S}_2$  alloy (blue). The dashed green curves are the average of the  $\text{MoS}_2$  and  $\text{WS}_2$  spectra.

To gain qualitative insight into the effect of alloying, we also show the average of the spectra of pure  $\text{MoS}_2$  and  $\text{WS}_2$  as green dashed curves in Figure 3.1a quantitative comparison of the measured  $OD$  and results from TDDFT is discussed in Section 3.3). The average spectra at 293 K and 25 K both differ from the spectra of the alloy. Most strikingly, the B exciton peak of the alloy appears at significantly higher energy than in the average spectra. These differences indicate that formation of excitons in domains consisting of either predominantly  $\text{MoS}_2$  or  $\text{WS}_2$  is unlikely. As a consequence, the probability that photoexcitation leads to formation of a

charge transfer exciton at a boundary between these material domains is small. Indeed, the peak of the A exciton in the alloy spectrum appears at higher energy than that in the spectrum of  $\text{MoS}_2$ , while that of a charge transfer exciton would be at lower energy.

Inspection of the transmission spectra of the alloy points towards closer similarities to  $\text{MoS}_2$  than to  $\text{WS}_2$ . Despite intimate mixing and nearly equal Mo and W content in the alloy,<sup>28</sup> the energies of the A and B exciton in the alloy are closer to those of pure  $\text{MoS}_2$ , as also found for samples of one or a few  $\text{Mo}_{0.5}\text{W}_{0.5}\text{S}_2$  layers before.<sup>16,17</sup> This suggests that the wave functions of excitons in the  $\text{Mo}_{0.6}\text{W}_{0.4}\text{S}_2$  alloy have a larger amplitude on Mo atoms than on W atoms. The latter agrees with charge density distributions for the highest valence and lowest conduction band states obtained from DFT calculations.<sup>14,19</sup> Interestingly, according to our TDDFT calculations the mutual arrangement of Mo and W atoms within the material has a large impact on the shape of the optical absorption spectrum, see Section 3.3.3. To gain insight into the nature of exciton-phonon coupling, we first proceed with a discussion of the measured effects of temperature on exciton peak positions and linewidths in Section 3.3.2.

### 3.3.2 Temperature dependence of A and B exciton peak energies and linewidths.

To get further insight into the relative contributions of Mo and W atoms to the character of excitons, we compare the effects of exciton-phonon coupling in the  $\text{Mo}_{0.6}\text{W}_{0.4}\text{S}_2$  alloy with those in  $\text{MoS}_2$  and  $\text{WS}_2$ . We studied electron-phonon coupling by analysis of the temperature dependence of exciton peak energies and linewidths in the transmission spectra, as outlined in appendix A3.2. The peaks due to A and B excitons could each be described by a Lorentzian function with linewidth  $\Gamma_X$ , (where  $X = A, B$ ), which is defined as the full-width at half-maximum (FWHM), see Equation A3.1. The contribution of optical reflection, below band gap absorption due to defects,<sup>41</sup> and the broad C absorption feature at higher energy in the optical transmission spectra in Figure 3.1 could be described by two Gaussian functions. The total fit function thus consists of two Lorentzian and two Gaussian functions, see Equation A3.1. Figure A3.2 shows that the fits reproduce the experimental transmission spectra very well.

Figures 3.2 and 3.3 show the temperature dependence of the A and B exciton peak energies and linewidths, as obtained from fits of Equation A3.1 to the experimental transmission spectra. At all temperatures, the peak energies and

linewidths of the  $\text{Mo}_{0.6}\text{W}_{0.4}\text{S}_2$  alloy are closer to those of  $\text{MoS}_2$  than  $\text{WS}_2$ . This further supports the idea that excitons have more Mo than W character, as we already inferred above from Figure 3.1.

The decrease of the exciton peak energies with increasing temperature is due to the availability of more phonons at higher temperatures that can be absorbed upon photoexcitation from the electronic ground state to an exciton state, as well as electron-phonon coupling due to interaction between the motion of electrons and atomic nuclei (change of bond lengths and breakdown of the Born-Oppenheimer approximation).<sup>42–44</sup> Following previous studies<sup>26,44–46</sup> we describe the temperature dependence of the exciton peak energies by the semi-empirical O’Donnell equation<sup>47</sup>

$$E_X = E_{0,X} - S_X \langle \hbar\omega_X \rangle \left[ \coth \left( \frac{\langle \hbar\omega_X \rangle}{2k_B T} \right) - 1 \right] \quad 3.1$$

where  $X = A, B$  denotes the exciton type and  $k_B$  and  $\hbar$  are the Boltzmann and the reduced Planck constant, respectively. In Equation 3.1,  $E_{0,X}$  is the exciton peak energy at zero temperature,  $S_X$  is a dimensionless constant that increases with the exciton-phonon coupling strength and  $\langle \hbar\omega_X \rangle$  is the coupling-weighted average of the phonon energies that interact with the exciton.<sup>48</sup>

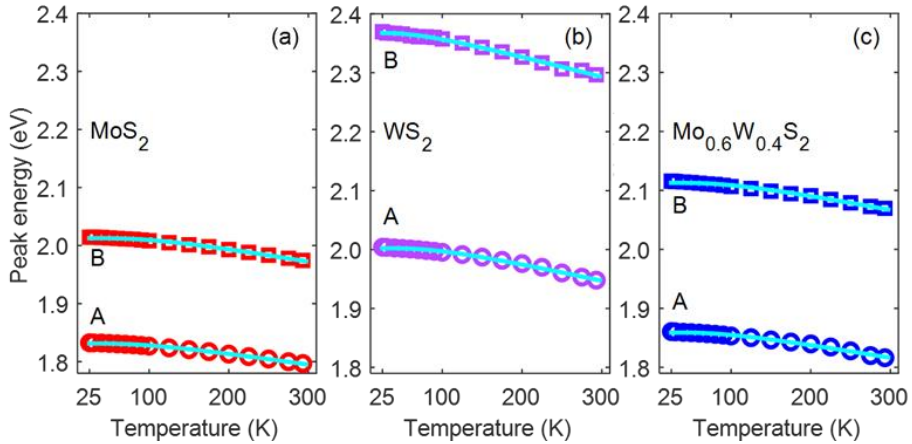


**Figure 3.2.** Temperature dependence of the A and B exciton peak energies for (a)  $\text{MoS}_2$ , (b)  $\text{WS}_2$ , and (c) the  $\text{Mo}_{0.6}\text{W}_{0.4}\text{S}_2$  alloy, obtained from the measured transmission spectra (markers). The solid cyan curves are fits of Equation 3.1 to the experimental peak energies.

Fits of Equation 3.1 to the A and B exciton peak energies with  $E_{0,X}$ ,  $S_X$  and  $\langle \hbar\omega_X \rangle$  as adjustable parameters are shown as solid cyan curves in Figure 3.2. Equation 3.1

reproduces the temperature dependence of the exciton peak energies very well and the values of the fit parameters are presented in Table 3.1. The exciton peak energies  $E_{0,A}$  and  $E_{0,B}$  for the alloy are closer to those for MoS<sub>2</sub> than for WS<sub>2</sub>. In addition, the fitted values near 1.5 of  $S_A$  and  $S_B$  for the alloy are similar to those of MoS<sub>2</sub>, while they are about 25% smaller than the values near 2.0 obtained for WS<sub>2</sub>. These findings corroborate our notice in Section 3.3.1. that exciton wave functions in the alloy have a larger amplitude on Mo atoms than on W atoms, so that the former has a predominant effect on exciton-phonon coupling. To within the experimental uncertainty, the average phonon energies  $\langle \hbar\omega_X \rangle$  for both A and B excitons are similar for all three materials and are close to the value of 22.1 meV reported for MoS<sub>2</sub> and WS<sub>2</sub> in literature.<sup>49,50</sup>

We analyze the temperature dependence of the linewidths of the Lorentzians in Equation A3.1 of the A and B exciton peaks by using the following expression<sup>51</sup>

$$\Gamma_X = \Gamma_{X,I} + \frac{\Gamma_{X,ph}}{e^{\frac{\langle \hbar\omega_X \rangle}{k_B T}} - 1} \quad 3.2$$

The first term at the right-hand side of Equation 3.2,  $\Gamma_{X,I}$ , represents inhomogeneous linewidth broadening induced by temperature-independent mechanisms, such as scattering of excitons on structural defects or impurities. The second term describes exciton-phonon scattering for both absorption and emission of phonons. The average energies of phonons that couple with excitons,  $\langle \hbar\omega_X \rangle$ , were taken equal to the values obtained from fitting Equation 3.1 to the peak energies, see Table 3.1.

The solid cyan lines in Figures 3.3a-c are the least-squares fits of Equation 3.2 to the FWHM values, with the latter obtained from fits of Equation A3.1 to the optical transmission spectra in Figure A3.2. The results for the inhomogeneous broadening,  $\Gamma_{X,I}$ , and the broadening due to exciton-phonon scattering,  $\Gamma_{X,ph}$ , are presented in Table 3.1. For each of the three materials, the values of the inhomogeneous broadening of the A exciton,  $\Gamma_{A,I}$ , are smaller than that of the B exciton,  $\Gamma_{B,I}$ , similar to results for single crystals.<sup>52</sup> Interestingly, the values of both  $\Gamma_{A,ph}$  and  $\Gamma_{B,ph}$  of the alloy are close to the corresponding values for MoS<sub>2</sub>, while they are significantly lower than those for WS<sub>2</sub>. This is in line with the exciton peak energies and the values of  $S_A$  and  $S_B$  for the alloy being nearest to those of MoS<sub>2</sub>, as discussed above. The larger exciton-phonon scattering rate for B excitons can be due to the additional

ultrafast decay channel of B excitons involving their relaxation to A excitons by emission of phonons, as discussed previously.<sup>53</sup>

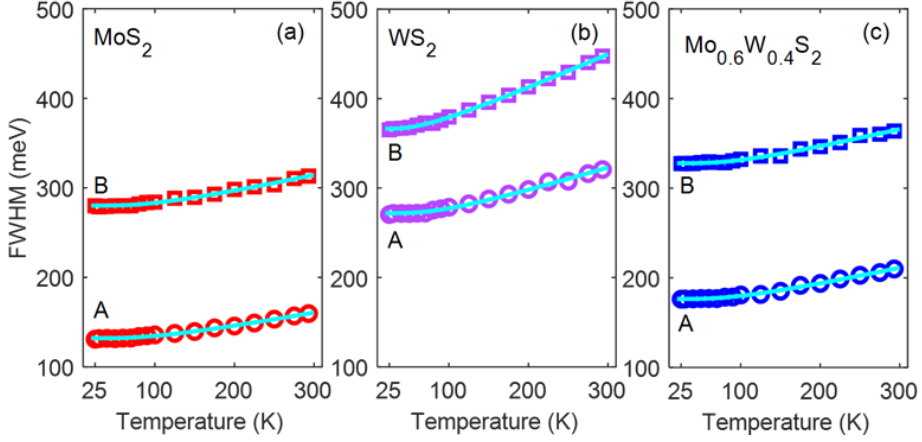


**Figure 3.3.** Temperature dependence of the linewidths (FWHM, markers) of the A and B exciton peaks for (a)  $\text{MoS}_2$ , (b)  $\text{WS}_2$  and (c) the  $\text{Mo}_{0.6}\text{W}_{0.4}\text{S}_2$  alloy. The solid cyan lines are fits to the experimental data.

Our values of  $E_{0,X}$ ,  $S_X$ ,  $\langle \hbar\omega_X \rangle$  and  $\Gamma_{X,\text{ph}}$  for ALD grown  $\text{MoS}_2$  and  $\text{WS}_2$  films are within the range reported for mono- or few-layer TMDC samples that were obtained by mechanical exfoliation or chemical vapor deposition (CVD),<sup>26,45,46,50,54–56</sup> and CVD grown bulk samples.<sup>27,50</sup> Note that the values of these parameters can vary from one sample to another due to differences in sample preparation, dielectric environment (in particular for mono- and few-layer samples), etc. Our values for the inhomogeneous linewidth broadening,  $\Gamma_{X,I}$ , are higher than those that Ho *et al.*<sup>27</sup> obtained from temperature-dependent piezoreflectance measurements on CVD-grown crystals of  $\text{MoS}_2$ ,  $\text{WS}_2$  and  $\text{Mo}_x\text{W}_{1-x}\text{S}_2$  alloys. This may result from a larger degree of structural disorder in our ALD-grown samples. Indeed the grain size in ALD grown samples is  $\sim 10$  nm, which is much smaller than for CVD-grown crystals.<sup>57</sup> Interestingly, the values of the electron-LO phonon coupling strength,  $\Gamma_{X,\text{ph}}$ , reported by Ho *et al.*<sup>27</sup> are a factor of 2-3 higher than ours. This could be due to the fact that their piezoreflectance measurements probe excitons near the sample surface, which would then appear to couple to surface-phonons with higher strength than the bulk exciton-phonon coupling probed in our experiments.

**Table 3.1.** Fitted values of the exciton-phonon coupling strength,  $S_X$ , the average phonon energy,  $\langle \hbar\omega_X \rangle$ , inhomogeneous linewidth broadening,  $\Gamma_{X,I}$ , and the electron-phonon interaction strength,  $\Gamma_{X,ph}$ , for MoS<sub>2</sub>, WS<sub>2</sub>, and the Mo<sub>0.6</sub>W<sub>0.4</sub>S<sub>2</sub> alloy.

	MoS <sub>2</sub>	WS <sub>2</sub>	Mo <sub>0.6</sub> W <sub>0.4</sub> S <sub>2</sub>
$E_{0A}$ (eV)	1.80 ± 0.01	1.96 ± 0.01	1.83 ± 0.01
$E_{0B}$ (eV)	1.97 ± 0.01	2.34 ± 0.01	2.09 ± 0.01
$S_A$	1.4 ± 0.2	1.9 ± 0.2	1.5 ± 0.1
$S_B$	1.5 ± 0.1	2.1 ± 0.1	1.6 ± 0.1
$\hbar\omega_A$ (meV)	26.4 ± 2.2	22.8 ± 3.1	24.4 ± 2.5
$\hbar\omega_B$ (meV)	26.4 ± 1.9	16.4 ± 3.5	24.4 ± 1.5
$\Gamma_{A,I}$ (meV)	132.1 ± 0.4	271.8 ± 0.9	176.4 ± 0.1
$\Gamma_{B,I}$ (meV)	280.2 ± 0.7	366.2 ± 0.6	327.8 ± 0.1
$\Gamma_{A,ph}$ (meV)	50.8 ± 1.8	72.4 ± 3.0	54.6 ± 1.9
$\Gamma_{B,ph}$ (meV)	60.8 ± 3.1	73.9 ± 1.6	59.7 ± 2.5

**3.3.3 TDDFT calculations of the optical absorption spectrum.** The real and imaginary parts of the dielectric functions obtained from the TDDFT calculations are shown in Figures A3.3–A3.5 and these were used to calculate the optical absorption coefficient,  $\alpha$ , according to Equation A3.3. The calculated absorption coefficients for MoS<sub>2</sub> and WS<sub>2</sub> are shown in Figure 3.4, together with the experimental data at 293 K. The optical absorption coefficients were obtained as described in Section 3.2.2, using the spectra of  $T$  and  $R$  in Figure A3.1. The calculations reproduce the relative

energies of the A and B excitons very well, see also Table A3.2. In addition, the calculations reproduce the magnitude of the optical absorption coefficient to within a factor two.

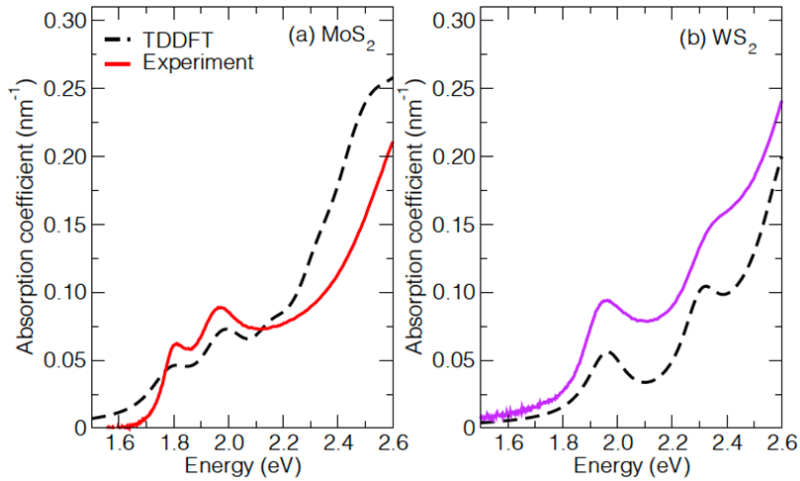


**Figure 3.4.** Absorption coefficient,  $\alpha$ , obtained from TDDFT calculations (black dashed curves) together with the experimental results at 293 K for (a)  $\text{MoS}_2$  and (b)  $\text{WS}_2$ .

As discussed in Section 3.2.2, we describe the  $\text{Mo}_{0.6}\text{W}_{0.4}\text{S}_2$  alloy by a periodic crystal structure with the smallest possible ( $2 \times 2 \times 1$ ) supercell resulting in the  $\text{Mo}_{0.625}\text{W}_{0.375}\text{S}_2$  alloy, see Figure 3.5. One unit cell then contains 5 Mo atoms, 3 W atoms and 16 S atoms that are arranged in two layers bonded by van der Waals forces. By permutation of the 5 Mo and 3 W atoms one can realize 28 different arrangements. These can be categorized into two groups: 1) 4 'heterogeneous' structures in which every other layer contains only Mo atoms and the layers in between contain also W atoms, and b) 24 'homogeneous' structures in which both layers contain Mo and W atoms. Applying the symmetry operations of translation, rotation, mirror planes, and their combinations, we obtain three physically distinct structures (I, II, and III), as shown in Figure 3.5.

The calculated optical absorption coefficient of the  $\text{Mo}_{0.625}\text{W}_{0.375}\text{S}_2$  alloy with heterogeneous structure I is shown in Figure 3.6a, together with the experimental spectrum. The presence of three peaks in the calculated spectrum disagrees with the two excitonic peaks in the experimental spectrum. We suspect, but cannot prove here, that the peak at the lowest energy calculated for structure I is due to excitons having some more charge transfer character than the peaks at higher

energy. For such excitons the electron would have a somewhat larger probability to reside on Mo atoms, while the hole is preferentially present on W atoms. Interestingly, the calculated spectra of structures II and III in Figure 3.6b agree with the experimental spectrum. The relative energies of the A and B exciton, as well as the magnitude of the optical absorption coefficient are very well reproduced by these structures, see also Table 3.2. From this we infer that the Mo and W atoms in the ALD-grown films are to a large extent mixed homogeneously, as in structures II and III. This agrees with the previously reported random arrangement of Mo and W atoms in monolayers of these alloys grown by chemical vapor transport.<sup>14,15</sup> The very different result from TDDFT calculations for structure I in Figure 3.6a, as compared with those for structures II and III in Figure 3.6b shows that the mutual arrangement of Mo and W atoms has a strong effect on the optical absorption spectrum.

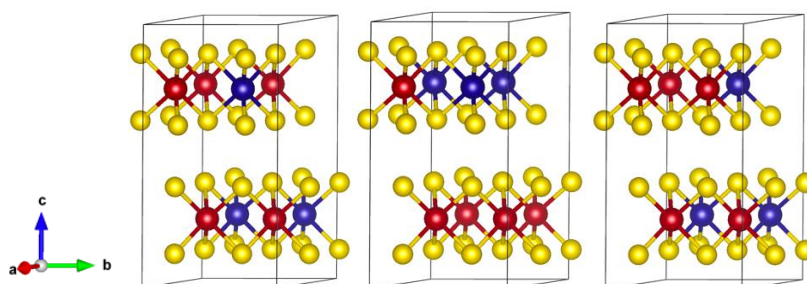


**Figure 3.5.** The three physically distinct arrangements of atoms in the  $\text{Mo}_{0.625}\text{W}_{0.375}\text{S}_2$  alloy. Each  $2 \times 2 \times 1$  supercell of the  $\text{Mo}_{0.625}\text{W}_{0.375}\text{S}_2$  alloy shows the different arrangements of metal and chalcogen atoms where the Mo atoms are red, the W atoms are blue and the S atoms are yellow. The heterogeneous structure I has alternating layers of Mo atoms only and layers containing both Mo and W atoms. In the homogeneous structures II and III all layers contain Mo and W atoms.

Unfortunately, the TDDFT calculations performed with the Elk code do not provide the atom resolved composition of the exciton wave functions and therefore we cannot obtain the distribution of the electron and hole within an exciton among the atoms. To investigate the spatial distribution of the electron and the hole within an exciton, calculations at a higher level of theory are needed; e.g. by describing excitons on the basis of the Bethe-Salpeter equation.<sup>58</sup>

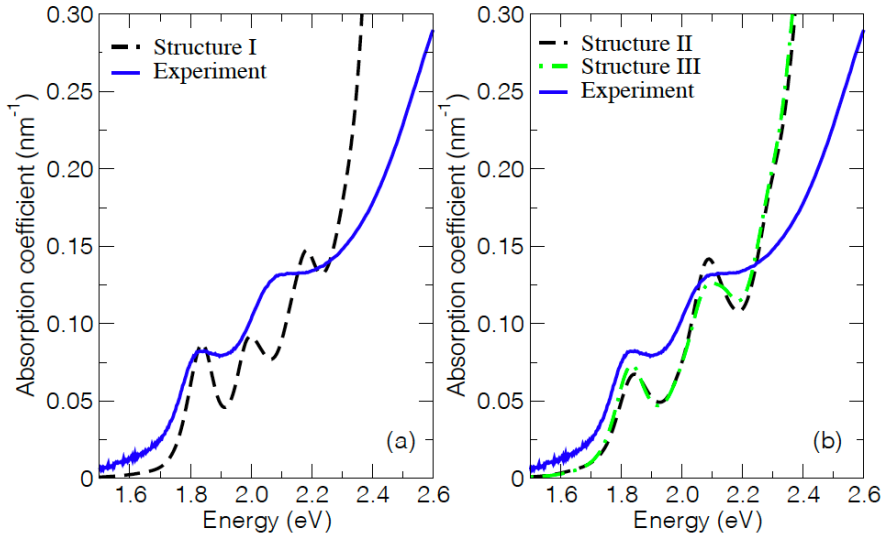


**Figure 3.6.** The calculated absorption coefficient of (a) structure I and (b) structures II and III of the  $\text{Mo}_{0.625}\text{W}_{0.375}\text{S}_2$  alloy, together with the experimental spectrum at room temperature (293 K).

**Table 3.2.** Energies of the A and B excitons in  $\text{MoS}_2$ ,  $\text{WS}_2$  and the  $\text{Mo}_{0.6}\text{W}_{0.4}\text{S}_2$  alloy. The last two rows show the energy difference between the exciton energies from experiments (exp.) and the TDDFT calculations.

	$\text{MoS}_2$	$\text{WS}_2$	$\text{Mo}_{0.6}\text{W}_{0.4}\text{S}_2$	$\text{Mo}_{0.625}\text{W}_{0.375}\text{S}_2$
$E_A$ (exp.) eV	1.80	1.96	1.83	
$E_B$ (exp.) eV	1.97	2.34	2.09	
$E_B - E_A$ (exp.) meV	170	380	260	
$E_B - E_A$ (TDDFT calc.) meV	179	353		255

### 3.4 Conclusions

We performed a combined experimental and time-dependent density functional theory (TDDFT) study of the optical absorption/transmission spectra of ALD-grown thin films of MoS<sub>2</sub>, WS<sub>2</sub> and the alloy Mo<sub>0.6</sub>W<sub>0.4</sub>S<sub>2</sub>. The temperature dependence of the peak energies and linewidths of the A and B excitons in the alloy is close to that for MoS<sub>2</sub>. This suggests that the exciton wave functions have a larger amplitude on Mo atoms than on W atoms. From comparison of the measured optical absorption spectra with those from TDDFT calculations we infer that Mo and W atoms are homogeneously distributed throughout the alloy. Further, the mutual arrangement of Mo and W atoms in the material has a strong effect on the shape of the optical absorption spectrum. These results provide clear support towards structural engineering of two-dimensional van der Waals materials through atomic arrangements, extending the already rich variety of properties in this class of materials.

## A3 Appendix to chapter 3

### A3.1 Transmission spectra of MoS<sub>2</sub>, WS<sub>2</sub>, and the Mo<sub>0.6</sub>W<sub>0.4</sub>S<sub>2</sub> alloy together with the fractions reflected and absorbed light.

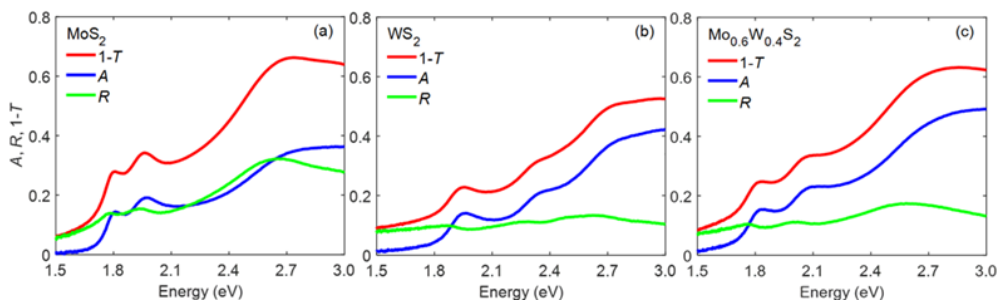


**Figure A3.1.** Room temperature transmission spectra ( $1-T$ ) and fractions reflected ( $R$ ) and absorbed ( $A = 1 - R - T$ ) light for MoS<sub>2</sub>, WS<sub>2</sub> and the Mo<sub>0.6</sub>W<sub>0.4</sub>S<sub>2</sub> alloy.

**A3.2 Fits to the temperature-dependent transmission spectra.** The optical transmission spectra were analyzed by fitting Equation A3.1 to the experimental results

$$1 - T(E) = \sum_{i=A,B} \frac{1}{2\pi} \frac{C_i \Gamma_i}{(E - E_i)^2 + (\Gamma_i/2)^2} + \sum_{j=1}^2 \frac{C_j}{\sigma_j \sqrt{2\pi}} e^{-\frac{(E - E_j)^2}{2\sigma_j^2}} \quad \text{A3.1}$$

with  $E$  the photon energy  $E$ . The two Lorentzian functions with amplitude  $C_i$  and linewidth  $\Gamma_i$  describe the A and B exciton peaks. The Gaussian functions describe optical reflection, below band gap absorption due to defects and the broad C absorption feature at higher energy. Figure A3.2 shows the fit results together with the experimental spectra.

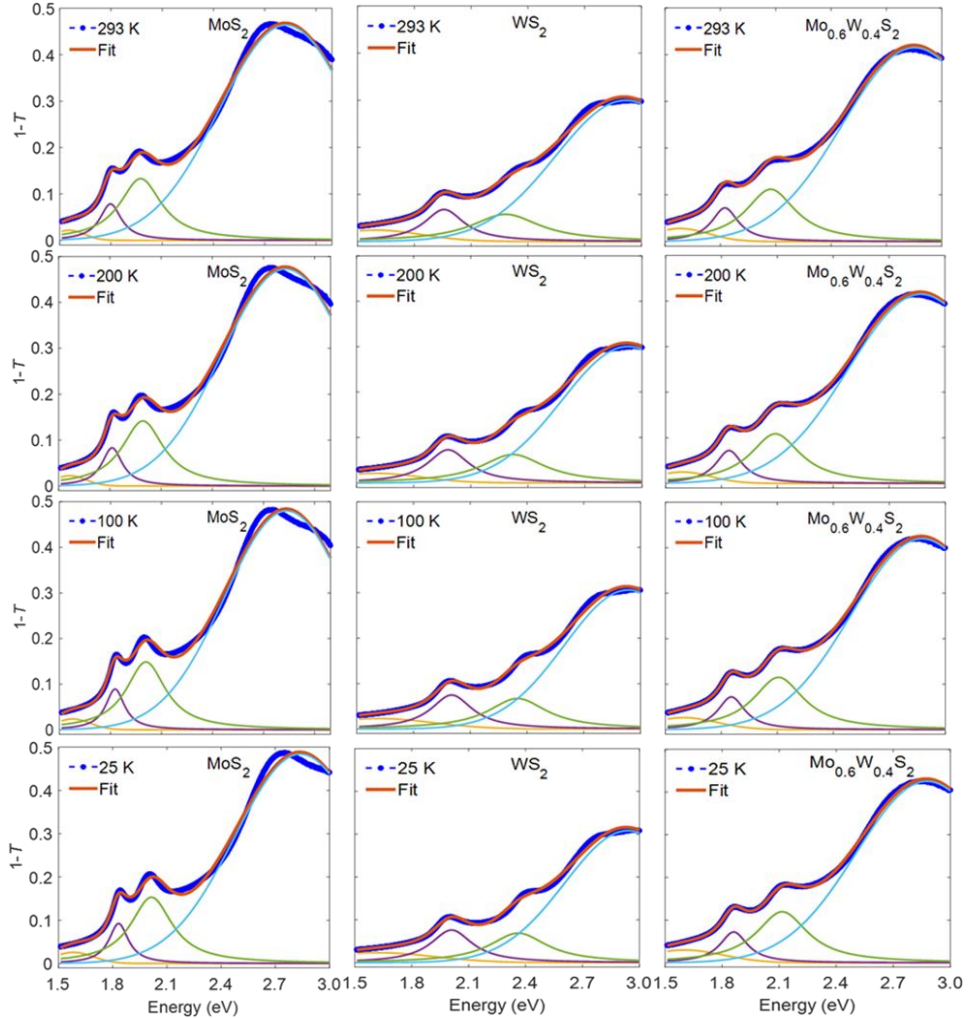


**Figure A3.2.** Fits to the experimental transmission spectra of  $\text{MoS}_2$ ,  $\text{WS}_2$ , and the  $\text{Mo}_{0.6}\text{W}_{0.4}\text{S}_2$  alloy at 293 K, 200 K, 100 K, and 25 K, respectively. The dark blue curves are the experimental spectra, the red curve is the fit of Equation A3.1 with the Lorentzian functions shown in purple and green and the Gaussians in yellow and light blue.

**A3.3 Relation between absorption coefficient and dielectric function.** The optical absorption coefficient,  $\alpha$ , can be obtained from the real ( $\varepsilon_1$ ) and imaginary ( $\varepsilon_2$ ) parts of the dielectric function using the following relations.<sup>59</sup>

$$n = \sqrt{\frac{1}{2} [[\varepsilon_1^2 + \varepsilon_2^2]^{1/2} + \varepsilon_1]}, \quad k = \sqrt{\frac{1}{2} [[\varepsilon_1^2 + \varepsilon_2^2]^{1/2} - \varepsilon_1]} \quad \text{A3.2}$$

and,

$$\alpha = 2\omega k/c \quad \text{A3.3}$$

where  $n$  is the refractive index,  $k$  the extinction coefficient and  $\omega$  the radian frequency of the light, respectively.

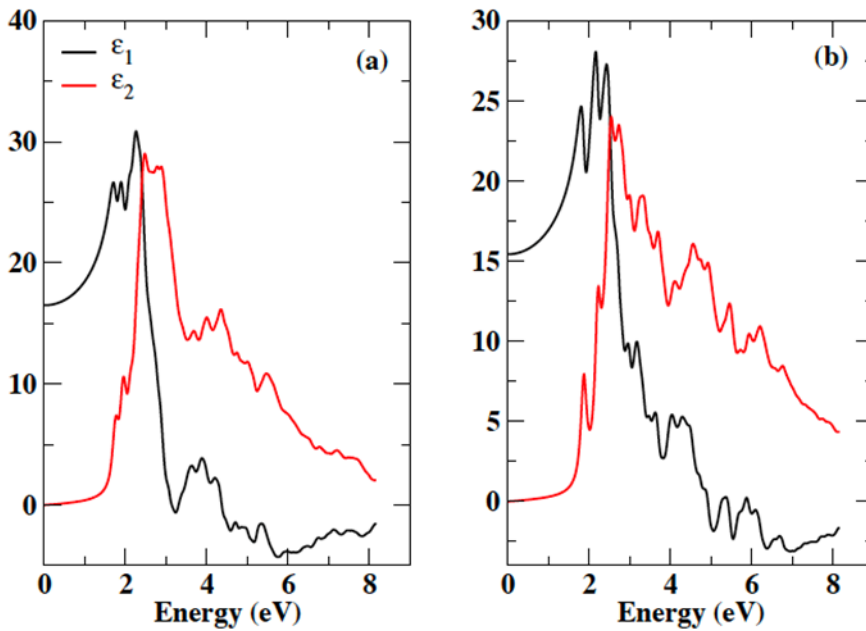


**Figure A3.3.** The real and imaginary part of the dielectric function obtained from the TDDFT calculations for (a) MoS<sub>2</sub> and (b) WS<sub>2</sub>.

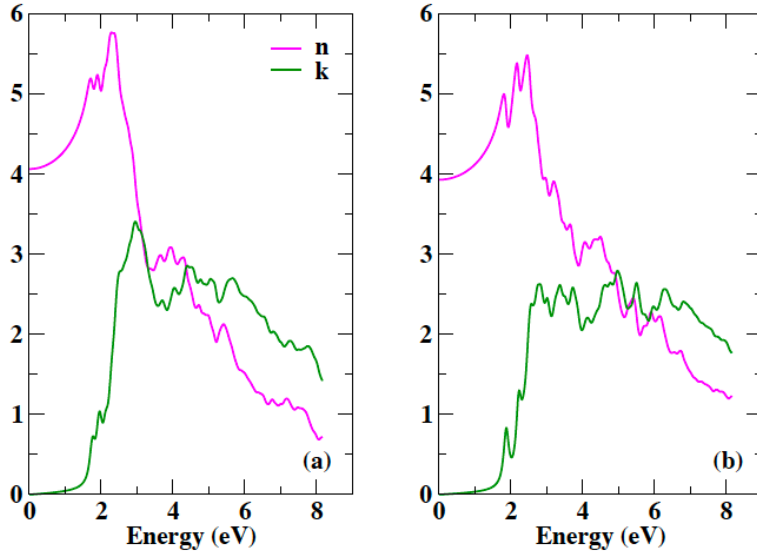


**Figure A3.4.** The refractive index and extinction coefficient obtained from Equation A3.2 for (a)  $\text{MoS}_2$  and (b)  $\text{WS}_2$ .

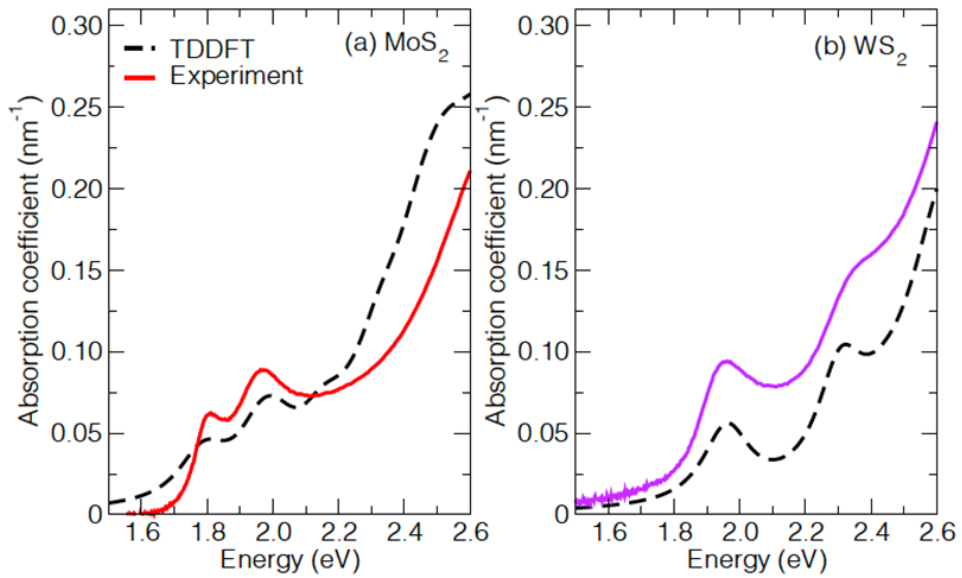


**Figure A3.5.** The absorption coefficient obtained from Equation A3.3 for (a)  $\text{MoS}_2$  and (b)  $\text{WS}_2$ . The TDDFT results have not been shifted in energy.

## References

- (1) Manzeli, S.; Ovchinnikov, D.; Pasquier, D.; Yazyev, O. V.; Kis, A. 2D Transition Metal Dichalcogenides. *Nat. Rev. Mater.* **2017**, *2*, 1–15.
- (2) Xia, J.; Huang, X.; Liu, L.-Z.; Wang, M.; Wang, L.; Huang, B.; Zhu, D.-D.; Li, J.-J.; Gu, C.-Z.; Meng, X.-M. CVD Synthesis of Large-Area, Highly Crystalline MoSe<sub>2</sub> Atomic Layers on Diverse Substrates and Application to Photodetectors. *Nanoscale* **2014**, *6*, 8949.
- (3) Late, D. J.; Huang, Y.-K.; Liu, B.; Acharya, J.; Shirodkar, S. N.; Luo, J.; Yan, A.; Charles, D.; Waghmare, U. V.; Dravid, V. P.; Rao, C. N. R. Sensing Behavior of Atomically Thin-Layered MoS<sub>2</sub> Transistors. *ACS Nano* **2013**, *7*, 4879–4891.
- (4) Donarelli, M.; Prezioso, S.; Perrozzi, F.; Bisti, F.; Nardone, M.; Giancaterini, L.; Cantalini, C.; Ottaviano, L. Response to NO<sub>2</sub> and Other Gases of Resistive Chemically Exfoliated MoS<sub>2</sub>-Based Gas Sensors. *Sens. Actuators B Chem.* **2015**, *207*, 602–613.
- (5) Feng, J.; Qian, X.; Huang, C.-W.; Li, J. Strain-Engineered Artificial Atom as a Broad-Spectrum Solar Energy Funnel. *Nat. Photonics* **2012**, *6*, 866–872.
- (6) Pospischil, A.; Furchi, M. M.; Mueller, T. Solar-Energy Conversion and Light Emission in an Atomic Monolayer p–n Diode. *Nat. Nanotechnol.* **2014**, *9*, 257–261.
- (7) Mueller, T.; Malic, E. Exciton Physics and Device Application of Two-Dimensional Transition Metal Dichalcogenide Semiconductors. *Npj 2D Mater. Appl.* **2018**, *2*, 1–12.
- (8) Wilson, J. A.; Yoffe, A. D. The Transition Metal Dichalcogenides Discussion and Interpretation of the Observed Optical, Electrical and Structural Properties. *Adv. Phys.* **1969**, *18*, 193–335.
- (9) Wang, Q. H.; Kalantar-Zadeh, K.; Kis, A.; Coleman, J. N.; Strano, M. S. Electronics and Optoelectronics of Two-Dimensional Transition Metal Dichalcogenides. *Nat. Nanotechnol.* **2012**, *7*, 699–712.
- (10) Splendiani, A.; Sun, L.; Zhang, Y.; Li, T.; Kim, J.; Chim, C.-Y.; Galli, G.; Wang, F. Emerging Photoluminescence in Monolayer MoS<sub>2</sub>. *Nano Lett.* **2010**, *10*, 1271–1275.

- (11) Mak, K. F.; He, K.; Shan, J.; Heinz, T. F. Control of Valley Polarization in Monolayer  $\text{MoS}_2$  by Optical Helicity. *Nat. Nanotechnol.* **2012**, *7*, 494–498.
- (12) Chernikov, A.; Berkelbach, T. C.; Hill, H. M.; Rigosi, A.; Li, Y.; Aslan, O. B.; Reichman, D. R.; Hybertsen, M. S.; Heinz, T. F. Exciton Binding Energy and Nonhydrogenic Rydberg Series in Monolayer  $\text{WS}_2$ . *Phys. Rev. Lett.* **2014**, *113*, 076802.
- (13) Song, J.-G.; Ryu, G. H.; Lee, S. J.; Sim, S.; Lee, C. W.; Choi, T.; Jung, H.; Kim, Y.; Lee, Z.; Myoung, J.-M. *et al.* Controllable Synthesis of Molybdenum Tungsten Disulfide Alloy for Vertically Composition-Controlled Multilayer. *Nat. Commun.* **2015**, *6*, 7817.
- (14) Chen, Y.; Xi, J.; Dumcenco, D. O.; Liu, Z.; Suenaga, K.; Wang, D.; Shuai, Z.; Huang, Y.-S.; Xie, L. Tunable Band Gap Photoluminescence from Atomically Thin Transition-Metal Dichalcogenide Alloys. *ACS Nano* **2013**, *7*, 4610–4616.
- (15) Dumcenco, D. O.; Kobayashi, H.; Liu, Z.; Huang, Y.-S.; Suenaga, K. Visualization and Quantification of Transition Metal Atomic Mixing in  $\text{Mo}_{1-x}\text{W}_x\text{S}_2$  Single Layers. *Nat. Commun.* **2013**, *4*, 1351.
- (16) Liu, H.; Antwi, K. K. A.; Chua, S.; Chi, D. Vapor-Phase Growth and Characterization of  $\text{Mo}_{1-x}\text{W}_x\text{S}_2$  ( $0 \leq x \leq 1$ ) Atomic Layers on 2-Inch Sapphire Substrates. *Nanoscale* **2014**, *6*, 624–629.
- (17) Rigosi, A. F.; Hill, H. M.; Rim, K. T.; Flynn, G. W.; Heinz, T. F. Electronic Band Gaps and Exciton Binding Energies in Monolayer  $\text{Mo}_x\text{W}_{1-x}\text{S}_2$  Transition Metal Dichalcogenide Alloys Probed by Scanning Tunneling and Optical Spectroscopy. *Phys. Rev. B* **2016**, *94*, 075440.
- (18) Gao, Y.; Liu, J.; Zhang, X.; Lu, G. Unraveling Structural and Optical Properties of Two-Dimensional  $\text{Mo}_x\text{W}_{1-x}\text{S}_2$  Alloys. *J. Phys. Chem. C* **2021**, *125*, 774–781.
- (19) Xi, J.; Zhao, T.; Wang, D.; Shuai, Z. Tunable Electronic Properties of Two-Dimensional Transition Metal Dichalcogenide Alloys: A First-Principles Prediction. *J. Phys. Chem. Lett.* **2014**, *5*, 285–291.
- (20) Kaasbjerg, K.; Thygesen, K. S.; Jacobsen, K. W. Phonon-Limited Mobility in n-Type Single-Layer  $\text{MoS}_2$  from First Principles. *Phys. Rev. B* **2012**, *85*, 115317.

- (21) Zhao, W.; Ribeiro, R. M.; Toh, M.; Carvalho, A.; Kloc, C.; Castro Neto, A. H.; Eda, G. Origin of Indirect Optical Transitions in Few-Layer MoS<sub>2</sub>, WS<sub>2</sub>, and WSe<sub>2</sub>. *Nano Lett.* **2013**, *13*, 5627–5634.
- (22) Ruppert, C.; Chernikov, A.; Hill, H. M.; Rigosi, A. F.; Heinz, T. F. The Role of Electronic and Phononic Excitation in the Optical Response of Monolayer WS<sub>2</sub> after Ultrafast Excitation. *Nano Lett.* **2017**, *17*, 644–651.
- (23) Raja, A.; Selig, M.; Berghäuser, G.; Yu, J.; Hill, H. M.; Rigosi, A. F.; Brus, L. E.; Knorr, A.; Heinz, T. F.; Malic, E.; Chernikov, A. Enhancement of Exciton–Phonon Scattering from Monolayer to Bilayer WS<sub>2</sub>. *Nano Lett.* **2018**, *18*, 6135–6143.
- (24) Selig, M.; Berghäuser, G.; Raja, A.; Nagler, P.; Schüller, C.; Heinz, T. F.; Korn, T.; Chernikov, A.; Malic, E.; Knorr, A. Excitonic Linewidth and Coherence Lifetime in Monolayer Transition Metal Dichalcogenides. *Nat. Commun.* **2016**, *7*, 13279.
- (25) Christiansen, D.; Selig, M.; Berghäuser, G.; Schmidt, R.; Niehues, I.; Schneider, R.; Arora, A.; de Vasconcellos, S. M.; Bratschitsch, R.; Malic, E. *et al.* Phonon Sidebands in Monolayer Transition Metal Dichalcogenides. *Phys. Rev. Lett.* **2017**, *119*, 187402.
- (26) Helmrich, S.; Schneider, R.; Achtstein, A. W.; Arora, A.; Herzog, B.; Vasconcellos, S. M. de; Kolarczik, M.; Schöps, O.; Bratschitsch, R.; Woggon, U. *et al.* Exciton–Phonon Coupling in Mono- and Bilayer MoTe<sub>2</sub>. *2D Mater.* **2018**, *5*, 045007.
- (27) Ho, C. H.; Wu, C. S.; Huang, Y. S.; Liao, P. C.; Tiong, K. K. Temperature Dependence of Energies and Broadening Parameters of the Band-Edge Excitons of Single Crystals. *J. Phys. Condens. Matter* **1998**, *10*, 9317–9328.
- (28) Schulpen, J. J. P. M.; Verheijen, M. A.; Kessels, W. M. M.; Vandalon, V.; Bol, A. A. Controlling Transition Metal Atomic Ordering in Two-Dimensional Mo<sub>1-x</sub>W<sub>x</sub>S<sub>2</sub> Alloys. *ArXiv211106289 Cond-Mat* **2021**.
- (29) Dewhurst, K.; Sharma, S.; Nordstrom, L.; Cricchio, F.; Bultmark, F.; Gross, H. Introduction To The Elk Code.
- (30) Perdew, J. P.; Burke, K.; Ernzerhof, M. Generalized Gradient Approximation Made Simple. *Phys. Rev. Lett.* **1996**, *77*, 3865–3868.

- (31) Petkov, V.; Billinge, S. J. L.; Larson, P.; Mahanti, S. D.; Vogt, T.; Rangan, K. K.; Kanatzidis, M. G. Structure of Nanocrystalline Materials Using Atomic Pair Distribution Function Analysis: Study of LiMoS<sub>2</sub>. *Phys. Rev. B* **2002**, *65*, 092105.
- (32) Schutte, W. J.; De Boer, J. L.; Jellinek, F. Crystal Structures of Tungsten Disulfide and Diselenide. *J. Solid State Chem.* **1987**, *70*, 207–209.
- (33) Sharma, S.; Dewhurst, J. K.; Gross, E. K. U. Optical Response of Extended Systems Using Time-Dependent Density Functional Theory. *Top. Curr. Chem.* **2014**, *347*, 235–257.
- (34) Wooten, F. *Optical Properties of Solids*; Academic Press, 2013.
- (35) Sharma, S.; Dewhurst, J. K.; Sanna, A.; Gross, E. K. U. Bootstrap Approximation for the Exchange-Correlation Kernel of Time-Dependent Density-Functional Theory. *Phys. Rev. Lett.* **2011**, *107*, 186401.
- (36) Zhao, W.; Ghorannevis, Z.; Amara, K. K.; Pang, J. R.; Toh, M.; Zhang, X.; Kloc, C.; Tan, P. H.; Eda, G. Lattice Dynamics in Mono- and Few-Layer Sheets of WS<sub>2</sub> and WSe<sub>2</sub>. *Nanoscale* **2013**, *5*, 9677.
- (37) Latzke, D. W.; Zhang, W.; Suslu, A.; Chang, T.-R.; Lin, H.; Jeng, H.-T.; Tongay, S.; Wu, J.; Bansil, A.; Lanzara, A. Electronic Structure, Spin-Orbit Coupling, and Interlayer Interaction in Bulk MoS<sub>2</sub> and WS<sub>2</sub>. *Phys. Rev. B* **2015**, *91*, 235202.
- (38) Fan, X.; Singh, D. J.; Zheng, W. Valence Band Splitting on Multilayer MoS<sub>2</sub>: Mixing of Spin–Orbit Coupling and Interlayer Coupling. *J. Phys. Chem. Lett.* **2016**, *7*, 2175–2181.
- (39) Palummo, M.; Bernardi, M.; Grossman, J. C. Exciton Radiative Lifetimes in Two-Dimensional Transition Metal Dichalcogenides. *Nano Lett.* **2015**, *15*, 2794–2800.
- (40) Qiu, D. Y.; da Jornada, F. H.; Louie, S. G. Optical Spectrum of MoS<sub>2</sub>: Many-Body Effects and Diversity of Exciton States. *Phys. Rev. Lett.* **2013**, *111*, 216805.
- (41) Kunstmann, J.; Wendumu, T. B.; Seifert, G. Localized Defect States in MoS<sub>2</sub> Monolayers: Electronic and Optical Properties. *Phys. Status Solidi B* **2017**, *254*, 1600645.

- (42) Peter, Y.U.; Cardona, M. *Fundamentals of Semiconductors: Physics and Materials Properties*, 4th ed.; Graduate Texts in Physics; Springer-Verlag: Berlin Heidelberg, 2010.
- (43) King-Smith, R. D.; Needs, R. J.; Heine, V.; Hodgson, M. J. A First-Principle Calculation of the Temperature Dependence of the Indirect Band Gap of Silicon. *Europhys. Lett. EPL* **1989**, *10*, 569–574.
- (44) Huang, J.; Hoang, T. B.; Mikkelsen, M. H. Probing the Origin of Excitonic States in Monolayer WSe<sub>2</sub>. *Sci. Rep.* **2016**, *6*, 22414.
- (45) Christopher, J. W.; Goldberg, B. B.; Swan, A. K. Long Tailed Trions in Monolayer MoS<sub>2</sub>: Temperature Dependent Asymmetry and Resulting Red-Shift of Trion Photoluminescence Spectra. *Sci. Rep.* **2017**, *7*, 14062.
- (46) He, Z.; Sheng, Y.; Rong, Y.; Lee, G.-D.; Li, J.; Warner, J. H. Layer-Dependent Modulation of Tungsten Disulfide Photoluminescence by Lateral Electric Fields. *ACS Nano* **2015**, *9*, 2740–2748.
- (47) O'Donnell, K. P.; Chen, X. Temperature Dependence of Semiconductor Band Gaps. *Appl. Phys. Lett.* **1991**, *58*, 2924–2926.
- (48) Wang, Z.-W.; Li, R.-Z.; Dong, X.-Y.; Xiao, Y.; Li, Z.-Q. Temperature Dependence of the Excitonic Spectra of Monolayer Transition Metal Dichalcogenides. *Front. Phys.* **2018**, *13*, 137305.
- (49) Gaur, A. P. S.; Sahoo, S.; Scott, J. F.; Katiyar, R. S. Electron–Phonon Interaction and Double-Resonance Raman Studies in Monolayer WS<sub>2</sub>. *J. Phys. Chem. C* **2015**, *119*, 5146–5151.
- (50) Dey, P.; Paul, J.; Wang, Z.; Stevens, C. E.; Liu, C.; Romero, A. H.; Shan, J.; Hilton, D. J.; Karaiskaj, D. Optical Coherence in Atomic-Monolayer Transition-Metal Dichalcogenides Limited by Electron-Phonon Interactions. *Phys. Rev. Lett.* **2016**, *116*, 127402.
- (51) Rudin, S.; Reinecke, T. L.; Segall, B. Temperature-Dependent Exciton Linewidths in Semiconductors. *Phys. Rev. B* **1990**, *42*, 11218–11231.
- (52) Evans, B. L.; Young, P. A. Optical Absorption and Dispersion in Molybdenum Disulphide. *Proc. R. Soc. Lond. Ser. Math. Phys. Sci.* **1965**, *284*, 402–422.

- (53) McCreary, K. M.; Hanbicki, A. T.; Sivaram, S. V.; Jonker, B. T. A- and B-Exciton Photoluminescence Intensity Ratio as a Measure of Sample Quality for Transition Metal Dichalcogenide Monolayers. *APL Mater.* **2018**, *6*, 111106.
- (54) Tongay, S.; Zhou, J.; Ataca, C.; Lo, K.; Matthews, T. S.; Li, J.; Grossman, J. C.; Wu, J. Thermally Driven Crossover from Indirect toward Direct Bandgap in 2D Semiconductors:  $\text{MoSe}_2$  versus  $\text{MoS}_2$ . *Nano Lett.* **2012**, *12*, 5576–5580.
- (55) Arora, A.; Koperski, M.; Nogajewski, K.; Marcus, J.; Faugeras, C.; Potemski, M. Excitonic Resonances in Thin Films of  $\text{WSe}_2$ : From Monolayer to Bulk Material. *Nanoscale* **2015**, *7*, 10421–10429.
- (56) Arora, A.; Nogajewski, K.; Molas, M.; Koperski, M.; Potemski, M. Exciton Band Structure in Layered  $\text{MoSe}_2$ : From a Monolayer to the Bulk Limit. *Nanoscale* **2015**, *7*, 20769–20775.
- (57) Mattinen, M.; Leskelä, M.; Ritala, M. Atomic Layer Deposition of 2D Metal Dichalcogenides for Electronics, Catalysis, Energy Storage, and Beyond. *Adv. Mater. Interfaces* **2021**, *8*, 2001677.
- (58) Martin, R. M.; Reining, L.; Ceperley, D. M. *Interacting Electrons: Theory and Computational Approaches*; Cambridge University Press: Cambridge, 2016.
- (59) Wooten, F. *Optical Properties of Solids*, Academic Press, New York and London, **1972**.



## Chapter 4

**Photogeneration, relaxation and many-body effects of excitons and charge carriers in MoS<sub>2</sub>, WS<sub>2</sub>, and the Mo<sub>0.6</sub>W<sub>0.4</sub>S<sub>2</sub> alloy, probed by transient optical absorption spectroscopy.**

## 4.1 Introduction

Transition metal dichalcogenide alloys (TMDC alloys) have gained widespread interest owing to their composition-dependent optoelectronic properties. These alloys can be denoted as  $M_yM'_{1-y}X_2$  and  $MX_{2y}X'_{2(1-y)}$ , where M is the metal atom and X is the chalcogen atom.<sup>1,2</sup> In TMDC alloys, fundamental properties such as effective masses and bandgap can be continuously and controllably tuned by changing the composition ( $y$ ).<sup>3,4</sup> Layers of TMDC alloys can be prepared by chemical vapor deposition (CVD), physical vapor deposition, and atomic layer deposition (ALD) growth methods.<sup>5-7</sup>

Up to now, pure TMDCs such as  $MoS_2$ ,  $WS_2$ ,  $MoSe_2$  and  $WSe_2$  have been extensively studied for their applications in photodetectors, solar cells, and light-emitting diodes.<sup>8-13</sup> In these materials, time-resolved studies such as transient optical absorption (TA) are of particular importance to understand the photophysical properties of generated charges and their decay on ultrashort timescales. Excitons, biexcitons, and trions have been found in layers of TMDCs<sup>14-17</sup> and a variety of distinct phenomena have been studied such as photogenerated charge carrier lifetimes,<sup>18,19</sup> exciton-exciton interactions,<sup>20</sup> spin-valley dynamics, etc.<sup>17,21</sup> In bulk TMDCs, studies revealed that the presence of free charges along with excitons dominates the TA spectral features.<sup>22</sup> However, the underlying physics of the observed complex spectral features is heavily debated and is explained by different phenomena in the literature.

In the present chapter, we discuss TA measurements on ALD grown  $MoS_2$ ,  $WS_2$ , and the  $Mo_{0.6}W_{0.4}S_2$  alloy with a thickness of a few layers. We start our analysis of TA data for the pure compounds ( $MoS_2$  and  $WS_2$ ) and compare the results with literature. Next, we discuss the effects of alloying on photogenerated charge carriers and excitons in the  $Mo_{0.6}W_{0.4}S_2$  alloy. We also address the effects of pump photon energy and pump laser fluence on charge and exciton dynamics. We performed fits to the TA spectra and obtained a time-dependent blueshift and linewidth narrowing of the A and B exciton peaks in all three compounds. These effects are independent of the incident pump photon energy and were found to depend on the absorbed photon fluence in the  $Mo_{0.6}W_{0.4}S_2$  alloy.

## 4.2 Materials and methods

**Samples.** The materials studied in this chapter are  $MoS_2$ ,  $WS_2$ , and the  $Mo_{0.6}W_{0.4}S_2$  alloy. These samples are grown on a quartz substrate by atomic layer deposition

method and have a thickness of 6.3 nm, 4.1 nm and 5.2 nm, respectively, as described previously.<sup>6</sup>

**Transient absorption measurements.** From transient absorption (TA) measurements, we obtained pump-induced changes in TA signal, defined as  $\Delta A = \log_{10}\left(\frac{I_{\text{off}}}{I_{\text{on}}}\right)$ . Here,  $I$  is the incident light on the detector with either pump on or pump off. The TA signal is a result of changes in the absorption and reflection. In our data analysis, four Lorentzian functions were used to fit the TA spectra. Two Lorentzians were used to describe the A and B excitons in the absence of the pump pulse and the other two Lorentzians described the excitons after the pump pulse.

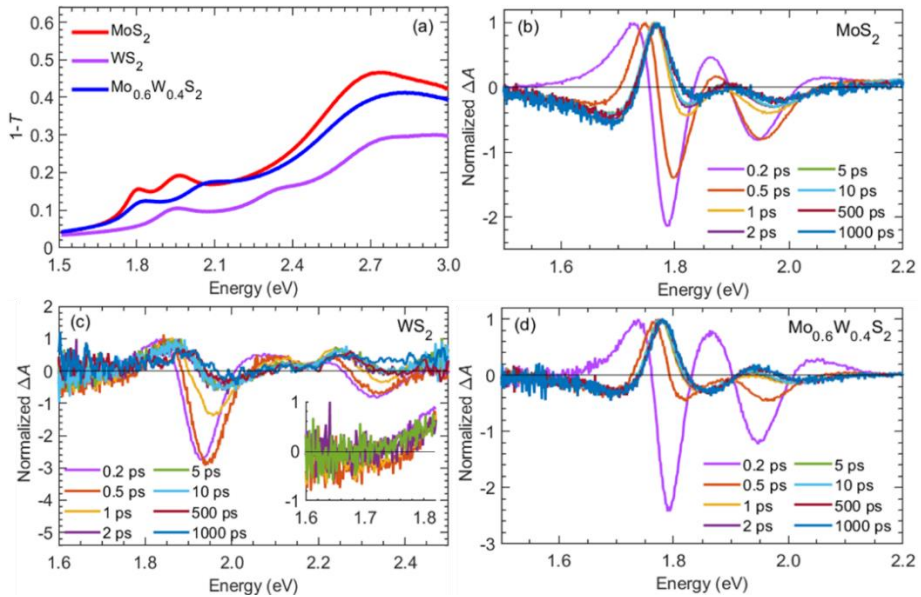
### 4.3 Results and discussion

Figure 4.1a shows the optical transmission spectrum of the Mo<sub>0.6</sub>W<sub>0.4</sub>S<sub>2</sub> alloy together with those of pure MoS<sub>2</sub> and WS<sub>2</sub> as reported previously.<sup>23</sup> Similar to MoS<sub>2</sub> and WS<sub>2</sub>,<sup>24,25</sup> the A and B exciton energy peaks are visible in the Mo<sub>0.6</sub>W<sub>0.4</sub>S<sub>2</sub> alloy spectrum and the alloy spectrum agrees well with that reported in the literature for a 60:40 composition.<sup>6</sup> The exciton peaks in the Mo<sub>0.6</sub>W<sub>0.4</sub>S<sub>2</sub> alloy are at energies in between those of MoS<sub>2</sub> and WS<sub>2</sub>. TD-DFT calculations on the Mo<sub>0.6</sub>W<sub>0.4</sub>S<sub>2</sub> alloy revealed that Mo and W atoms are homogeneously distributed in the alloy.<sup>23</sup>

Figures 4.1b-d show the TA spectra for MoS<sub>2</sub>, WS<sub>2</sub>, and the Mo<sub>0.6</sub>W<sub>0.4</sub>S<sub>2</sub> alloy obtained after photoexcitation with 3.1 eV pump photons for multiple probe delay times. The 3.1 eV pump photon energy is well above the exciton energies (Figure 4.1a) and as a consequence hot charges are generated initially by the pump. We obtained a series of complex spectral features around the A and B exciton energy levels for all three samples (Figures 4.1b-d). Below we first discuss the spectral features of the pure compounds and compare them with the existing literature.

The TA spectra of MoS<sub>2</sub> and WS<sub>2</sub> are shown in Figures 4.1b-c, respectively. At 0.2 ps after the pump pulse, a negative TA signal is present at the A and B exciton peak energies. In the literature, these negative features have been assigned to ground-state bleach due to the formation of excitons by the pump pulse in few layer samples of MoS<sub>2</sub> and WS<sub>2</sub>.<sup>26-28</sup> The positive features below the exciton bleach peaks are referred to as excited state absorption and have been assigned to trions, which are

generated by the probe pulses.<sup>29</sup> The negative transient absorption feature below the A exciton bleach peak was attributed to the filling of trap sites.<sup>30,31</sup>



**Figure 4.1.** (a) Optical transmission spectra of MoS<sub>2</sub>, WS<sub>2</sub>, and the Mo<sub>0.6</sub>W<sub>0.4</sub>S<sub>2</sub> alloy. (b) Normalized (at the maximum) TA spectra of MoS<sub>2</sub>, WS<sub>2</sub>, and the Mo<sub>0.6</sub>W<sub>0.4</sub>S<sub>2</sub> alloy obtained after photoexcitation with 3.1 eV pump photons and at an absorbed photon fluence of  $(2 \pm 1) \times 10^{12}$  photons cm<sup>-2</sup> per pulse.

According to other studies, the positive features below exciton bleach peaks at short times are due to carrier-induced spectral shifts and linewidth broadening.<sup>28,32</sup> Interestingly, a striking difference between the abovementioned studies reported in literature and our TA results is visible at 1 ps and higher probe delay times, and we observe the emergence of narrow positive features slightly below the exciton peak energies. The positive features are most prominent in MoS<sub>2</sub> and the Mo<sub>0.6</sub>W<sub>0.4</sub>S<sub>2</sub> alloy, while they are less prominent in WS<sub>2</sub> (see inset of Figure 4.1c). Tsokkou *et. al.*<sup>27</sup> have reported TA features in a few layers of mechanically exfoliated MoS<sub>2</sub>. In their case, the TA signal changed sign at 7 ps, which is later than our TA signals for pure MoS<sub>2</sub>. The positive features found by Tsokkou *et. al.* appeared around 7 ps and have the shape of the mirror image of the early TA spectrum. Our results agree with Tsokkou *et. al.* on early delay time, 0.2 ps, but after 1 ps, the results are unlike.

These differences could arise from the preparation methods as we are comparing ALD grown with CVD grown samples.

Next, we turn to the data obtained for the Mo<sub>0.6</sub>W<sub>0.4</sub>S<sub>2</sub> alloy. In the steady-state absorption spectra, the exciton peaks in the Mo<sub>0.6</sub>W<sub>0.4</sub>S<sub>2</sub> alloy lie closer to those in MoS<sub>2</sub> than WS<sub>2</sub>. At 0.2 ps, the TA spectrum of the Mo<sub>0.6</sub>W<sub>0.4</sub>S<sub>2</sub> alloy is similar to that of MoS<sub>2</sub> with a pronounced bleach at the exciton energy levels and positive features just below them. A narrow positive feature emerges within 0.5 ps in the Mo<sub>0.6</sub>W<sub>0.4</sub>S<sub>2</sub> alloy, which is earlier than MoS<sub>2</sub> and WS<sub>2</sub>, indicating faster charge carrier relaxation in the alloy.

The TA spectra are due to the superposition of several effects such as blue/red shifts of exciton energy levels and broadening/narrowing of the exciton linewidths. To understand the origin of these effects, we performed fits to the TA spectra as a function of probe photon energy,  $E$ , using a superposition of four Lorentzian energy profiles, according to  $\Delta A(E) = L_A^*(E; C_A^*, \Gamma_A^*, E_A^*) - L_A(E; C_A, \Gamma_A, E_A) + L_B^*(E; C_B^*, \Gamma_B^*, E_B^*) - L_B(E; C_B, \Gamma_B, E_B)$ . The fit parameters  $C_i, \Gamma_i, E_i$  are the amplitude, linewidth and peak energy of the Lorentzians. Details of the fit model are given in appendix A4.1 along with fit results.

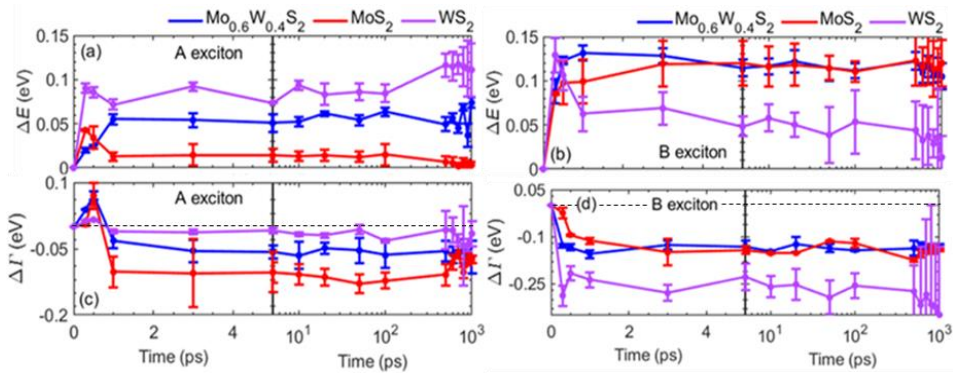


**Figure 4.2.** Energy shifts,  $\Delta E$ , and changes in the exciton linewidths,  $\Delta \Gamma$ , of the A and B excitons in MoS<sub>2</sub>, WS<sub>2</sub>, and the Mo<sub>0.6</sub>W<sub>0.4</sub>S<sub>2</sub> alloy after photoexcitation with 3.1 eV photons at the absorbed fluence of  $(2 \pm 1) \times 10^{12}$  photons cm<sup>-2</sup>.

After performing fits, we monitored the shifts of the A and B exciton peaks, ( $\Delta E$ ) and changes in the exciton linewidths ( $\Delta \Gamma$ ) for the three compounds (Figures 4.2a-d). From Figures 4.2a and c, we observe a blueshift ( $\Delta E > 0$ ) of the A exciton peak

and a linewidth narrowing ( $\Delta\Gamma < 0$ ) at 1 ps and onwards. The  $\text{Mo}_{0.6}\text{W}_{0.4}\text{S}_2$  alloy shows a blueshift and narrowing of the A exciton peak that is in between those of  $\text{MoS}_2$  and  $\text{WS}_2$ . Figures 4.2b and d show that the B exciton peak also blueshifts and its linewidth decreases for  $\text{MoS}_2$ ,  $\text{WS}_2$  and the alloy. For the B exciton, the magnitude of the shift and narrowing of the  $\text{Mo}_{0.6}\text{W}_{0.4}\text{S}_2$  alloy is similar to pure  $\text{MoS}_2$  after 1 ps and is much larger than for  $\text{WS}_2$ . In pure TMDCs, blueshift and/or redshift of the TA spectra have been previously observed for monolayers and bulk samples.<sup>26,27,32–36</sup> The energy shifts,  $\Delta E$ , at exciton energy levels occur due to the interplay between binding energy reduction, causing a blueshift and bandgap renormalization, which causes a redshift. In few layer TMDC samples, the presence of free charges has been attributed as a cause of the spectral blueshift and other changes in the spectral shape.<sup>27,37</sup> These free charges can be generated either by exciton dissociation via intervalley scattering or exciton quenching at trap sites, resulting in the change of the TA spectra on a timescale less than 1 ps after photoexcitation. After 1 ps, we do not expect a major contribution from A excitons, since they have an energy above the indirect band gap and exciton dissociation leading to charges at the indirect band edges is likely. Note, that excitons may also exist at the indirect band gap.<sup>38</sup>

In addition to blueshift, linewidth narrowing of the exciton features is obtained from our fits. The linewidth narrowing ( $\Delta\Gamma < 0$ ) is maximum within 1 ps and remains constant during the entire experimental time range of 2.5 ns. Recently, Schiettecatte *et. al.* have argued that homogenization of the local environment in a few layer  $\text{ReS}_2$  sample can result in linewidth narrowing.<sup>34</sup> The photogenerated free charges screen the parasitic in-plane electric fields. The latter arises from the local potential such as charged or ionized defects<sup>39,40</sup> or due to pre-existing built-in fields. The linewidth narrowing in the few layer ALD grown  $\text{MoS}_2$ ,  $\text{WS}_2$ , and the  $\text{Mo}_{0.6}\text{W}_{0.4}\text{S}_2$  alloy could also be due to the reduction of inhomogeneous broadening by photogenerated free charges.

**Effects of pump photon energy.** We studied effects of pump photon energy on the linewidth narrowing and the energy shift of the exciton peaks of the  $\text{Mo}_{0.6}\text{W}_{0.4}\text{S}_2$  alloy. Figures 4.3a-e show the normalized  $|\Delta A|/I_{\text{abs}}$  spectra for pump photon energies equal to 1.86 eV and 3.1 eV, respectively. Here,  $I_{\text{abs}}$  is the absorbed pump photon fluence. Soon after photoexcitation, at 0.2 ps, bleach peaks along with positive features are present for both pump energies. Upon 3.1 eV photoexcitation, hot charges are generated at higher energy in the conduction and valence bands. From 2 ps onwards, they have relaxed, as the shape of the TA spectra for both pump

photon energies is similar. The charges will relax to the indirect band gap with the conduction band edge at the Q valley.<sup>41</sup> We cannot exclude that the sub-ps decay is partly due to carrier capture by defect states.<sup>31,42</sup>

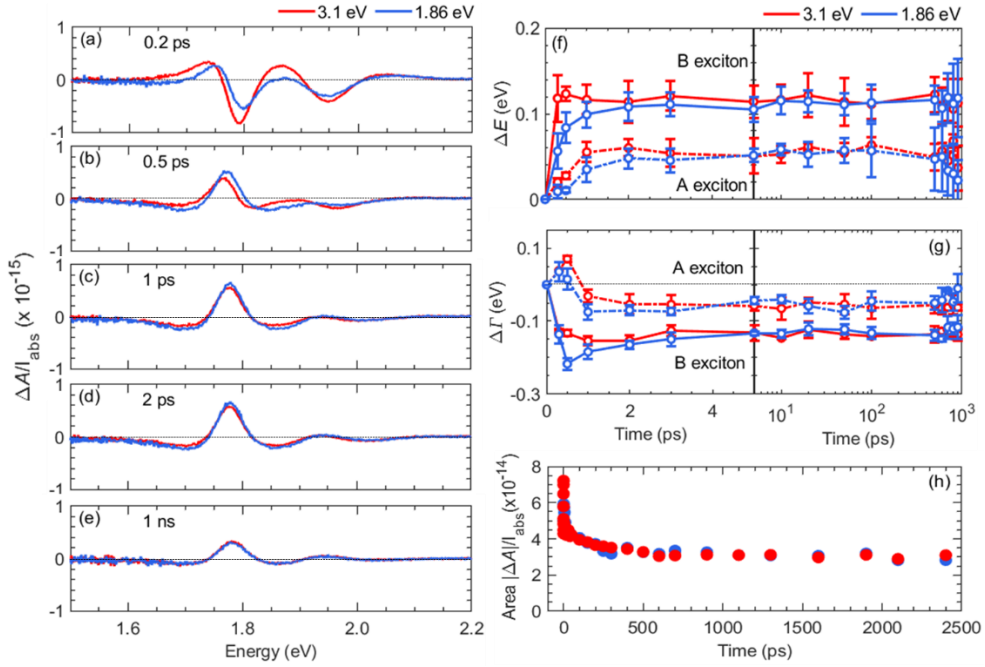


**Figure 4.3.** Transient absorption spectra at probe delay times (a) 0.2 ps, (b) 0.5 ps, (c) 1 ps, (d) 2 ps, and (e) 1 ns. The signals are obtained after photoexcitation with 1.86 eV and 3.1 eV pump photon energies and are plotted after normalizing with the absorbed photon fluence of  $(1.5 \pm 0.2) \times 10^{12}$  photons  $\text{cm}^{-2}$ . (f) The energy shifts ( $\Delta E$ ) of the A (dashed line) and B excitons (solid line) as a function of probe delay time. (g) The change in exciton linewidths ( $\Delta \Gamma$ ) as a function of probe delay time. (h) The decay of the normalized absolute integrated area,  $|\Delta A|/I_{\text{abs}}$  for 3.1 eV and 1.86 eV pump photon energies.

Figures 4.3f-g show the fit results ( $\Delta E$ ,  $\Delta \Gamma$ ) for the A and B excitons. We observe blueshifts for the A (dashed line) and B (solid line) exciton peaks. At short times up to 1 ps, for 3.1 eV pump photon energy, the A and B exciton peaks are shifted to higher energies by 50 meV and 120 meV, respectively. For 1.86 eV pump energy, the shifts for A and B excitons at short time of 1 ps are 30 meV and 80 meV to higher energy, respectively. The magnitude of the energy shift and linewidth narrowing is found to depend on the incident pump photon energy for probe delay times,  $t < 1$  ps. For 3.1 eV pump energy, hotter charges with more excess energy above the band

gap are created than in the case of 1.86 eV pump photons. Hotter charges can cause more linewidth broadening by interactions (scattering) with excitons produced by the probe pulse. Hotter charges can also reduce the exciton binding energy, which leads to a larger blueshift of the exciton peaks. By contrast, upon resonant excitation the photogenerated charges do not possess excess kinetic energy which results in reduced initial broadening and screening of the excitons. Once the hot charges relax at the conduction band minimum, the TA spectra for high and low-energy photoexcitations are similar (Figures 4.3d-e). We observe different values of the energy shifts and linewidth narrowing for the A and the B excitons. This could be due to different intrinsic properties of the excitons such as exciton radius and effective masses.<sup>43</sup> Figure 4.3h shows the normalized absolute integrated area,  $|\Delta A|/I_{\text{abs}}$ , for 1.86 eV and 3.1 eV, respectively. We observe decay of the photoexcited population and part of the carriers has not decayed within the range of our probing time until 2.5 ns.

**Effects of pump photon fluence.** Next, we varied the absorbed pump photon fluence,  $I_{\text{abs}}$ , from  $0.13 \times 10^{13}$  photons  $\text{cm}^{-2}$  to  $1.3 \times 10^{13}$  photons  $\text{cm}^{-2}$ , to study the effects of the charge carrier density on the spectral features. In Figures 4.4a-d, the  $\Delta A/I_{\text{abs}}$  spectra are plotted at 0.2 ps, 0.5 ps, 1 ps, and 1 ns. Negative and positive features are visible near the exciton energy levels. On increasing the pump photon fluence the shape of the TA spectra changes. At higher pump fluences, the positive TA features near the energies of the A and B exciton peaks exhibit a redshift. Recently, Wang *et. al.* performed TA measurements on a liquid phase exfoliated  $\text{Mo}_{0.5}\text{W}_{0.5}\text{S}_2$  alloy and reported TA spectra after resonant and non-resonant pump photon excitations for different pump photon fluences.<sup>44</sup> The shapes of their TA spectra are different from our ALD grown  $\text{Mo}_{0.6}\text{W}_{0.4}\text{S}_2$  alloy at low pump fluences, in particular at 1.7 eV, at all probe delay times. At high pump fluence, our results agree with those of Wang *et. al.* with positive TA features at 1.7 eV at all probe delay times. The positive feature at high pump photon fluence at probe photon energy below the A exciton energy could be due to the formation of trions, since the formation of an exciton by the probe pulse near a charge produced by the pump pulse becomes more likely at a higher pump fluence.

We applied the above-mentioned fit procedure to the TA spectra for the lowest and highest fluences in Figures 4.4a-d. The results are plotted in Figures 4.4e-f. Figure 4.4e shows the energy shifts,  $\Delta E$ , of the A and B excitons at the lowest and highest absorbed pump photon fluences. At high fluence, the A exciton shows a

crossover from blueshift to redshift within 1 ps. For the B exciton, we obtained a slightly smaller blueshift at the higher excitation density.

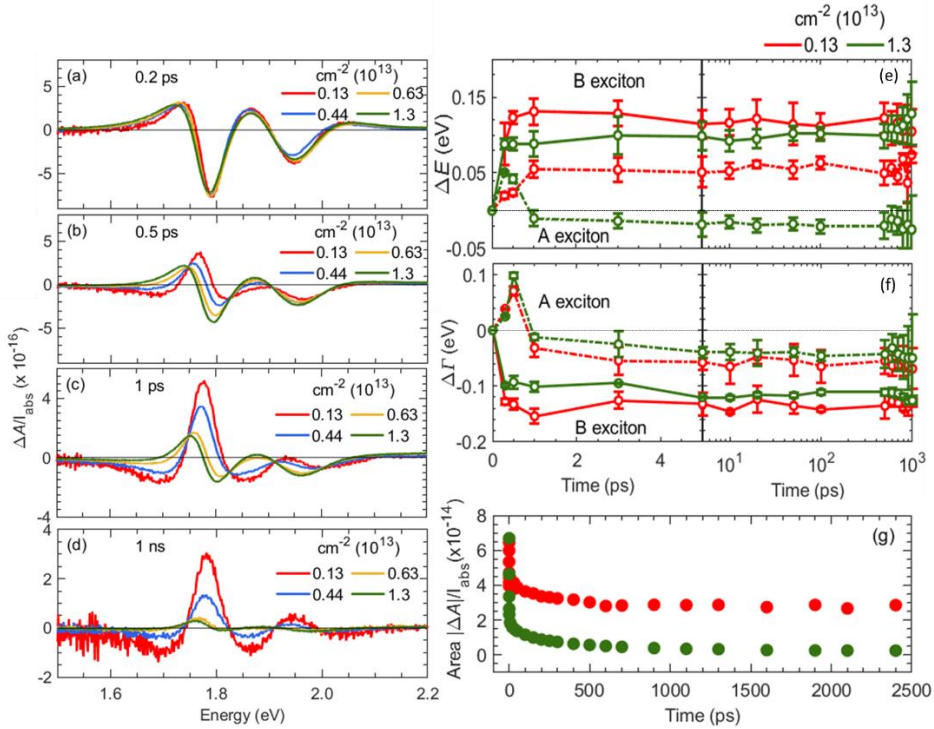


**Figure 4.4.** (a-d) Fluence-dependent spectral dynamics of the Mo<sub>0.6</sub>W<sub>0.4</sub>S<sub>2</sub> alloy at 0.2 ps, 0.5 ps, 1 ps, and 1 ns after photoexcitation with 3.1 eV pump photon energy. (e-f) The energy shifts ( $\Delta E$ ) and changes in the linewidths ( $\Delta \Gamma$ ) of the A (dashed line) and B excitons (solid line) at the lowest and highest absorbed pump photon fluences. (g) The decay of the normalized absolute integrated area,  $|\Delta A|/I_{\text{abs}}$  is plotted at the lowest and highest absorbed photon fluence.

The redshift of the A exciton at higher absorbed pump fluence can be explained by the presence of a higher carrier density.<sup>45–47</sup> For the absorbed pump photon density of  $1.3 \times 10^{13}$  photons  $\text{cm}^{-2}$  the distance,  $d$ , between photogenerated charges is  $\sim 3$  nm. This distance is close to the exciton Bohr diameter of  $\sim 4$  nm and  $\sim 6$  nm in bulk MoS<sub>2</sub><sup>48</sup> and WS<sub>2</sub>,<sup>49,50</sup> respectively. This suggests significant many-body interactions between excitons produced by the probe pulse and charges left after the pump pulse. Hence, electrons and holes within an exciton will interact with the charges produced by the pump pulse. Note, that in general, a redshift could result from lattice heating, due to the energy transfer of initially hot electrons and holes to phonons.<sup>47,51</sup> However, we do not expect significant lattice heating, since the

estimated increase of the lattice temperature,  $\Delta T$ , is reported to be only a few degrees Kelvin for the pure compounds at our pump photon fluences.<sup>51–54</sup> In addition to redshift, the decrease of the A and B exciton linewidths are found to be relatively smaller at the highest pump fluence, see Figure 4.4f. With increased pump photon density, the observed relative broadening is a result of the collisional broadening.<sup>45,55</sup> Charge carriers can scatter via carrier-carrier or carrier-phonon scattering mechanisms resulting in broader exciton peaks at higher pump photon fluence.

In Figure 4.4g, the normalized absolute integrated area,  $|\Delta A|/I_{\text{abs}}$ , is plotted until 2.5 ns for two different pump photon fluences. This quantity is a measure of the quantum yield of photogenerated charges. On early probe times ( $t < 1$  ps) the value of  $|\Delta A|/I_{\text{abs}}$  is similar, which implies that the initial quantum yield is independent of pump fluence. At later times, a fast decay is observed for the highest pump photon fluence, which is due to high-order recombination of electrons and holes.

## 4.4 Conclusions

In summary, we have analyzed photogenerated exciton and charge carrier dynamics in ALD grown  $\text{MoS}_2$ ,  $\text{WS}_2$ , and the  $\text{Mo}_{0.6}\text{W}_{0.4}\text{S}_2$  alloy using time-resolved pump-probe measurements. In all three compounds, the A and B excitons peaks show a blueshift and linewidth narrowing on the probed timescale up to 2.5 ns after the pump pulse. Upon photoexcitation, free charges are generated within 1 ps, which can screen the electron-hole attraction in an exciton, causing a blueshift. Charges can cause a linewidth narrowing by homogenizing the local environment around an exciton in the material. Our pump photon energy and photon fluence-dependent measurements on the  $\text{Mo}_{0.6}\text{W}_{0.4}\text{S}_2$  alloy revealed that the A exciton linewidth narrowing and blueshift depend on the density of photogenerated charges.

## A4 Appendix to chapter 4

**A4.1 Fits to the transient absorption spectra of MoS<sub>2</sub>, WS<sub>2</sub>, and the Mo<sub>0.6</sub>W<sub>0.4</sub>S<sub>2</sub> alloy.** The transient absorption spectra as a function of probe photon energy,  $E$ , are analyzed by fitting the following equation to the experimental results:

$$\Delta A(E) = \frac{1}{2\pi} \left( \frac{C_A^* \Gamma_A^*}{(E - E_A^*)^2 + (0.5\Gamma_A^*)^2} - \frac{C_A \Gamma_A}{(E - E_A)^2 + (0.5\Gamma_A)^2} \right) + \frac{1}{2\pi} \left( \frac{C_B^* \Gamma_B^*}{(E - E_B^*)^2 + (0.5\Gamma_B^*)^2} - \frac{C_B \Gamma_B}{(E - E_B)^2 + (0.5\Gamma_B)^2} \right)$$

$E_A^*$ ,  $E_B^*$ ,  $E_A$  and  $E_B$  are the excited (i.e. after the pump pulse) and ground state energies of the A and B excitons, respectively.  $\Gamma_A^*$ ,  $\Gamma_B^*$ ,  $\Gamma_A$  and  $\Gamma_B$  are the excited and ground state linewidths of the A and B excitons and  $C_A^*$ ,  $C_B^*$ ,  $C_A$  and  $C_B$  are their amplitudes. Figure A4.1 shows the fit results together with the experimental spectra. Here, MoS<sub>2</sub>, WS<sub>2</sub>, and the Mo<sub>0.6</sub>W<sub>0.4</sub>S<sub>2</sub> alloy are photoexcited by 3.1 eV pump photon energy and at the absorbed pump photon fluence of  $(2 \pm 1) \times 10^{12}$  photons cm<sup>-2</sup>.

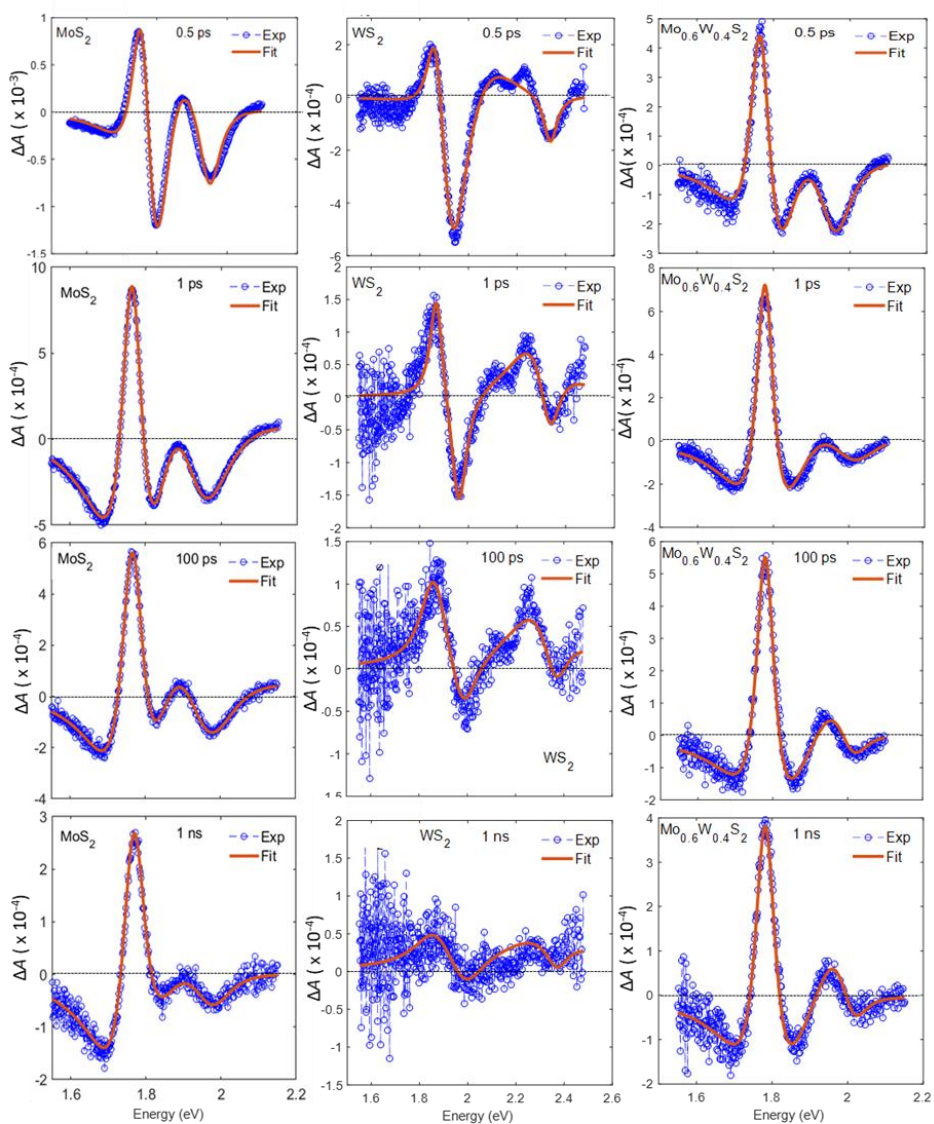


**Figure A4.1.** Fits to the experimental  $\Delta A$  spectra of MoS<sub>2</sub>, WS<sub>2</sub>, and the Mo<sub>0.6</sub>W<sub>0.4</sub>S<sub>2</sub> alloy after photoexcitation with 3.1 eV. The dark blue curves are the experimental spectra, and the red curves are fits of the equation above.

**A4.2 Fits to the TA spectra of the Mo<sub>0.6</sub>W<sub>0.4</sub>S<sub>2</sub> alloy after photoexcitation with 3.1 eV pump photon energy at the absorbed pump photon fluence of  $1.3 \times 10^{13}$  photons cm<sup>-2</sup>.**

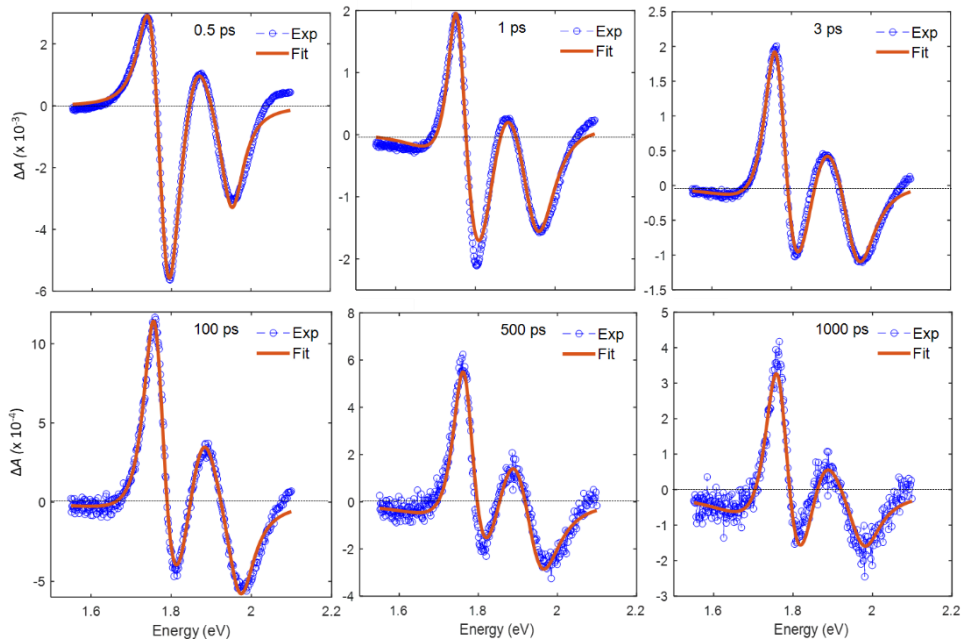


**Figure A4.2.** Fits to the  $\Delta A$  spectra of the Mo<sub>0.6</sub>W<sub>0.4</sub>S<sub>2</sub> alloy at 0.5 ps, 1 ps, 3 ps, 100 ps, 500 ps, and 1000 ps.

**A4.3 Fits to the TA spectra of the Mo<sub>0.6</sub>W<sub>0.4</sub>S<sub>2</sub> alloy at 1.86 eV pump photon energy.**

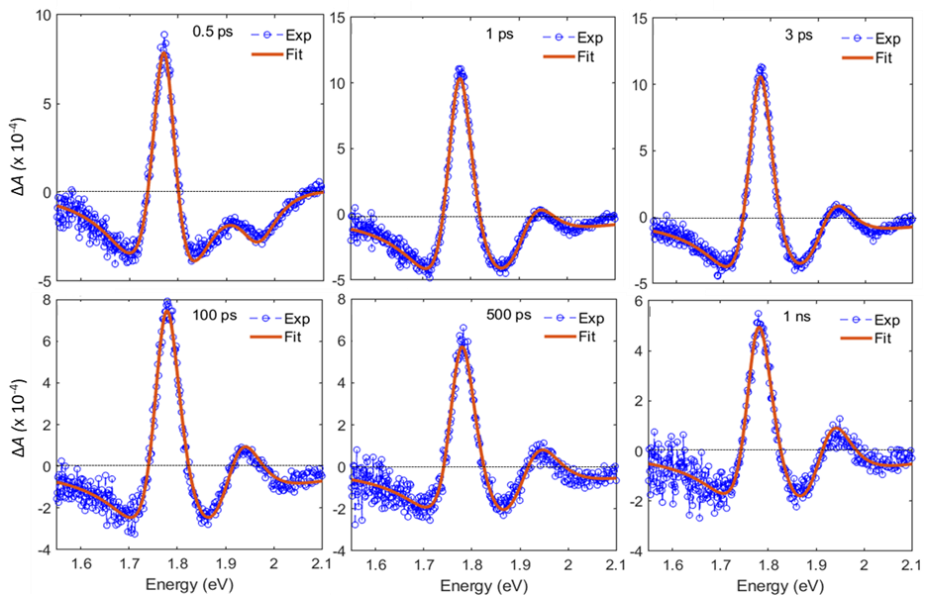


**Figure A4.3.** Fits to the  $\Delta A$  spectra of the Mo<sub>0.6</sub>W<sub>0.4</sub>S<sub>2</sub> alloy at 0.5 ps, 1 ps, 3 ps, 100 ps, 500 ps, and 1 ns.

## References

- (1) Song, J.-G.; Ryu, G. H.; Lee, S. J.; Sim, S.; Lee, C. W.; Choi, T.; Jung, H.; Kim, Y.; Lee, Z.; Myoung, J.-M.; Dussarrat, C.; Lansalot-Matras, C.; Park, J.; Choi, H.; Kim, H. Controllable Synthesis of Molybdenum Tungsten Disulfide Alloy for Vertically Composition-Controlled Multilayer. *Nat. Commun.* **2015**, *6*, 7817.
- (2) Chen, Y.; Xi, J.; Dumcenco, D. O.; Liu, Z.; Suenaga, K.; Wang, D.; Shuai, Z.; Huang, Y.-S.; Xie, L. Tunable Band Gap Photoluminescence from Atomically Thin Transition-Metal Dichalcogenide Alloys. *ACS Nano* **2013**, *7*, 4610–4616.
- (3) Kutana, A.; Penev, E. S.; Yakobson, B. I. Engineering Electronic Properties of Layered Transition-Metal Dichalcogenide Compounds through Alloying. *Nanoscale* **2014**, *6*, 5820–5825.
- (4) Xi, J.; Zhao, T.; Wang, D.; Shuai, Z. Tunable Electronic Properties of Two-Dimensional Transition Metal Dichalcogenide Alloys: A First-Principles Prediction. *J. Phys. Chem. Lett.* **2014**, *5*, 285–291.
- (5) Zheng, S.; Sun, L.; Yin, T.; Dubrovkin, A. M.; Liu, F.; Liu, Z.; Shen, Z. X.; Fan, H. J. Monolayers of  $W_xMo_{1-x}S_2$  Alloy Heterostructure with In-Plane Composition Variations. *Appl. Phys. Lett.* **2015**, *106*, 063113.
- (6) Schulpen, J. J. P. M.; Verheijen, M. A.; Kessels, W. M. M. (Erwin); Vandalon, V.; Bol, A. A. Controlling Transition Metal Atomic Ordering in Two-Dimensional  $Mo_{1-x}W_xS_2$  Alloys. *2D Mater.* **2022**, *9*, 025016.
- (7) Xie, L. M. Two-Dimensional Transition Metal Dichalcogenide Alloys: Preparation, Characterization and Applications. *Nanoscale* **2015**, *7*, 18392–18401.
- (8) Manzeli, S.; Ovchinnikov, D.; Pasquier, D.; Yazyev, O. V.; Kis, A. 2D Transition Metal Dichalcogenides. *Nat. Rev. Mater.* **2017**, *2*.
- (9) Xia, J.; Huang, X.; Liu, L.-Z.; Wang, M.; Wang, L.; Huang, B.; Zhu, D.-D.; Li, J.-J.; Gu, C.-Z.; Meng, X.-M. CVD Synthesis of Large-Area, Highly Crystalline  $MoSe_2$  Atomic Layers on Diverse Substrates and Application to Photodetectors. *Nanoscale* **2014**, *6*, 8949.
- (10) Late, D. J.; Huang, Y.-K.; Liu, B.; Acharya, J.; Shirodkar, S. N.; Luo, J.; Yan, A.; Charles, D.; Waghmare, U. V.; Dravid, V. P.; Rao, C. N. R. Sensing Behavior of Atomically Thin-Layered  $MoS_2$  Transistors. *ACS Nano* **2013**, *7*, 4879–4891.
- (11) Donarelli, M.; Prezioso, S.; Perrozzi, F.; Bisti, F.; Nardone, M.; Giancaterini, L.; Cantalini, C.; Ottaviano, L. Response to  $NO_2$  and Other Gases of Resistive

- Chemically Exfoliated MoS<sub>2</sub>-Based Gas Sensors. *Sens. Actuators B Chem.* **2015**, *207*, 602–613.
- (12) Pospischil, A.; Furchi, M. M.; Mueller, T. Solar-Energy Conversion and Light Emission in an Atomic Monolayer p–n Diode. *Nat. Nanotechnol.* **2014**, *9*, 257–261.
- (13) Mueller, T.; Malic, E. Exciton Physics and Device Application of Two-Dimensional Transition Metal Dichalcogenide Semiconductors. *Npj 2D Mater. Appl.* **2018**, *2*, 1–12.
- (14) Xiao, J.; Zhao, M.; Wang, Y.; Zhang, X. Excitons in Atomically Thin 2D Semiconductors and Their Applications. *Nanophotonics* **2017**, *6*.
- (15) Sie, E. J.; Frenzel, A. J.; Lee, Y.-H.; Kong, J.; Gedik, N. Intervalley Biexcitons and Many-Body Effects in Monolayer MoS<sub>2</sub>. *Phys. Rev. B* **2015**, *92*, 125417.
- (16) Chowdhury, R. K.; Nandy, S.; Bhattacharya, S.; Karmakar, M.; Bhaktha, S. N. B.; Datta, P. K.; Taraphder, A.; Ray, S. K. Ultrafast Time-Resolved Investigations of Excitons and Biexcitons at Room Temperature in Layered WS<sub>2</sub>. *2D Mater.* **2018**, *6*, 015011.
- (17) Mai, C.; Barrette, A.; Yu, Y.; Semenov, Y. G.; Kim, K. W.; Cao, L.; Gundogdu, K. Many-Body Effects in Valleytronics: Direct Measurement of Valley Lifetimes in Single-Layer MoS<sub>2</sub>. *Nano Lett.* **2014**, *14*, 202–206.
- (18) Wang, R.; Ruzicka, B. A.; Kumar, N.; Bellus, M. Z.; Chiu, H.-Y.; Zhao, H. Ultrafast and Spatially Resolved Studies of Charge Carriers in Atomically Thin Molybdenum Disulfide. *Phys. Rev. B* **2012**, *86*, 045406.
- (19) Kumar, N.; He, J.; He, D.; Wang, Y.; Zhao, H. Charge Carrier Dynamics in Bulk MoS<sub>2</sub> Crystal Studied by Transient Absorption Microscopy. *J. Appl. Phys.* **2013**, *113*, 133702.
- (20) Sim, S.; Park, J.; Song, J.-G.; In, C.; Lee, Y.-S.; Kim, H.; Choi, H. Exciton Dynamics in Atomically Thin MoS<sub>2</sub>: Interexcitonic Interaction and Broadening Kinetics. *Phys. Rev. B* **2013**, *88*, 075434.
- (21) Wang, Q.; Ge, S.; Li, X.; Qiu, J.; Ji, Y.; Feng, J.; Sun, D. Valley Carrier Dynamics in Monolayer Molybdenum Disulfide from Helicity-Resolved Ultrafast Pump–Probe Spectroscopy. *ACS Nano* **2013**, *7*, 11087–11093.
- (22) Völzer, T.; Lütgens, M.; Fennel, F.; Lochbrunner, S. Recombination Dynamics of Optically Excited Charge Carriers in Bulk MoS<sub>2</sub>. *J. Phys. B At. Mol. Opt. Phys.* **2017**, *50*, 194003.

- (23) Poonia, D.; Singh, N.; Schulpen, J. J. P. M.; van der Laan, M.; Maiti, S.; Failla, M.; Kinge, S.; Bol, A. A.; Schall, P.; Siebbeles, L. D. A. Effects of the Structure and Temperature on the Nature of Excitons in the  $\text{Mo}_{0.6}\text{W}_{0.4}\text{S}_2$  Alloy. *J. Phys. Chem. C* **2022**, *126*, 1931–1938.
- (24) Wilson, J. A.; Yoffe, A. D. The Transition Metal Dichalcogenides Discussion and Interpretation of the Observed Optical, Electrical and Structural Properties. *Adv. Phys.* **1969**, *18*, 193–335.
- (25) Zhao, W.; Ghorannevis, Z.; Amara, K. K.; Pang, J. R.; Toh, M.; Zhang, X.; Kloc, C.; Tan, P. H.; Eda, G. Lattice Dynamics in Mono- and Few-Layer Sheets of  $\text{WS}_2$  and  $\text{WSe}_2$ . *Nanoscale* **2013**, *5*, 9677.
- (26) Vega-Mayoral, V.; Vella, D.; Borzda, T.; Prijatelj, M.; Tempra, I.; Pogna, E. A. A.; Dal Conte, S.; Topolovsek, P.; Vujcic, N.; Cerullo, G.; Mihailovic, D.; Gadermaier, C. Exciton and Charge Carrier Dynamics in Few-Layer  $\text{WS}_2$ . *Nanoscale* **2016**, *8*, 5428–5434.
- (27) Tsokkou, D.; Yu, X.; Sivula, K.; Banerji, N. The Role of Excitons and Free Charges in the Excited-State Dynamics of Solution-Processed Few-Layer  $\text{MoS}_2$  Nanoflakes. *J. Phys. Chem. C* **2016**, *120*, 23286–23292.
- (28) Shi, H.; Yan, R.; Bertolazzi, S.; Brivio, J.; Gao, B.; Kis, A.; Jena, D.; Xing, H. G.; Huang, L. Exciton Dynamics in Suspended Monolayer and Few-Layer  $\text{MoS}_2$  2D Crystals. *ACS Nano* **2013**, *7*, 1072–1080.
- (29) Borzda, T.; Gadermaier, C.; Vujcic, N.; Topolovsek, P.; Borovsak, M.; Mertelj, T.; Viola, D.; Manzoni, C.; Pogna, E. A. A.; Brida, D.; Antognazza, M. R.; Scotognella, F.; Lanzani, G.; Cerullo, G.; Mihailovic, D. Charge Photogeneration in Few-Layer  $\text{MoS}_2$ . *Adv. Funct. Mater.* **2015**, *25*, 3351–3358.
- (30) Chen, K.; Ghosh, R.; Meng, X.; Roy, A.; Kim, J.-S.; He, F.; Mason, S. C.; Xu, X.; Lin, J.-F.; Akinwande, D.; Banerjee, S. K.; Wang, Y. Experimental Evidence of Exciton Capture by Mid-Gap Defects in CVD Grown Monolayer  $\text{MoSe}_2$ . *Npj 2D Mater. Appl.* **2017**, *1*, 1–8.
- (31) Bretscher, H.; Li, Z.; Xiao, J.; Qiu, D. Y.; Refaely-Abramson, S.; Alexander-Webber, J. A.; Tanoh, A.; Fan, Y.; Delpont, G.; Williams, C. A.; Stranks, S. D.; Hofmann, S.; Neaton, J. B.; Louie, S. G.; Rao, A. Rational Passivation of Sulfur Vacancy Defects in Two-Dimensional Transition Metal Dichalcogenides. *ACS Nano* **2021**, *15*, 8780–8789.
- (32) Cunningham, P. D.; McCreary, K. M.; Hanbicki, A. T.; Currie, M.; Jonker, B. T.; Hayden, L. M. Charge Trapping and Exciton Dynamics in Large-Area CVD Grown  $\text{MoS}_2$ . *J. Phys. Chem. C* **2016**, *120*, 5819–5826.

- (33) Sim, S.; Shin, H.-S.; Lee, D.; Lee, J.; Cha, M.; Lee, K.; Choi, H. Opposite Behavior of Ultrafast Dynamics of Exciton Shift and Linewidth Broadening in Bilayer ReS<sub>2</sub>. *Phys. Rev. B* **2021**, *103*, 014309.
- (34) Schiettecatte, P.; Poonia, D.; Tanghe, I.; Maiti, S.; Failla, M.; Kinge, S.; Hens, Z.; Siebbeles, L. D. A.; Geiregat, P. Unraveling the Photophysics of Liquid-Phase Exfoliated Two-Dimensional ReS<sub>2</sub> Nanoflakes. *J. Phys. Chem. C* **2021**, *125*, 20993–21002.
- (35) Schiettecatte, P.; Geiregat, P.; Hens, Z. Ultrafast Carrier Dynamics in Few-Layer Colloidal Molybdenum Disulfide Probed by Broadband Transient Absorption Spectroscopy. *J. Phys. Chem. C* **2019**, *123*, 10571–10577.
- (36) Sie, E. J.; Steinhoff, A.; Gies, C.; Lui, C. H.; Ma, Q.; Rösner, M.; Schönhoff, G.; Jahnke, F.; Wehling, T. O.; Lee, Y.-H.; Kong, J.; Jarillo-Herrero, P.; Gedik, N. Observation of Exciton Redshift–Blueshift Crossover in Monolayer WS<sub>2</sub>. *Nano Lett.* **2017**, *17*, 4210–4216.
- (37) Taank, P.; Karmakar, R.; Sharma, R.; Yadav, R. K.; Shrivastava, M.; Maurya, N. C.; Maji, T. K.; Karmakar, D.; Adarsh, K. V. An Insightful Picture of Multi-Particle Recombination in Few-Layer MoS<sub>2</sub> Nanosheets. *J. Phys. Chem. C* **2022**, *126*, 416–422.
- (38) Zhao, W.; Ribeiro, R. M.; Toh, M.; Carvalho, A.; Kloc, C.; Castro Neto, A. H.; Eda, G. Origin of Indirect Optical Transitions in Few-Layer MoS<sub>2</sub>, WS<sub>2</sub>, and WSe<sub>2</sub>. *Nano Lett.* **2013**, *13*, 5627–5634.
- (39) Moody, G.; Kavir Dass, C.; Hao, K.; Chen, C.-H.; Li, L.-J.; Singh, A.; Tran, K.; Clark, G.; Xu, X.; Berghäuser, G.; Malic, E.; Knorr, A.; Li, X. Intrinsic Homogeneous Linewidth and Broadening Mechanisms of Excitons in Monolayer Transition Metal Dichalcogenides. *Nat. Commun.* **2015**, *6*, 8315.
- (40) Stoneham, A. M. Shapes of Inhomogeneously Broadened Resonance Lines in Solids. *Rev. Mod. Phys.* **1969**, *41*, 82–108.
- (41) Hein, P.; Stange, A.; Hanff, K.; Yang, L. X.; Rohde, G.; Rosnagel, K.; Bauer, M. Momentum-Resolved Hot Electron Dynamics at the 2 H – MoS<sub>2</sub> Surface. *Phys. Rev. B* **2016**, *94*, 205406.
- (42) Addou, R.; Colombo, L.; Wallace, R. M. Surface Defects on Natural MoS<sub>2</sub>. *ACS Appl. Mater. Interfaces* **2015**, *7*, 11921–11929.
- (43) Wu, S.; Cheng, L.; Wang, Q. Exciton States and Absorption Spectra in Freestanding Monolayer Transition Metal Dichalcogenides: A Variationally Optimized Diagonalization Method. *Phys. Rev. B* **2019**, *100*, 115430.

- (44) Wang, X.; Niu, G.; Jiang, J.; Sui, L.; Zeng, X.; Liu, X.; Zhang, Y.; Wu, G.; Yuan, K.; Yang, X. Anomalous Dynamics of Defect-Assisted Phonon Recycling in Few-Layer  $\text{Mo}_{0.5}\text{W}_{0.5}\text{S}_2$ . *J. Phys. Chem. Lett.* **2022**, *13*, 10395–10403.
- (45) Cunningham, P. D.; Hanbicki, A. T.; McCreary, K. M.; Jonker, B. T. Photoinduced Bandgap Renormalization and Exciton Binding Energy Reduction in  $\text{WS}_2$ . *ACS Nano* **2017**, *11*, 12601–12608.
- (46) Steinhoff, A.; Rösner, M.; Jahnke, F.; Wehling, T. O.; Gies, C. Influence of Excited Carriers on the Optical and Electronic Properties of  $\text{MoS}_2$ . *Nano Lett.* **2014**, *14*, 3743–3748.
- (47) Chernikov, A.; Ruppert, C.; Hill, H. M.; Rigosi, A. F.; Heinz, T. F. Population Inversion and Giant Bandgap Renormalization in Atomically Thin  $\text{WS}_2$  Layers. *Nat. Photonics* **2015**, *9*, 466–470.
- (48) Jia, G. Y.; Liu, Y.; Gong, J. Y.; Lei, D. Y.; Wang, D. L.; Huang, Z. X. Excitonic Quantum Confinement Modified Optical Conductivity of Monolayer and Few-Layered  $\text{MoS}_2$ . *J. Mater. Chem. C* **2016**, *4*, 8822–8828.
- (49) Sharma, S.; Bhagat, S.; Singh, J.; Singh, R. C.; Sharma, S. Excitation-Dependent Photoluminescence from  $\text{WS}_2$  Nanostructures Synthesized via Top-down Approach. *J. Mater. Sci.* **2017**, *52*, 11326–11336.
- (50) Stier, A. V.; McCreary, K. M.; Jonker, B. T.; Kono, J.; Crooker, S. A. Exciton Diamagnetic Shifts and Valley Zeeman Effects in Monolayer  $\text{WS}_2$  and  $\text{MoS}_2$  to 65 Tesla. *Nat. Commun.* **2016**, *7*, 10643.
- (51) Ruppert, C.; Chernikov, A.; Hill, H. M.; Rigosi, A. F.; Heinz, T. F. The Role of Electronic and Phononic Excitation in the Optical Response of Monolayer  $\text{WS}_2$  after Ultrafast Excitation. *Nano Lett.* **2017**, *17*, 644–651.
- (52) Suryavanshi, S. V.; Gabourie, A. J.; Barati Farimani, A.; Pop, E. Thermal Boundary Conductance of Two-Dimensional  $\text{MoS}_2$  Interfaces. *J. Appl. Phys.* **2019**, *126*, 055107.
- (53) Roxlo, C. B.; Chianelli, R. R.; Deckman, H. W.; Ruppert, A. F.; Wong, P. P. Bulk and Surface Optical Absorption in Molybdenum Disulfide. *J. Vac. Sci. Technol. A* **1987**, *5*, 555–557.
- (54) O'Hare, P. A. G.; Hubbard, W. N.; Johnson, G. K.; Flotow, H. E. Calorimetric Measurements of the Low-Temperature Heat Capacity, Standard Molar Enthalpy of Formation at 298.15 K, and High-Temperature Molar Enthalpy Increments Relative to 298.15 K of Tungsten Disulfide ( $\text{WS}_2$ ), and the Thermodynamic Properties to 1500 K. *J. Chem. Thermodyn.* **1984**, *16*, 45–59.

- (55) Sim, S.; Park, J.; Song, J.-G.; In, C.; Lee, Y.-S.; Kim, H.; Choi, H. Exciton Dynamics in Atomically Thin MoS<sub>2</sub>: Interexcitonic Interaction and Broadening Kinetics. *Phys. Rev. B* **2013**, *88*.



# Chapter 5

## Multiexciton generation in monolayer MoSe<sub>2</sub>

## 5.1 Introduction

Solar cell invention has played an important role in the growth of thin film research. From the first generation of crystalline Si solar cells to third-generation organics solar cells, a lot of advancements have been made by the scientific community to increase photoconversion efficiency.<sup>1,2</sup> In this quest to find an ideal solar cell, transition metal dichalcogenides (TMDCs) have not remained aloof and research has been ongoing to understand the optoelectronic properties of TMDCs. TMDCs have also shown an efficient carrier multiplication efficiency making them a suitable host for photovoltaic applications.<sup>3,4</sup>

Carrier multiplication (CM) is a process in which the absorption of a single high-energy photon results in the generation of two or more electron-hole pairs. The process of carrier multiplication has been studied extensively in semiconductors.<sup>5</sup> While studying CM, the onset of CM along with the yield of photogenerated charges, are considered crucial factors. The onset of CM is the lowest photon energy from which CM starts. The quantum yield is defined as the number of electron-hole pairs generated per absorbed photon. In an ideal material, the onset of CM is at twice the bandgap energy, but in practice, the CM onset is found to be higher in energy in most of the semiconductors<sup>6-8</sup> and is dependent on the various microscopic parameters such as effective masses of electrons and holes<sup>9</sup> and density of states.<sup>10</sup>

In the past few years, TMDCs have gained considerable interest in photovoltaic applications owing to their large range of electronic bandgaps and high sunlight absorption coefficient.<sup>11,12</sup> This chapter reports studies of the process of multiexciton generation (MEG) in monolayer MoSe<sub>2</sub> film grown by chemical vapor deposition. MEG is the process of the generation of multiple excitons after the absorption of a single high energy photon. We performed pump photon fluence and energy-dependent experiments using ultrafast pump-probe spectroscopy. The occurrence of MEG is inferred from the magnitude of the transient optical absorption signal due to excitons as a function of pump photon energy at similar absorbed pump photon fluences. To determine the onset of multiexciton generation, we plotted the yield of excitons as a function of the A exciton photon energy multiple and found a higher yield at twice the A exciton energy.

## 5.2 Results and discussion

**Optical Absorption Spectroscopy.** To gain insights into the optical transitions, steady-state absorption measurements are performed on monolayer MoSe<sub>2</sub>. The absorption curve (blue) in Figure 5.1 shows the A and B exciton energy peaks at 1.6 eV and 1.8 eV.<sup>13</sup> The energy difference between the A and B exciton peaks is due to the spin-orbit splitting at the K/K' point of the Brillouin zone.<sup>13</sup> In addition to exciton peaks, higher energy absorption is also observed with a maximum near 2.6 eV, often termed as C exciton in the literature, which originates from the transitions between the valence and conduction band along the direction from K to  $\Gamma$  point.<sup>14</sup> The red curve in Figure 5.1 shows the 2 nm Stokes shifted photoluminescence (PL) spectrum of a monolayer MoSe<sub>2</sub> obtained after photoexcitation with a 532 nm laser. The photoluminescence signal is due to the direct transition at the K point of the Brillouin zone.

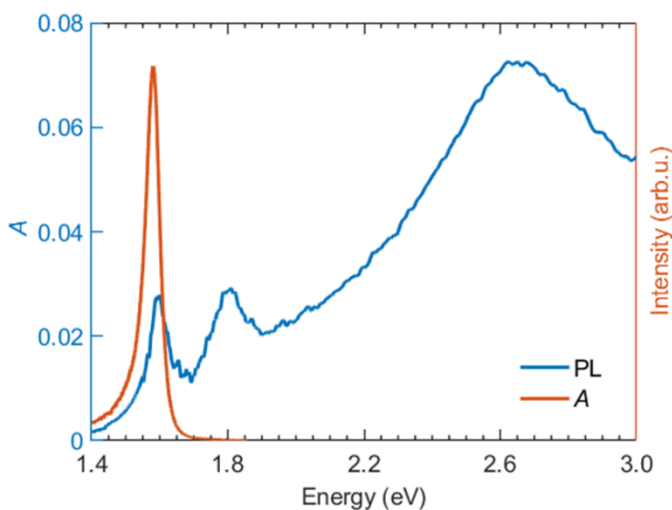


**Figure 5.1.** Optical absorption (blue curve) and photoluminescence (red curve) spectra of monolayer MoSe<sub>2</sub>.

**Transient absorption spectroscopy.** To study the process of multiexciton generation in monolayer MoSe<sub>2</sub>, we performed ultrafast pump-probe measurements (setup details in Chapter 1). Figure 5.2a shows the normalized differential transmission signal  $(\Delta T/T)/I_{\text{abs}}$  after excitation with multiple pump photon energies. Here,  $I_{\text{abs}}$  is the absorbed pump photon fluence and was set to  $(3.3 \pm 0.5) \times 10^{12}$  photons  $\text{cm}^{-2}$ . The signal is plotted at 1.59 eV (A exciton peak energy) and is plotted as a function of probe delay times.

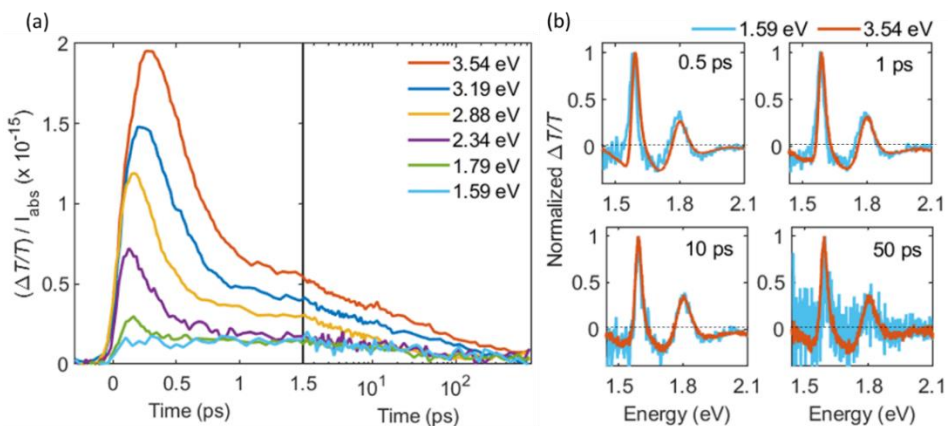


**Figure 5.2.** (a) Differential transmission signal recorded at the A exciton energy after photoexcitations at different pump photon energies and is normalized by the absorbed pump photon fluence of  $(3.3 \pm 0.5) \times 10^{12}$  photons  $\text{cm}^{-2}$ . (b) The normalized (by peak maximum) signal plotted at 0.5 ps, 1 ps, 10 ps, and 50 ps for 1.59 eV and 3.54 eV, respectively.

At all photoexcitation energies, a positive differential transmission signal is observed at the probing energy of 1.59 eV (A exciton), see Figure 5.2a. This positive feature has been attributed to formation of excitons that cause bleaching of the ground state.<sup>15,16</sup> In addition, stimulated emission from excitons also results in the observed positive signal.<sup>17</sup> After resonant photoexcitation (1.59 eV), excitons are predominantly generated in monolayer  $\text{MoSe}_2$  due to their high binding energy of  $\sim 500$  meV.<sup>18,19</sup> These photogenerated excitons relax back to the ground state within hundreds of picoseconds, as inferred from the decay of the bleach in Figure 5.2a. As the incident pump photon energy is increased, the magnitude of the signal is high and a sub-picosecond decay component emerges. The lifetime of the fast decay component is less than 1 ps for all non-resonant pump photon energies. This phenomenon has been previously observed in monolayer  $\text{MoSe}_2$  and  $\text{WSe}_2$  after non-resonant energy excitations and was attributed to the formation of excitons from the initially photogenerated hot charge carriers.<sup>20</sup>

In Figure 5.2a, the magnitude of the  $\Delta T/T$  signal is increasing as a function of incident pump photon energy at a similar  $I_{\text{abs}}$ . An increase in the  $\Delta T/T$  signal could be because of MEG, changes in the absorption cross-section of excitons, or a combination of both. For multiexciton generation to occur, the incident pump photon energy should be at least twice the A exciton energy. However, we observe a pump photon energy-dependent increase in the bleach, see Figure 5.2a. Pump

photon energy-dependent bleaching of the ground state has been reported in semiconductor quantum-well structures and was assigned to more efficient bleaching of the ground state by free charges than by excitons.<sup>20,21</sup> In monolayer WSe<sub>2</sub>, free charges were shown to be generated after the above bandgap photoexcitations and were present until 5 ps after photoexcitation.<sup>22</sup> Hence, we also expect the presence of photogenerated free charges at short probe delay times in monolayer MoSe<sub>2</sub>, which cause a stronger bleach of the ground state than the case for excitons.

From Figure 5.2a, free charges and excitons have relaxed within 10 ps, as the decay curves have fallen on top of each other for pump photon energies below twice the A exciton energy. However, for high energy excitations (above twice the A exciton energy), the magnitude of the signal remains higher at longer probe delay times, indicating the presence of more excitons per absorbed photon. Figure 5.2b shows the shape of the  $\Delta T/T$  spectra after normalizing by the peak maximum. The shape of the spectra is not changing after 10 ps for resonant and non-resonant pump photon energies. Hence, after 10 ps only excitons are present in a monolayer of MoSe<sub>2</sub> for all pump photon energies.

To estimate the yield of excitons, we select a probe time range of 50-95 ps, where no contribution from hot charge carriers is expected and only excitons are present. Figure 5.3a shows the normalized time-averaged absolute spectra ( $|\Delta T/T|/I_{\text{abs}}$ ) plotted for different pump photon energies. The magnitude of the signal for 3.54 eV and 3.19 eV is higher than for the lower pump photon energies. We integrated the area under the A exciton peak (dashed vertical black lines) for all pump photon energies to estimate the quantum yield of excitons. Quantum yield is generally expressed as the number of photogenerated charge carriers per absorbed pump photon energy. Figure 5.3b shows the relative quantum yield of excitons, which is calculated by dividing the yield of excitons at a higher pump photon energy by the yield of excitons at the resonant pump energy.

In Figure 5.3b, the relative quantum yield is plotted as a function of the A exciton energy multiple,  $(h\nu/E_A)$ , where  $h\nu$  is the incident photon energy and  $E_A$  is the A exciton energy. For the two photon energies  $\geq 2E_A$ , the quantum yield increases from 1.0 to 1.5 and 2, respectively. A higher quantum yield represents the presence of multiple electron-hole pairs in monolayer MoSe<sub>2</sub> film. Multiexciton generation with efficiencies of 94-99% has been inferred recently from pump-probe measurements

in multilayer  $\text{MoTe}_2$ .<sup>3,4</sup> Higher MEG efficiencies in TMDCs have been attributed to a weaker electron-phonon coupling, which results in a lower hot carrier cooling rate. We can attribute the high quantum efficiency of  $\text{MoSe}_2$  to a result of a weaker coupling. Additionally, DFT calculations have shown that the presence of a higher density of states (for example in multilayer  $\text{MoTe}_2$ ) also increases the rate of the MEG process.<sup>23</sup>

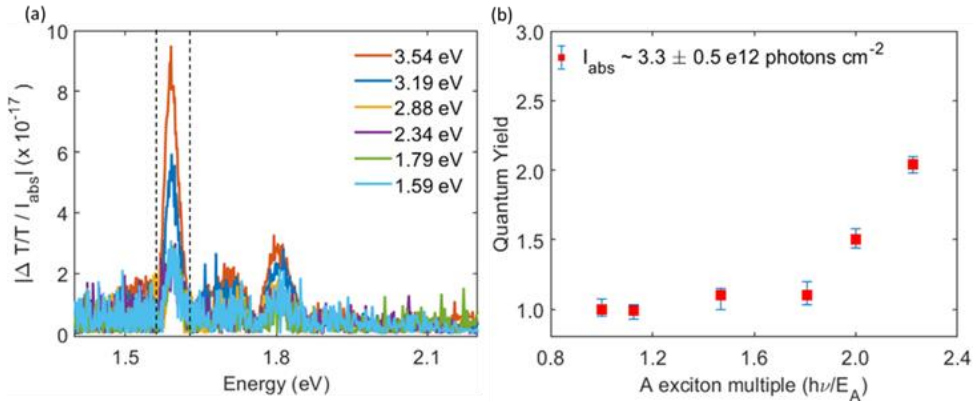


**Figure 5.3.** (a) Time averaged (50 ps - 95 ps) normalized transient transmission spectra at pump photon energies as indicated. (b) Quantum yield as a function of the A exciton energy multiple.

Next, we vary  $I_{\text{abs}}$  and calculate the yield of excitons as shown in Figure 5.4. We integrate the A exciton peak at different photon fluences and plot the relative quantum yield as a function of  $h\nu/E_A$ .

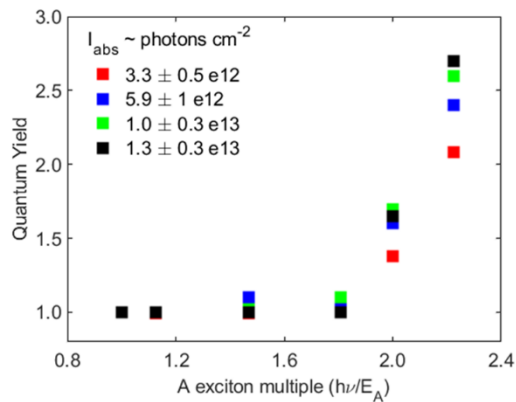


**Figure 5.4.** The quantum yield of excitons as a function of the A exciton energy multiple at various absorbed pump photon fluences.

From Figure 5.4, the quantum yield of excitons is seen to depend on  $I_{\text{abs}}$  and, surprisingly, it is more than two for pump photon energies below thrice the A exciton energy. These results are quite uncommon, as we do not expect a quantum yield greater than two for photon energies below thrice the bandgap. Recently, Liu et.al. have shown a lower MEG threshold of  $1.51 E_g$  for monolayer WS<sub>2</sub>.<sup>24</sup> They compared two monolayer WS<sub>2</sub> films, one pristine and the other containing sulfur vacancies. The MEG threshold was found to be lower in the latter. The lower threshold was attributed to the promotion of an electron from the valence band to the defect states inside the bandgap by utilizing the excess energy of the initially photoexcited electron.

### 5.3 Conclusions

To summarize, we observed the generation of multiexcitons in monolayer MoSe<sub>2</sub>, with a MEG threshold at twice the A exciton energy. As an effect of increasing the absorbed pump photon fluence, a fluence-dependent yield of excitons is observed. However, we need more experiments to find out if the results reproduce and in that case theoretical studies are needed to understand the origins of the MEG process in monolayer MoSe<sub>2</sub> samples as studied here. The effects of free charges and excitons on the amplitude of the bleach signal and the effects of pump fluence and defect states on MEG both need to be investigated further.

## References

- (1) Akinoglu, B. G.; Tuncel, B.; Badescu, V. Beyond 3rd Generation Solar Cells and the Full Spectrum Project. Recent Advances and New Emerging Solar Cells. *Sustain. Energy Technol. Assess.* **2021**, *46*, 101287.
- (2) Fukuda, K.; Yu, K.; Someya, T. The Future of Flexible Organic Solar Cells. *Adv. Energy Mater.* **2020**, *10*, 2000765.
- (3) Kim, J.-H.; Bergren, M. R.; Park, J. C.; Adhikari, S.; Lorke, M.; Frauenheim, T.; Choe, D.-H.; Kim, B.; Choi, H.; Gregorkiewicz, T.; Lee, Y. H. Carrier Multiplication in van Der Waals Layered Transition Metal Dichalcogenides. *Nat. Commun.* **2019**, *10*.
- (4) Zheng, W.; Bonn, M.; Wang, H. I. Photoconductivity Multiplication in Semiconducting Few-Layer MoTe<sub>2</sub>. *Nano Lett.* **2020**, *20*, 5807–5813.
- (5) Maiti, S.; van der Laan, M.; Poonia, D.; Schall, P.; Kinge, S.; Siebbeles, L. D. A. Emergence of New Materials for Exploiting Highly Efficient Carrier Multiplication in Photovoltaics. *Chem. Phys. Rev.* **2020**, *1*, 011302.
- (6) Aerts, M.; Bielewicz, T.; Klinke, C.; Grozema, F. C.; Houtepen, A. J.; Schins, J. M.; Siebbeles, L. D. A. Highly Efficient Carrier Multiplication in PbS Nanosheets. *Nat. Commun.* **2014**, *5*, 3789.
- (7) Ellingson, R. J.; Beard, M. C.; Johnson, J. C.; Yu, P.; Micic, O. I.; Nozik, A. J.; Shabaev, A.; Efros, A. L. Highly Efficient Multiple Exciton Generation in Colloidal PbSe and PbS Quantum Dots. *Nano Lett.* **2005**, *5*, 865–871.
- (8) Beard, M. C.; Knutsen, K. P.; Yu, P.; Luther, J. M.; Song, Q.; Metzger, W. K.; Ellingson, R. J.; Nozik, A. J. Multiple Exciton Generation in Colloidal Silicon Nanocrystals. *Nano Lett.* **2007**, *7*, 2506–2512.
- (9) Schaller, R. D.; Pietryga, J. M.; Klimov, V. I. Carrier Multiplication in InAs Nanocrystal Quantum Dots with an Onset Defined by the Energy Conservation Limit. *Nano Lett.* **2007**, *7*, 3469–3476.
- (10) Kirchartz, T.; Rau, U. What Makes a Good Solar Cell? *Adv. Energy Mater.* **2018**, *8*, 1703385.
- (11) Bernardi, M.; Palummo, M.; Grossman, J. C. Extraordinary Sunlight Absorption and One Nanometer Thick Photovoltaics Using Two-Dimensional Monolayer Materials. *Nano Lett.* **2013**, *13*, 3664–3670.
- (12) Chaves, A.; Azadani, J. G.; Alsalman, H.; da Costa, D. R.; Frisenda, R.; Chaves, A. J.; Song, S. H.; Kim, Y. D.; He, D.; Zhou, J.; Castellanos-Gomez, A.; Peeters, F. M.;

- Liu, Z.; Hinkle, C. L.; Oh, S.-H.; Ye, P. D.; Koester, S. J.; Lee, Y. H.; Avouris, P.; Wang, X.; Low, T. Bandgap Engineering of Two-Dimensional Semiconductor Materials. *Npj 2D Mater. Appl.* **2020**, *4*, 1–21.
- (13) Zhang, Y.; Chang, T.-R.; Zhou, B.; Cui, Y.-T.; Yan, H.; Liu, Z.; Schmitt, F.; Lee, J.; Moore, R.; Chen, Y.; Lin, H.; Jeng, H.-T.; Mo, S.-K.; Hussain, Z.; Bansil, A.; Shen, Z.-X. Direct Observation of the Transition from Indirect to Direct Bandgap in Atomically Thin Epitaxial MoSe<sub>2</sub>. *Nat. Nanotechnol.* **2014**, *9*, 111–115.
- (14) Qiu, D. Y.; da Jornada, F. H.; Louie, S. G. Optical Spectrum of MoS<sub>2</sub>: Many-Body Effects and Diversity of Exciton States. *Phys. Rev. Lett.* **2013**, *111*, 216805.
- (15) Shi, H.; Yan, R.; Bertolazzi, S.; Brivio, J.; Gao, B.; Kis, A.; Jena, D.; Xing, H. G.; Huang, L. Exciton Dynamics in Suspended Monolayer and Few-Layer MoS<sub>2</sub> 2D Crystals. *ACS Nano* **2013**, *7*, 1072–1080.
- (16) Vega-Mayoral, V.; Vella, D.; Borzda, T.; Prijatelj, M.; Tempra, I.; Pogna, E. A. A.; Dal Conte, S.; Topolovsek, P.; Vujicic, N.; Cerullo, G.; Mihailovic, D.; Gadermaier, C. Exciton and Charge Carrier Dynamics in Few-Layer WS<sub>2</sub>. *Nanoscale* **2016**, *8*, 5428–5434.
- (17) Failla, M.; García Flórez, F.; Salzmann, B. B. V.; Vanmaekelbergh, D.; Stoof, H. T. C.; Siebbeles, L. D. A. Effects of Pump Photon Energy on Generation and Ultrafast Relaxation of Excitons and Charge Carriers in CdSe Nanoplatelets. *J. Phys. Chem. C* **2023**, *127*, 1899–1907.
- (18) Wang, G.; Gerber, I. C.; Bouet, L.; Lagarde, D.; Balocchi, A.; Vidal, M.; Amand, T.; Marie, X.; Urbaszek, B. Exciton States in Monolayer MoSe<sub>2</sub>: Impact on Interband Transitions. *2D Mater.* **2015**, *2*, 045005.
- (19) Mueller, T.; Malic, E. Exciton Physics and Device Application of Two-Dimensional Transition Metal Dichalcogenide Semiconductors. *Npj 2D Mater. Appl.* **2018**, *2*, 1–12.
- (20) Ceballos, F.; Cui, Q.; Bellus, M. Z.; Zhao, H. Exciton Formation in Monolayer Transition Metal Dichalcogenides. *Nanoscale* **2016**, *8*, 11681–11688.
- (21) Schmitt-Rink, S.; Chemla, D. S.; Miller, D. A. B. Theory of Transient Excitonic Optical Nonlinearities in Semiconductor Quantum-Well Structures. *Phys. Rev. B* **1985**, *32*, 6601–6609.
- (22) Steinleitner, P.; Merkl, P.; Nagler, P.; Mornhinweg, J.; Schüller, C.; Korn, T.; Chernikov, A.; Huber, R. Direct Observation of Ultrafast Exciton Formation in a Monolayer of WSe<sub>2</sub>. *Nano Lett.* **2017**, *17*, 1455–1460.

- (23) Weerdenburg, S. A Theoretical Study on Charge Carrier Multiplication in 2H-MoTe<sub>2</sub>. Master of Science, Delft University of Technology, The Netherlands, 2022.
- (24) Liu, Y.; Frauenheim, T.; Yam, C. Carrier Multiplication in Transition Metal Dichalcogenides Beyond Threshold Limit. *Adv. Sci.* **2022**, *9*, 2203400.

# Summary

The present thesis reports the nature of photogenerated charges and their dynamics in layers of transition metal dichalcogenides and their alloys. The contents of each chapter are summarized below.

**Chapter 2:** In this chapter, we have analyzed the nature and dynamics of charge carriers in highly crystalline liquid-phase exfoliated ReS<sub>2</sub>, using a unique combination of optical pump-THz probe and broad-band transient absorption spectroscopy. Two distinct time regimes are identified, both of which are dominated by unbound charge carriers despite the high exciton binding energy. In the first-time regime, the unbound charge carriers cause an increase and a broadening of the exciton absorption band. In the second time regime, a peculiar narrowing of the excitonic absorption profile is observed, which we assign to the presence of built-in fields and/or charged defects. Our results pave the way to analyze spectrally complex transient absorption measurements on layered TMD materials and indicate the potential for ReS<sub>2</sub> to produce mobile free charge carriers, a feat relevant for photovoltaic applications.

**Chapter 3:** We studied the nature of excitons in the transition metal dichalcogenide alloy Mo<sub>0.6</sub>W<sub>0.4</sub>S<sub>2</sub> compared to pure MoS<sub>2</sub> and WS<sub>2</sub> grown by atomic layer deposition (ALD). For this, optical absorption/transmission spectroscopy and time-dependent density functional theory (TDDFT) were used. The effects of temperature on A and B exciton peak energies and line widths in optical transmission spectra were compared between the alloy and pure MoS<sub>2</sub> and WS<sub>2</sub>. On increasing the temperature from 25 to 293 K, the energy of the A and B exciton peaks decreases, while their line width increases due to exciton-phonon interactions. The exciton-phonon interactions in the alloy are closer to those for MoS<sub>2</sub> than those for WS<sub>2</sub>. This suggests that exciton wave functions in the alloy have a larger amplitude on Mo atoms than that on W atoms. The experimental absorption spectra could be reproduced by TDDFT calculations. Interestingly, for the alloy, the Mo and W atoms had to be distributed over all layers. Conversely, we could not reproduce the experimental alloy spectrum by calculations on a structure with alternating layers, in which every other layer contains only Mo atoms, and the layers in between also contain W atoms. For the latter atomic arrangement, the TDDFT calculations yielded an additional optical absorption peak that could be due to

excitons with some charge transfer character. From these results, we conclude that ALD yields an alloy in which Mo and W atoms are distributed uniformly among all layers.

**Chapter 4:** We analyzed photogenerated exciton and charge carrier dynamics in ALD grown  $\text{MoS}_2$ ,  $\text{WS}_2$ , and the  $\text{Mo}_{0.6}\text{W}_{0.4}\text{S}_2$  alloy using time-resolved pump-probe measurements. In all three compounds, the A and B excitons peaks show a blueshift and linewidth narrowing on the probed timescale up to 2.5 ns after the pump pulse. Upon photoexcitation, free charges are generated within 1 ps, which can screen the electron-hole attraction in an exciton, causing a blueshift. Charges can cause a linewidth narrowing by homogenizing the local environment around an exciton in the material. Our pump photon energy and photon fluence-dependent measurements on the  $\text{Mo}_{0.6}\text{W}_{0.4}\text{S}_2$  alloy revealed that the A exciton linewidth narrowing and blueshift depend on the density of photogenerated charges.

**Chapter 5:** In this chapter, we studied the process of multiexciton generation (MEG) in monolayer  $\text{MoSe}_2$  film grown by chemical vapor deposition. MEG refers to the process of the generation of multiple bound charge-charge pairs after the absorption of a single high-energy photon. We performed pump photon fluence and energy-dependent experiments using ultrafast pump-probe spectroscopy. The occurrence of MEG is inferred from the magnitude of the transient optical absorption signal due to excitons as a function of pump photon energy at similar absorbed pump photon fluences. We observed the generation of multiexcitons in a monolayer  $\text{MoSe}_2$  and the MEG threshold is observed at twice the A exciton energy. On increasing absorbed pump photon fluence, we observed a fluence-dependent yield of excitons.

# Samenvatting

Dit proefschrift rapporteert de aard van door licht gegenereerde ladingen en hun dynamiek in lagen van overgangsmetaaldichalcogeniden en hun legeringen. De inhoud van elk hoofdstuk wordt hieronder samengevat.

**Hoofdstuk 2:** In dit hoofdstuk hebben we de aard en dynamiek van ladingsdragers in hoogkristallijne vloeibare fase geëxfolieerde  $\text{ReS}_2$  geanalyseerd, met behulp van een unieke combinatie van optische pomp-THz-sonde en breedbandige kortstondige absorptiespectroscopie. Er worden twee verschillende tijdregimes geïdentificeerd, die beide worden gedomineerd door ongebonden ladingsdragers ondanks de hoge excitonbindingsenergie. In het eerste regime veroorzaken de ongebonden ladingsdragers een toename en een verbreding van de excitonabsorptieband. In het tweede tijdsregime wordt een bijzondere vernauwing van het excitonische absorptieprofiel waargenomen, die we toeschrijven aan de aanwezigheid van ingebouwde velden en/of geladen defecten. Onze resultaten banen een weg om spectraal complexe kortstondige absorptiemetingen op gelaagde TMD-materialen te analyseren en geven het potentieel aan voor  $\text{ReS}_2$  om mobiele vrije ladingsdragers te produceren, een prestatie die relevant is voor fotonische toepassingen.

**Hoofdstuk 3:** We bestudeerden de aard van excitonen in de overgangsmetaal dichalcogenide legering  $\text{Mo}_{0.6}\text{W}_{0.4}\text{S}_2$  in vergelijking met puur  $\text{MoS}_2$  en  $\text{WS}_2$  gegroeid door atomic layer deposition (ALD). Hiervoor werden optische absorptie-/transmissiespectroscopie en tijdsafhankelijke dichtheidsfunctionaaltheorie (TDDFT) gebruikt. De effecten van temperatuur op A- en B-excitonpiekenergieën en lijnbreedten in optische transmissiespectra werden vergeleken tussen de legering en pure  $\text{MoS}_2$  en  $\text{WS}_2$ . Bij het verhogen van de temperatuur van 25 naar 293 K, neemt de energie van de A- en B-excitonpieken af, terwijl hun lijnbreedte toeneemt als gevolg van exciton-fonon-interacties. De exciton-fonon-interacties in de legering lijken meer op die van  $\text{MoS}_2$  dan die van  $\text{WS}_2$ . Dit suggereert dat excitongolffuncties in de legering een grotere amplitude hebben op Mo-atomen dan op W-atomen. De experimentele absorptiespectra konden worden gereproduceerd door TDDFT-berekeningen. Interessant is dat voor de legering de Mo- en W-atomen over alle lagen moesten worden verdeeld. Omgekeerd konden we het experimentele legeringsspectrum niet reproduceren door berekeningen op een structuur met afwisselende lagen, waarin elke andere laag alleen Mo-atomen bevat, en de lagen

ertussen ook W-atomen bevatten. Voor die laatste atomaire rangschikking leverden de TDDFT-berekeningen een extra optische absorptiepiek op die te wijten zou kunnen zijn aan excitonen met een bepaald ladingsoverdrachtskarakter. Uit deze resultaten concluderen we dat ALD een legering oplevert waarin Mo- en W-atomen gelijkmatig over alle lagen zijn verdeeld.

**Hoofdstuk 4:** We analyseerden de fotongegeneerde exciton- en ladingsdragerdynamiek in ALD-gegroeid  $\text{MoS}_2$ ,  $\text{WS}_2$  en de  $\text{Mo}_{0.6}\text{W}_{0.4}\text{S}_2$ -legering met behulp van tijdsopgeloste pomp-sond-metingen. In alle drie materialen vertonen de A- en B-excitonpieken een blauwverschuiving en vernauwing van de lijnbreedte op de onderzochte tijdschaal tot 2,5 ns na de pomppuls. Bij foton-excitatie worden binnen 1 ps vrije ladingen gegeneerd, die de elektron-gat-aantrekking in een exciton kunnen afschermen, waardoor een blauwverschuiving ontstaat. Ladingen kunnen een vernauwing van de lijnbreedte veroorzaken door de lokale omgeving rond een exciton in het materiaal te homogeniseren. Onze pomffotonenergie en fotonfluentie-afhankelijke metingen op de  $\text{Mo}_{0.6}\text{W}_{0.4}\text{S}_2$ -legering onthulden dat de A-exciton lijnbreedtevernauwing en blauwverschuiving afhangen van de dichtheid van fotongegeneerde ladingen.

**Hoofdstuk 5:** In dit hoofdstuk bestudeerden we het proces van multi-exciton generatie (MEG) in monolaag  $\text{MoSe}_2$  film gegroeid door chemische damp depositie. MEG verwijst naar het proces van het genereren van meerdere gebonden lading-ladingparen na absorptie van een enkel hoogenergetisch foton. We voerden pomffotonenfluentie en energieafhankelijke experimenten uit met behulp van ultrasnelle pompsondespectroscopie. Het optreden van MEG wordt afgeleid uit de grootte van het voorbijgaande optische absorptiesignaal als gevolg van excitonen als een functie van pomffotonenergie bij vergelijkbare geabsorbeerde pomffotonfluenties. We observeerden de generatie van multi-excitonen in een monolaag  $\text{MoSe}_2$  en de MEG-drempel wordt waargenomen bij tweemaal de A-exciton-energie. Bij toenemende geabsorbeerde pomffotonenfluentie zagen we een fluentieafhankelijke opbrengst van excitonen.

# List of Publications

- 1 *Unraveling the Photophysics of Liquid-Phase Exfoliated Two-Dimensional ReS<sub>2</sub> Nanoflakes*  
P. Schiettecatte, **D. Poonia**, I. Tanghe, S. Maiti, M. Failla, S. Kinge, Z. Hens, L.D.A Siebbeles, P. Geiregat  
J. Phys. Chem. C 2021, 125, 38, 20993–21002
- 2 *Effects of the Structure and Temperature on the Nature of Excitons in the Mo<sub>0.6</sub>W<sub>0.4</sub>S<sub>2</sub> Alloy*  
**D. Poonia**, N. Singh, J.JPM Schulpen, M. Van Der Laan, S. Maiti, M. Failla, S. Kinge, A.A Bol, P. Schall, L.D.A Siebbeles  
J. Phys. Chem. C 2022, 126, 4, 1931–1938
- 3 *Generating Triplets in Organic Semiconductor Tetracene upon Photoexcitation of Transition Metal Dichalcogenide ReS<sub>2</sub>*  
S. Maiti, **D. Poonia**, P. Schiettecatte, Z. Hens, P. Geiregat, S. Kinge, L.D.A Siebbeles  
J. Phys. Chem. Lett. 2021, 12, 22, 5256–5260
- 4 *Emergence of New Materials for Exploiting Highly Efficient Carrier Multiplication in Photovoltaics*  
S. Maiti, M. Van Der Laan, **D. Poonia**, P. Schall, S. Kinge, L.D.A Siebbeles  
Chem. Phys. Rev. 1, 011302 (2020)
- 5 *Efficient Carrier Multiplication in Low Band Gap Mixed Sn/Pb Halide Perovskites*  
S. Maiti, S. Ferro, **D. Poonia**, B. Ehrler, S. Kinge, L.D.A Siebbeles  
J. Phys. Chem. Lett. 2020, 11, 15, 6146–6149
- 6 *Photon Recycling in CsPbBr<sub>3</sub> All-Inorganic Perovskite Nanocrystals*  
M. Van Der Laan, C. De Weerd, L. Poirier, O. Van De Water, **D. Poonia**, L. Gomez, S. Kinge, L.D.A Siebbeles, A. Femius Koenderink, T. Gregorkiewicz, P. Schall  
ACS Photonics 2021, 8, 11, 3201–3208

- 7 *Electronic Coupling of Highly Ordered Perovskite Nanocrystals in Supercrystals*  
Y. Tang, **D. Poonia**, M. Van Der Laan, D. Timmerman, S. Kinge, L.D.A Siebbeles, P. Schall  
ACS Appl. Energy Mater. 2022, 5, 5, 5415–5422
- 8 *Stacking-Order-Dependent Excitonic Properties Reveal Interlayer Interactions in Bulk ReS<sub>2</sub>*  
M. Van Der Laan, E. Heemskerk, F. Kienhuis, N. Diepeveen, **D. Poonia**, S. Kinge, M. Triet Dang, V. An Dinh, L.D.A Siebbeles, A. Isaeva, J. Van De Groep, P. Schall  
ACS Photonics 2023, XXXX, XXX, XXX-XXX

# Deepika Poonia

July 28<sup>th</sup> 1995, Jaipur, India

2012 - 2015    **Bachelor of Science (Physics, Chemistry and Mathematics)**

*Maharani College, Rajasthan University, India*

2015 - 2017    **Master of Science (Physics)**

Indian Institute of Technology Indore, India

2019 - 2023    **PhD in Chemical Engineering**

Delft University of Technology, the Netherlands

Doctoral research in the group of Prof. dr. L.D.A Siebbeles

*Dynamics and nature of photogenerated excitons and charges in transition metal dichalcogenide thin films*

